

Copyright
by
Casey William Miller
2003

The Dissertation Committee for Casey William Miller
certifies that this is the approved version of the following dissertation:

**Nuclear Magnetic Resonance Force Microscopy:
Adiabaticity, External Field Effects,
and
Demonstration of Magnet-on-Oscillator Detection with
Sub-Micron Resolution**

Committee:

John T. Markert, Supervisor

C. K. Ken Shih

Zhen Yao

Jack B. Swift

David W. Hoffman

**Nuclear Magnetic Resonance Force Microscopy:
Adiabaticity, External Field Effects,
and
Demonstration of Magnet-on-Oscillator Detection with
Sub-Micron Resolution**

by

Casey William Miller, B.A.

DISSERTATION

Presented to the Faculty of the Graduate School of
The University of Texas at Austin
in Partial Fulfillment
of the Requirements
for the Degree of

DOCTOR OF PHILOSOPHY

THE UNIVERSITY OF TEXAS AT AUSTIN

December 2003

Dedicated to my family...

To my wife...

*for teaching me that sometimes “good enough” actually is good enough,
for giving me something infinitely more important than anything else,
and for touching my soul...*

To my mother...

*for always encouraging me in my pursuit of happiness,
for instilling in me a tenacious eye for detail and the diligence to use it,
and for loving me without bounds...*

To my father...

*for having the courage to teach me how to be a man,
for believing that I should always speak my mind,
and for the still spotless name he gave to his son...*

To my sister...

*for always looking up to me,
for giving me someone to look up to,
and for undertaking a beautiful and enviable life...*

To my grandfather...

for teaching me to take my time, especially with the little things...

Acknowledgments

First and foremost, it is my pleasure to thank my wife, Michelle, for all of her love and support that extends throughout my life. Probably the least important aspect of this was her fabrication of impeccable oscillators capped with $3\ \mu\text{m}$ cylindrical magnets so that I could graduate. Without her I would probably have found myself caught up in the whirlwind of research instead of anchored in a reality where physics is just physics, rock-n-roll is just rock-n-roll, and neither of them are really that important. With all that I am, and all that I have. . .

Second and also foremost, I thank John Markert for giving me the opportunity to work with him under less than optimal initial conditions. I must also thank him for his endlessly encouraging demeanor, his unmatched advisement, and for not getting too annoyed at me for keeping him updated daily on my bottomless stupidity. I consider him a great friend. But at the same time, I'd also like to thank his wife, Christiana Park, for making sure he didn't spend his nights and weekends in the lab.

I can't say enough about The Reverend Doctor Troy Messina, so I'll stick to the good stuff. His help in the lab was always worth asking for, and I'm glad that my gas-flow-rigged spectrometer worked well enough that he was able to do good things with it. Our "which one of us is stupider" conversations

were always refreshing. If he hadn't actually married Michelle and I, he would have been one of my Best Men.

Jack Clifford is probably the most acknowledged individual in all UT Physics dissertations, and with good reason. Jack has always been there for me whether I had a shop emergency, personal crisis, or just needed to drink the lab off my mind. I will raise my glass in his name for years to come.

I want to thank Utkir Mirsaidov for finally breaking out of his shell and making sure the lab was always a fun place to be. I don't think I've ever had as many hysterical outbreaks at the expense of one individual. It's a good thing too, because the laughter counteracted the hypertension caused by his comedy of errors always taking place too near my experiment.

Thank you also to Jae-Hyuk Choi for the pleasure of his company. He has great patience, which makes him a great teacher. His idea for measuring MgB_2 single crystals with NMR-FM is exactly what John's lab needs to establish itself as an NMR-FM powerhouse; I'm glad I could be a part of its birth.

And now for others I shouldn't forget. My thanks to John England in the electronics shop for consulting me throughout the design phase of the relaxation time measurement circuit. Thank you to Yong Lee for letting me pick his brain every now and then, and for the photodiode circuit. Thank you to Samareh Guchhait for building me random but necessary stuff in the shop when I didn't have the time. And thank you to Mark Monti for filling the LN_2

in the mornings.

I must also thank Sean Garner from John Marohn's MRFM group at Cornell. His conversations on the phone and by email have been a great help. I suggest that all future graduate students find at least one friend in other MRFM groups (March Meeting is a good place to start) so that they can bounce ideas off of each other and talk about experimental methods; knowing what other people do is a great advantage to knowing what you are doing.

I want to thank John Sidles from the University of Washington for always answering my many emails regarding various aspects of the experiment. Thanks also to John Mamin from Dan Rugar's MRFM group at IBM for our great phone conversation about the laser-induced self-oscillations of the oscillators. John Moreland from NIST in Boulder, Colorado has also been fun to work with, mostly because he brews his own beer and can shoot pool, but also because of interesting discussions about the external field effects on magnetically capped oscillators.

Last, but certainly not least since they all kept me sane, I must thank Philip Janisiewicz, Jennifer Sobeck, Dave "The Mang" Schlichte, Adam Rothschild, Jim Weston, and future M.D. Justin Miller.

**Nuclear Magnetic Resonance Force Microscopy:
Adiabaticity, External Field Effects,
and
Demonstration of Magnet-on-Oscillator Detection with
Sub-Micron Resolution**

Publication No. _____

Casey William Miller, Ph.D.
The University of Texas at Austin, 2003

Supervisor: John T. Markert

Investigations of the adiabatic condition governing nuclear magnetic resonance force microscopy (NMR-FM) have been performed. It has been determined that the adiabatic conditional factor for protons in ammonium sulfate must have a value of 1.5 or greater to optimize the NMR-FM signal. A theoretical formalism is presented that describes the data.

The characteristics of CoPt-capped single-crystal-silicon micro-oscillators with a magnetic field applied perpendicular to the magnetic film have been determined. The resonance frequency of the oscillators show two distinct regimes, one of softening and one of stiffening of the oscillator. A model is developed

to describe the previously unseen softening. This work suggests that using NMR-FM with a magnetic particle on the oscillator is experimentally feasible.

Magnet-on-oscillator NMR-FM has been demonstrated for the first time with our NMR-FM microscope using resonance slice thicknesses as small as ~ 150 nm. The sample investigated was a semi-infinite slab of ammonium sulfate. The resonance slice of the microscope was scanned from vacuum into the sample by changing the tuned carrier frequency of the AC magnetic field H_1 . The resulting signal-to-noise ratio of ~ 4 is slightly better than what was expected from conservative calculations.

Finally, feasibility calculations and an experimental plan are set forth for the future measurement of relaxation times of single crystals of the superconductor magnesium diboride.

Table of Contents

Acknowledgments	v
Abstract	viii
List of Tables	xiv
List of Figures	xv
Chapter 1. Introduction to Nuclear Magnetic Resonance Force Microscopy with Literature Review	1
1.1 Nuclear Magnetic Resonance	1
1.1.1 Quantum Theory of the Two-State System	1
1.1.1.1 Overview	2
1.1.1.2 Spin Precession in a Uniform Magnetic Field	3
1.1.1.3 Spin Magnetic Resonance	6
1.1.2 Semi-Classical Theory	9
1.1.3 NMR Spin Manipulation Techniques	12
1.1.4 Spin-Lattice and Spin-Spin Relaxation Times	14
1.2 NMR Force Microscopy Theory	15
1.2.1 Cyclic Adiabatic Inversion	16
1.3 The Basic MRFM Experiment and Its Components	19
1.3.1 The RF Coil	20
1.3.1.1 Relaxation Time Measurements	21
1.3.1.2 Spin Manipulation Regimes	21
1.3.2 Magnetic Field Gradient	24
1.3.3 Mechanical Oscillators	26
1.3.4 Fiber Optic Interferometer	29
1.3.5 Lock-in Amplifier	32
1.3.6 The Sample	33

Chapter 2. Experimental Details	36
2.1 Determining Oscillator Characteristics	36
2.1.1 Determining Resonance Frequencies	37
2.1.1.1 Frequency Scans	37
2.1.1.2 Fourier Transforms	38
2.1.2 Determining Quality Factors	40
2.1.2.1 Frequency Scans	40
2.1.2.2 Ring-Down	42
2.1.3 Determining Spring Constants	43
2.1.4 Fringe Locking Circuit	47
2.2 Blind-Aligning of Fiber to Oscillator	48
2.3 Tube Piezo for 2-D and 3-D Scanning	55
2.3.1 Piezo Stage Design	56
2.3.2 Scanning Tube Electronics	57
2.3.3 \hat{z} Piezo Characterization	58
2.4 Relaxation Time Measurement Electronics	61
2.4.1 Circuit Analysis	63
2.4.2 Making Relaxation Time Measurements	66
2.5 RF Signal Artifact	72
2.5.1 Experimental Method	73
2.5.2 Initial Ringing	74
2.5.3 Frequency Modulation Effects	76
2.5.4 Relative Tuning of Tank Circuit	78
2.6 Laser-Induced Self-Excitation of Oscillators	82
Chapter 3. Testing the Adiabatic Condition	90
3.1 Statement of the Adiabatic Condition	90
3.2 Ω - H_1 Parameter Space	92
3.2.1 Manipulated Magnetization	93
3.2.2 What does “much greater than” really mean?	96
3.2.2.1 Experimental Concerns	96
3.2.2.2 The Experiment	101

3.3	Adiabatic Following	104
3.3.1	Theoretical Formalism	105
3.3.2	The Inversion Probability P_π	108
3.3.2.1	Application to Cyclic Adiabatic Inversion	111
3.4	Future Adiabaticity Studies	112
Chapter 4. Field Effects on Oscillators Capped with Magnets		116
4.1	Motivation and Introduction	116
4.2	Experimental Details	119
4.3	Modelling of Data	124
4.3.1	High-Field Regime Model	124
4.3.2	Low-Field Regime Model	126
4.4	Notes	130
4.5	Conclusions with Application to NMR-FM	131
Chapter 5. Demonstration of Magnet-on-Oscillator NMR-FM		133
5.1	Experiment Overview	133
5.2	Magnets on Oscillators	135
5.3	Sample Preparation	140
5.3.1	Crystal Selection	140
5.3.2	Sample Mounting	141
5.4	Experimental Difficulties	143
5.4.1	Sample-Mediated Double Interference	144
5.4.2	Position Dependence of the Artifact	147
5.4.3	Tuning Dependence of the Artifact	152
5.5	Carrier Frequency Scan	155
5.5.1	Sub-Micron Resonance Slices	156
5.5.2	The Experiment	158
5.5.3	Nutation	164

Chapter 6. Future Work: NMR-FM Measurements of Magnesium Diboride	166
6.1 Future Work: MgB ₂	166
6.1.1 Feasibility Calculations	168
6.1.2 Experimental Plan and Considerations	171
6.1.3 Tangent-Wave Cyclic Adiabatic Inversion	173
6.2 Conclusion	180
Appendices	181
Appendix A. Launching into the Fiber	182
Appendix B. BNC Feedthrough Vacuum Compatibility	189
Bibliography	193
Vita	199

List of Tables

4.1	Oscillator characteristics and magnet dimensions used in this study.	119
6.1	Important values for the magnetization, expected force, force sensitivity, and signal-to-noise ratios at interesting temperatures. . . .	170
6.2	Values of the adiabaticity parameter and maximum manipulable magnetization for specific FM amplitudes assuming $H_1 = 5$ G. . .	171

List of Figures

1.1	Absorbption-emission cycle. The time-dependent potential causes the spins to harmonically flip.	8
1.2	Normalized NMR linewidth with a FWHM of $2g_N e B_1 / m_p$	8
1.3	\mathbf{H}_{eff} as seen in the rotating frame. The time-dependence of the \hat{z} component shown is used for cyclic adiabatic inversion of nuclear spins, wherein frequency modulation with modulation amplitude Ω is utilized.	11
1.4	Schematic of the effect that $\Pi/2$ and Π pulses have on the magnetization of a sample.	13
1.5	Magnet-on-oscillator experimental set up for NMR-FM.	16
1.6	Effective field in the \hat{z} direction during cyclic adiabatic inversion. The decay to resonance is important for initially bringing the magnetization parallel to \hat{x}' . The subsequent oscillations of the effective field about resonance are driven by frequency modulating the RF field; their result is the time-varying magnetization of the sample, which causes the force on the oscillator. The frequencies associated with the CAI cycle are indicated on the right.	18
1.7	Interrupted cyclic adiabatic inversion. This technique is used to manipulate spins whose relaxation rate is on the order of the oscillator resonance frequency.	22
1.8	Cyclic saturation. This technique is used when the relaxation rate of the spins is much greater than the resonance frequency of the oscillator.	23
1.9	Field gradient defines resonance slice. The size of the resonance slice is exaggerated for pedagogical purposes. A realistic resonance slice will be on the order of $1 \mu\text{m}$ or smaller.	24
1.10	SEMs of oscillators used in our lab. The top image is a triple-torsional oscillator made by Michelle Chabot while she was in this lab. The middle images are oscillators also made by Michelle Chabot, though these were made during her post-doc with John Moreland at NIST; we received them through a collaboration. The bottom SEM shows double-torsional oscillators made by Yong Lee with different moment of inertia ratios between the head and wing.	27

1.11	Schematic of the fiber optic interferometer with a block diagram of the feedback control.	30
1.12	The interference pattern formed by the displacement between the oscillator and the end of the fiber optic cable. This pattern was observed by using a quartered tube piezo to make small changes in the displacement (blue is extending, red is retracting). The displacement between maxima (or minima) is $\lambda/2$, while that from maximum to minimum is $\lambda/4$	30
1.13	X (red) and Y (blue) outputs of the lock-in on opposite sides of the head rise together slightly below resonance, indicating an in-phase relationship between X and Y. Because this phase relationship is the same on both sides of the head, we can conclude that this is a cantilever mode of the oscillator. Additional detection on the wings is necessary to specify the particular cantilever mode.	33
1.14	X (red) and Y (blue) outputs of the lock-in on opposite sides of the head behave oppositely slightly below resonance, indicating X and Y are out-of-phase. Because this phase relationship is opposite on opposite sides of the head, we can conclude that this is a torsional mode of the oscillator. Additional detection on the wings is necessary to specify the particular torsional mode.	34
2.1	Frequency scans of an oscillator resonance showing the effect of using different time constants. Quality factors of the resonance are indicated on each curve. From broadest to sharpest, the Q values correspond to time constants of 30 ms, 100 ms, 300 ms, and 1000 ms. The amplitude of the $\tau_c = 1000$ ms curve is shorter than the rest because the bandwidth was smaller than the step size and the peak was thus skipped over; a shorter step size would have revealed the peak amplitude equal to the others.	41
2.2	When using the ring-down method, the calculated mechanical quality factor plateaus at the oscillator's intrinsic Q for a given temperature and pressure. The line is a guide to the eye.	43
2.3	Example of $ G(f) ^2 S_F$ and its integral used in determining the spring constant of an oscillator.	46
2.4	Fringe lock circuit used to maintain a constant position and slope on the interference pattern during experiments.	49
2.5	Coordinate system for the probe.	50
2.6	A dip in the peak-to-peak amplitude of the interference pattern while moving the fiber in the \hat{y} direction is due to light escaping through the head-wing gap.	54
2.7	Head-wing gap seen by a severe dip in the peak-to-peak amplitude of the interference fringes.	55

2.8	Voltage divider used to apply variable voltage to the tube piezo quadrants. This setup extends the piezo, while using a positive voltage source retracts the piezo.	58
2.9	Interference pattern as a function of voltage applied to the four quadrants of the tube piezo. The non-linear contraction of the piezo is realized by the inequivalent voltage changes required to reach successive extrema of the pattern. The decrease of the peak-to-peak amplitude with applied voltage is caused by a decrease in intercepted light reflected from the target as the fiber-target distance is increased (the beam diverges).	59
2.10	Contraction of the tube piezo as a function of applied voltage. The major loop was performed first, followed in succession by the smaller loops. All five electrodes of the piezo were grounded upon returning to zero applied voltage.	60
2.11	Contraction of the tube piezo as a function of applied voltage. The major loop was performed first, followed in succession by the smaller loops. The electrodes were not grounded between loops, causing the sag in contraction.	61
2.12	Relaxation time measurement electronics circuitry.	62
2.13	Experimental demonstration of the Smooth-On functionality of the circuit. The extension of the sine wave (red) shows that there would have been a sudden change in the RF frequency when the CAI cycle was initiated if this part of the circuit did not exist. Such a discontinuity would be a diabatic process that could result in a loss of locked spins and therefore force signal.	66
2.14	Decay from above toward resonance as seen on a spectrum analyzer. The right peak corresponds to a frequency far above resonance, and the left peak is on resonance. The horizontal grid-lines are separated by 100 KHz. The width of the peak has been broadened by the spectrum analyzer.	67
2.15	FM portion of cyclic adiabatic inversion as seen on a spectrum analyzer. In this example, the FM amplitude $\Omega = \sim 50$ kHz. The horizontal grid-lines are separated by 100 kHz. The ghost of the off-resonance initial frequency can still be seen on the right side of the scope.	68
2.16	Spin-lattice relaxation time T_1 measurement sequence. Each curve is a digitized signal from the output of the electronics. The traces have been offset vertically for clarity.	70
2.17	Spin-spin relaxation time T_2 measurement sequence. Each curve is a digitized signal from the output of the electronics. The traces have been offset vertically for clarity.	71

2.18	Spin-lattice relaxation time $T_{1\rho}$ measurement sequence. Each curve is a digitized signal from the output of the electronics. The traces have been offset vertically for clarity.	72
2.19	Mechanical ringing occurs when the RF field is turned on or off.	74
2.20	Zoom showing the detail in the mechanical ringing. The oscillations have a frequency of 100 Hz.	75
2.21	Peak mechanical ringing amplitude as a function of RF power. The solid line is a fit of the data	75
2.22	The delay time for turn on of the FM shows the dependence of the oscillator ring-up on the presence of the FM. The amplitudes of the steady-state values are roughly 22 nm for each curve.	77
2.23	Steady state amplitude of the oscillator in the presence of FM as a function of RF power. The solid line is a fit of the data.	78
2.24	Beats due to a difference in FM modulation frequency and the oscillator resonance frequency. The blue curves on each are fits to a sine function.	79
2.25	Beat frequency of artifact as a function of the FM modulation frequency.	80
2.26	AC beat amplitude of the oscillator in the presence of FM as a function of FM modulation frequency.	80
2.27	Steady state amplitude of the artifact in the presence of FM as a function of FM amplitude. The solid line is a linear fit to the data, which yields $A/nm = 0.70 + 0.18\Omega/\text{kHz}$	81
2.28	Steady state amplitude of the oscillator artifact (blue) as a function of RF carrier frequency. Also shown (red) is the measured impedance of the tank circuit for each frequency.	81
2.29	Interference pattern showing the smooth “cold” side and the “hot” side of the fringe for four successive fringes. The data have not been corrected for the hysteresis of the tube piezo, so the fringes appear to have an unequal peak-to-peak separation.	83
2.30	Digitized lock-in signal as an external force is applied to the oscillator with the interferometer locked to the hot side of the fringe. The steady-state amplitude for $t < 0$ is the self-excitation. Only four curves are shown because otherwise the behavior would make the graph a mess. The AC voltage sent to the piezo plate is indicated for each curve. The strange behavior for the 112 mV curve is repeatable, and is included as an example of the oddity of the hot side response.	84

2.31	Digitized lock-in signal as an external force is applied to the oscillator with the interferometer locked to the cold side of the fringe. The AC voltage sent to the piezo plate is indicate for each curve. The steady-state driven amplitude scales linearly with the applied force. Note that the noise amplitudes are smaller than on the hot side.	85
2.32	Steady-state driven amplitude of the oscillators for the cold side (blue, vertical diamonds) and the hot side (red, horizontal diamonds). The linear behavior of the cold side implies that it may be reliably used for force measurements, while the odd response of the hot side implies that it cannot be used at this time.	85
2.33	Noise level for the cold side (blue, vertical diamonds) and the hot side (red, horizontal diamonds). These data support the conclusion that the cold side is usable and the hot side is not.	86
2.34	Phase relationship while being locked on the hot side before and after the driving force is applied. From bottom to top, the piezo plate's peak-to-peak driving voltages were 0.4 V, 0.5 V, 0.6 V, 0.7 V and 0.8 V. There is a transition at ~ 0.6 V, below which the phase of the oscillations smoothly incorporates the external force, and above which the phase is violently changed; the 0.6 V curve shows qualities of both regimes.	88
2.35	Phase relationship while being locked on the cold side before and after the driving force is applied. The curves are for different AC voltages sent to the piezo, but this is not the point of this graph. The point is to show the somewhat random nature of the phase for $t < 0$, which implies the absence of a significant driving force (i.e., there is no positive feedback loop). As a result, when the force from the piezo is applied, its (constant) phase is immediately assumed by the oscillator.	89
3.1	Maximum allowed magnetization in the \hat{z} direction as a function of the FM modulation amplitude Ω , according to Eq. 3.7. RF field strengths are indicated on each curve.	94
3.2	Maximum allowed magnetization in the \hat{z} direction as a function of the RF field strength H_1 , according to Eq. 3.7. FM modulation amplitudes are indicated on each curve.	95
3.3	Experimental setup for the sample-on-oscillator configuration used in this study.	97
3.4	Range of resonance frequency of the oscillator each day as a function of time throughout the experiment. The frequency always increased (almost linearly) from the low end to the high end of the ranges indicated. The increase in frequency is attributed to the liberation of water from the sample.	98

3.5	The modelled magnetic field (green) and magnetic field gradient (red) for the long bar magnet used in the experiment.	99
3.6	Data showing the normalized SNR as a function of the frequency modulation amplitude. The decrease in SNR is due to loss of spins because of violations of the adiabatic condition.	103
3.7	Data showing the normalized SNR as a function of the adiabaticity factor. The decrease in SNR is due to loss of spins because of violations of the adiabatic condition when the adiabaticity factor is small.	104
3.8	Adiabatic following probability vs adiabatic factor.	110
3.9	Adiabatic following with well-met adiabatic condition.	110
3.10	Experimental data using cyclic adiabatic inversion plotted with the theoretical curve for adiabatic following.	111
3.11	H_{eff} traces out an ellipse centered about H_1 with phase modulation if both the FM and AM have different modulation amplitudes. . .	113
3.12	Schematic representation of the components required for the effective field to trace out a circle centered at the origin. The colors are used to imply relative phase; blue is $\phi = 0$, and red is $\phi = \pi$	114
3.13	Effective field traces out a circle centered at the origin if appropriate measures are taken. The discontinuity in the curves near $x' = 0$ is the region where $H_{eff} \sim H_{local}$. The colors indicate different phase, as in Fig. 3.12.	115
4.1	Schematic overview of magnet-on-oscillator experimental setup. . .	118
4.2	Oscillators used in these experiments.	120
4.3	Normalized shift in resonant frequency for a bare paddle \circ and magnetically capped oscillators A, \square , B, ∇ , and C, \triangle	122
4.4	Quality factor dependance on field for a bare paddle \circ and magnetically capped oscillators A, \square , B, ∇ , and C, \triangle	123
4.5	Normalized shift in resonant frequency oscillator A ($1/8^{th}$ capped head, \square), and oscillator B ($1/2$ head capped, ∇). The solid line is a fit of the high field data to the model used previously by Rugar's group.	124
4.6	Schematic illustrating the coordinate system used in our low field model.	126
4.7	Fits to $1/8^{th}$ head magnet using the low field model is shown in red. The fit to the high field model is shown for completeness in gold. . .	129

5.1	Schematic overview of magnet-on-oscillator experimental setup to study the semi-infinite slab. Note that the external field is pointing in the opposite direction from our other NMR-FM studies. . . .	134
5.2	SEM showing the irregular geometry of 370 nm thick cylinders on the head of an oscillator. These thick magnets are deformed during the lift-off stage of the fabrication; thinner magnets are more uniform. .	136
5.3	Magnetic fields as functions of distance from the magnet along the axis of 180 nm thick cylindrical Permalloy magnets modelled using Eq. 5.3.	137
5.4	Magnetic field gradients as functions of distance from the magnet along the axis of 180 nm thick cylindrical Permalloy magnets modelled using Eq. 5.3. The solid and dotted straight lines indicate resonance slice thicknesses of 100 nm and 1000 nm taking the FM amplitude $\Omega/2\pi = 50$ kHz.	138
5.5	SEM of the oscillator type used to study the semi-infinite slab. The gradient-producing magnet is the small white spot in the middle of the head. The neck width and length are $3.00 \mu\text{m}$ and $130.0 \mu\text{m}$, the head is $30.0 \mu\text{m} \times 40.0 \mu\text{m}$, and the thickness is about 250 nm. . . .	138
5.6	Angled SEM of the oscillator type used to study the semi-infinite slab showing the thickness of the oscillator and the magnet. The cylindrical gradient-producing magnet shown is 180 nm thick and $\sim 5 \mu\text{m}$ in diameter. Working backward from the known tilt angle of the SEM and the bevel of the oscillator reveals a thickness of about 250 nm.	139
5.7	Setup for sample mounting using a graphite rod and three microscope slides. The slides only allow the rod to move in one direction and hold the crystal steady during mounting.	142
5.8	Artist's rendition of the double interferometer. In the normal interferometer, reflected waves B and C interfere. The double interference is observed when the light reflected from the sample-vacuum interface (wave D) enters the fiber and interferes with the normal interference pattern.	144

5.9	Interference patterns formed by changing the oscillator-fiber distance (left), and the sample-fiber distance. The left axis scale applies directly for only the red middle curve on each plot; the others were offset for clarity. The top curves have their initial DC level at the maximum of the pattern, the middle curves begin at the middle of the fringe (where we would normally lock with feedback), and the lower curves begin at the minimum DC level.	146
5.10	Experimental setup used to study the semi-infinite plane. The fiber was lowered and the sample was raised to avoid the double interference effect, though the latter is not evident in this picture.	148
5.11	Oscillator deflection amplitude during CAI cycle for five different frequencies for different sample positions. The initial position was chosen to be the reference position. Error bars are withheld for the sake of clarity, but are on the order of 80 mV.	149
5.12	Zoom of the interesting region of Fig. 5.11. Oscillator deflection amplitude during CAI cycle for five different frequencies for different sample positions. Error bars are withheld for the sake of clarity, but are on the order of 80 mV. The reference distance (0) was taken to be the point at which the sample touched the oscillator.	150
5.13	Oscillator response to a constant driving force for different sample-oscillator distances. The lowest amplitude group of curves correspond to the distances below the transition ($< \sim -20 \mu\text{m}$), and the largest amplitude group corresponds to the closest approach ($\sim 0 \mu\text{m}$). The origin of this amplified response is unknown.	152
5.14	Magnitude of signal artifact as a function of carrier frequency for two different tunings of the tank circuit. The two vertical dashed lines indicate the frequencies that were tuned using the Smith Chart function of a network analyzer. The difference between the tuned frequency and the frequency of minimum artifact may illustrate the systematic error in tuning (~ 3 parts in 10,000).	153
5.15	Magnitude of signal artifact as a function of carrier frequency taking phase into consideration. The vertical diamonds are the same data as shown in Fig. 5.14. The minimum magnitude of the artifact corresponds to a sign change in the phase of the signal, which we believe corresponds to the resonance frequency of the tank circuit.	154

5.16	Proton resonance frequency as a function of distance from the 4 μm diameter, 180 nm thick Permalloy magnet. The red horizontal line at 343.72 MHz is γH_0	155
5.17	Resonance slice center and bounds as a function of the carrier frequency. The slice thickness is determined by the distance between the upper and lower bound curves. The bound curves were calculated using an FM amplitude of 50 kHz.	156
5.18	Resonance slice thickness for different frequencies. The curve was calculated using an FM amplitude of 50 kHz and the normal equation for the slice thickness Δz . These experiments are our first experiences with sub-micron resonance slices.	157
5.19	Frequency scans of the mechanical oscillator. The scans were taken twice per carrier frequency throughout the experiment.	159
5.20	Raw data for all five frequency regimes investigated. The larger amplitude blue curves are artifact signals, and the lower amplitude red curves contain both the artifact and the NMR signals; the signal level decreases because the artifact and NMR forces are out of phase. The RF is turned on at $t = 0$ s, and goes off at 2.2 s; the embedded CAdI cycles begin at 70 ms, and end at 1.85 s.	161
5.21	Ring-up data during CAdI cycles for $f_c = f_{tuned}$. The larger amplitude blue curves are artifact signals, and the lower amplitude red curves contain both the artifact and the NMR signals; the signal level decreases because the artifact and NMR forces are out of phase.	162
5.22	NMR signal detected by scanning the carrier frequency to move the resonance slice position. The SNR is about 3.9, which is in accord with the expected improvement with $N = 4$ averages. The solid lines are the means for the artifact level (top) and the NMR signal (bottom) and the dashed lines are one standard deviation from the means. The error bars indicate the standard deviations of the steady-state levels of the ring-ups.	163
5.23	Raw data for each of the frequency groups used. The transition at the sample interface is seen for each of the frequencies, but the location of the shift is dependent on the detuning of the carrier frequency from the resonant frequency of the tank circuit. The shift is of unknown origin.	164

5.24	Typical results of nutation experiments with the resonance slice just inside the sample. Each data point is the peak value of an $N = 8$ averaged signal.	165
6.1	Unit cell of MgB_2 . The in-plane lattice parameter for the boron planes is $a = 0.3086$ nm, and the out-of-plane lattice parameter is $c = 0.3524$ nm.	168
6.2	Proposed piecewise inversion function for cyclic adiabatic inversion. Odd half-oscillator periods are composed of $-\tan(\omega_{osc}t)$, and even half-oscillator periods are $+\tan(\omega_{osc}t)$. The tangent functions are truncated and merged at $\omega_{osc}t = \pm\pi/4$	176
6.3	Adiabaticity factor of Eq. 6.21 as a function of the parameter n . The realistic parameters used were $\Omega = 2\pi \times 50$ kHz, $\gamma = 2\pi \times 13.66$ MHz/T, $H_1 = 3$ G, and $\omega_{osc}/2\pi$ are indicated. Because $1/\Lambda$ is significantly larger than one for $n = 1$, n should be taken as 1 for convenience. The shaded area indicates $1/\Lambda < 1$	179
B.1	BNC with the proper amount of epoxy. Any more epoxy will spill over the edge onto the threads.	191
B.2	Photographs of completed BNC feedthrough.	192

Chapter 1

Introduction to Nuclear Magnetic Resonance Force Microscopy with Literature Review

“Nōō’k-yōō-ler...it’s pronounced nōō’k-yōō-ler.”

- Homer Jay Simpson

This chapter gives a basic overview of essential material, including the theories of nuclear magnetic resonance (NMR) and NMR-force microscopy (NMR-FM). A detailed description of the experimental components of our microscope is given, with the differences between our techniques and those of other groups noted.

1.1 Nuclear Magnetic Resonance

1.1.1 Quantum Theory of the Two-State System

A simple account of nuclear magnetic resonance can be found in almost any introductory quantum mechanics book as an example of a real spin $1/2$ system with a time varying potential [1–3]. Here we present pertinent information for a background overview of NMR.

1.1.1.1 Overview

The total spin angular momentum of a nucleus is represented by \mathbf{I} , the spin quantum number by I , and the z-component by I_z . The magnitude of \mathbf{I} is given by $\sqrt{I(I+1)\hbar^2}$, where $[I(I+1)]\hbar^2$ is the eigenvalue of the operator I^2 . The eigenvalues of I_z are $m_I\hbar$, where $m_I \in [-I, -I+1, \dots, I-1, I]$. In the absence of a magnetic field all of these eigenstates have the same energy. When an external field is applied, a nucleus with spin \mathbf{I} has $2I+1$ equally spaced energy eigenstates. The energy in a magnetic field¹ is given by $-\vec{\mu} \cdot \mathbf{B}$, or by defining \hat{z} by the direction of the field, $E = -\mu_z B$, where μ_z is the \hat{z} component of the magnetic dipole moment. For nucleons, the magnetic moment $\vec{\mu}$ and its \hat{z} component μ_z are given respectively by $g_N\mu_N\mathbf{I}/\hbar$ and $g_N\mu_N m_I$, where g_N is the nuclear g-factor, and μ_N is the nuclear magneton (defined as $e\hbar/(2m_p)$). The coefficient $g_N\mu_N/\hbar$ defines the gyromagnetic ratio γ , which leads to the more familiar expressions $\vec{\mu} = \gamma\mathbf{I}$ and $\mu_z = \gamma\hbar m_I$. Then the energy reduces to $E = \gamma\hbar m_I B$ and the energy level spacing is given by

$$\Delta E = \gamma\hbar B. \tag{1.1}$$

The level spacing induced by the magnetic field defines the angular frequency necessary for resonance, the Larmor frequency, as $\omega = \gamma B$. When we apply an external field at the Larmor frequency, absorption allows low energy states to increase their energy, and spontaneous emission allows higher energy states to

¹Here we are using B for the magnetic field to avoid confusion with using H for both the field and the Hamiltonian. This will change in the next section.

decrease their energy. In the two-state system of protons, this simply means that at resonance some of the spins experience a magnetic dipole transition from the down state to the up state, and vice versa. The following discussion explains the details of the two-state system with quantum mechanical rigor.

1.1.1.2 Spin Precession in a Uniform Magnetic Field

The base kets we will use for the spin 1/2 system are $|\pm\rangle$. These are the eigenstates of the S_z operator, and their eigenvalues are $\pm\hbar/2$. The three coordinate operators are given in terms of the base set as

$$S_z = \frac{\hbar}{2} (|+\rangle\langle+| - |-\rangle\langle-|) \quad (1.2)$$

$$S_x = \frac{\hbar}{2} (|+\rangle\langle-| + |-\rangle\langle+|) \quad (1.3)$$

$$S_y = \frac{\hbar}{2} (-i|+\rangle\langle-| + i|-\rangle\langle+|). \quad (1.4)$$

The eigenstates for the S_x and S_y operators are

$$|S_x\pm\rangle = \frac{1}{\sqrt{2}} (|+\rangle \pm |-\rangle) \quad (1.5)$$

$$|S_y\pm\rangle = \frac{1}{\sqrt{2}} (|+\rangle \pm i|-\rangle). \quad (1.6)$$

For the specific case of a proton in a uniform time-independent magnetic field, B , pointed in the \hat{z} direction, the Hamiltonian is given by

$$H = - \left(\frac{g_N e B}{m_p} \right) S_z, \quad (1.7)$$

where e is the elementary charge, m_p is the mass of the proton, and c is the speed of light. Thus, the eigenstates of S_z are energy eigenstates (i.e.,

$[H, S_z] = 0$), and the eigenvalues are defined by

$$H | \pm \rangle = \mp \frac{\hbar}{2} \left(\frac{g_N e B}{m_p} \right) | \pm \rangle. \quad (1.8)$$

The signs of the energies in Eq. 1.8 indicate that $| + \rangle$ is the ground state, and $| - \rangle$ is the excited state. The energy difference between these two states is the amount of energy necessary to make a transition from one to the other. It is customary to use this level spacing to define the frequency

$$\omega \equiv \Delta E / \hbar = \frac{g_N e B}{m_p}. \quad (1.9)$$

Using this definition, we can rewrite the Hamiltonian of Eq. 1.7 as $H = \omega S_z$.

Let the state of our system at time $t = 0$ be given by

$$| \alpha(t = 0) \rangle = c_+ | + \rangle + c_- | - \rangle, \quad (1.10)$$

where probability conservation dictates that $| c_+ |^2 + | c_- |^2 = 1$. The state of the system at a later time, $| \alpha(t) \rangle$, is determined by applying the unitary time evolution operator, $U(t, 0) = \exp(-iHt/\hbar)$ to our initial state. Thus, the state at time t is given by

$$| \alpha(t) \rangle = c_+ e^{-i\omega t/2} | + \rangle + c_- e^{i\omega t/2} | - \rangle. \quad (1.11)$$

If we choose the initial state of the system to be spin up, then $c_+ = 1$, and $c_- = 0$. Applying the time evolution operator does nothing in this case, and the state of the system is eternally unchanged. This is clearly true because, as previously noted, S_z and H commute.

If we choose the initial state to be $|S_x+\rangle$, however, things change. In this case, $c_+ = 1/\sqrt{2}$, and $c_- = 1/\sqrt{2}$, and the state at time t is

$$|\alpha(t)\rangle = \frac{1}{\sqrt{2}} e^{-i\omega t/2} |+\rangle + \frac{1}{\sqrt{2}} e^{i\omega t/2} |-\rangle. \quad (1.12)$$

The state given in Eq. 1.12 is not stationary, so we'd like to figure out where it is going to end up. The way to do this is to determine the probability that the state will end up in any of $|S_x\pm\rangle$ in the future.

Recall that the probability of the state $|\alpha(t)\rangle$ being found in the state $|\beta\rangle$ is given by $|\langle\beta|\alpha(t)\rangle|^2$. We therefore find the probabilities of interest to be

$$|\langle S_x+|\alpha(t)\rangle|^2 = \cos^2 \omega t/2 \quad (1.13)$$

$$|\langle S_x-|\alpha(t)\rangle|^2 = \sin^2 \omega t/2. \quad (1.14)$$

The expectation values of the operators S_x, S_y and S_z are simply equal to the sum of the probabilities weighted by their eigenvalues. Thus, taking the results of Eqs. 1.13 and 1.14, and using similar arguments for S_y and S_z , leads us to the expectation values

$$\langle S_x \rangle = \frac{\hbar}{2} \cos \omega t \quad (1.15)$$

$$\langle S_y \rangle = \frac{\hbar}{2} \sin \omega t \quad (1.16)$$

$$\langle S_z \rangle = 0, \quad (1.17)$$

These expectation values tell us that the spin is precessing counter clockwise (viewed from $+\hat{z}$) in the $\hat{x}-\hat{y}$ plane due solely to the homogenous magnetic field.

1.1.1.3 Spin Magnetic Resonance

The time-dependent two-state problem is exactly solvable. The Hamiltonian of such a system can be written as

$$H = H_o + V(t), \quad (1.18)$$

where H_o is given in Eq. 1.7 and only the interaction potential V is time-dependent. Without this potential, the solutions to the Schrödinger equation are stationary states given as usual by $H | n \rangle = E_n | n \rangle$. The time-varying potential can cause transitions from one energy level to another, given that certain parameters of the potential are just right for two particular states.

In the explicit case of proton NMR, the time-independent part of the Hamiltonian is due to the large external magnetic field, B_o , the time-varying potential is a small radio-frequency magnetic field, B_1 , and the two particular states of interest are spin up, $| + \rangle$, and spin down, $| - \rangle$, of a proton's magnetic moment. The B_1 field is chosen to have the same time dependence as the natural precession of the spins (Eqs. 1.16 and 1.17). This field is therefore a counterclockwise circulating field (left circularly polarized) that is applied in the $\hat{x} - \hat{y}$ plane. The Hamiltonian is thus written as

$$\begin{aligned} H = & - \left(\frac{g_N e \hbar}{m_p} \frac{B_o}{2} \right) (| + \rangle \langle + | - | - \rangle \langle - |) \\ & - \left(\frac{g_N e \hbar}{m_p} \frac{B_1}{2} \right) \cos \omega_{RF} t (| + \rangle \langle - | + | - \rangle \langle + |) \\ & - \left(\frac{g_N e \hbar}{m_p} \frac{B_1}{2} \right) \sin \omega_{RF} t (-i | + \rangle \langle - | + i | - \rangle \langle + |), \end{aligned} \quad (1.19)$$

where e is the elementary charge, m_p is the mass of the proton, and ω_{RF} is the angular frequency of the time varying potential.

We take the state of this system at any time to be again given by Eq. 1.11. The coefficients $c_+(t)$ and $c_-(t)$ are determined by applying the time evolution operator to a set of initial conditions. For our case, we take the initial conditions to be $c_+(0) = 1$ and $c_-(0) = 0$, which is to say the spin is aligned with the external field. The probabilities of the spin being up or down at future time t are given by Rabi's formula

$$|c_-(t)|^2 = \frac{V^2/\hbar^2}{V^2/\hbar^2 + (\omega_{RF} - \omega_o)^2/4} \sin^2 \left(\sqrt{\frac{V^2}{\hbar^2} + \frac{(\omega_{RF} - \omega_o)^2}{4}} t \right) \quad (1.20)$$

$$|c_+(t)|^2 = 1 - |c_-(t)|^2, \quad (1.21)$$

where $V = \frac{g_N e \hbar}{m_p} B_1$.

Equations 1.20 and 1.21 show two important features. First, the probability of finding the system in the higher energy level (spin down state) is oscillatory with a frequency that depends on the "detuning" $\omega_{RF} - \omega_o$. Second, when the detuning is zero, the amplitude of $|c_-(t)|^2$ becomes large. This is the resonance condition. Figure 1.1 depicts the time evolution of the spin states, showing the cases of absorption (when the state flips to spin down) and emission (when the state returns to spin up). Additionally, Figure 1.2 shows the maximum amplitude of $|c_-(t)|^2$ as a function of RF frequency. The resonance curve has its peak at $\omega_{RF} = \omega_o$, and its full width at half maximum is $2g_N e B_1 / m_p$.

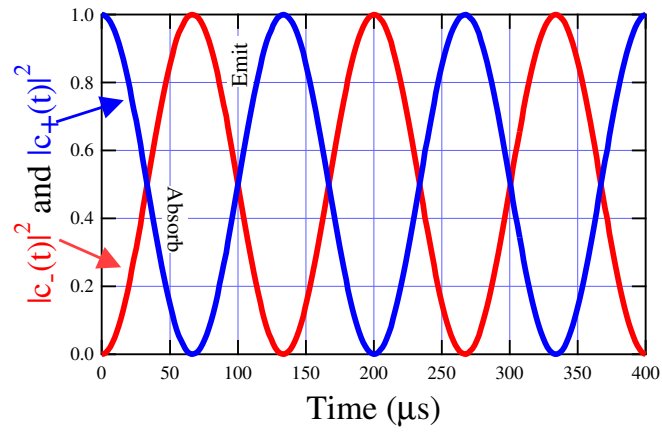


Figure 1.1: Absorption-emission cycle. The time-dependent potential causes the spins to harmonically flip.

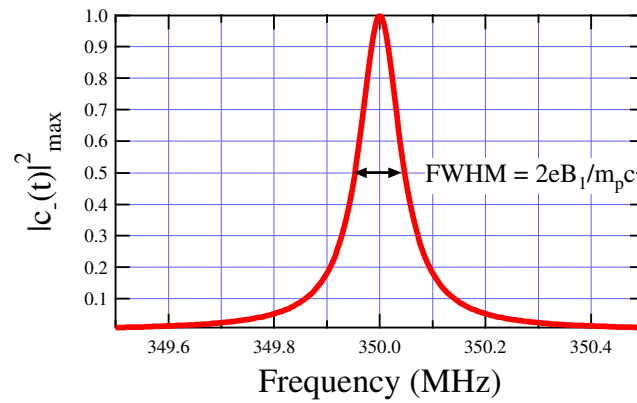


Figure 1.2: Normalized NMR linewidth with a FWHM of $2g_N e B_1 / m_p$.

1.1.2 Semi-Classical Theory

While the above quantum mechanical description of NMR is entirely correct, a more transparent account of the phenomenon is presented here. Several excellent sources can complement the following discussion [4–8].

Spins placed in magnetic fields experience a torque, causing them to precess at the Larmor frequency. The Larmor frequency is equal to the product of the gyromagnetic ratio of the spin and the field strength

$$\omega_o = \gamma H_o. \quad (1.22)$$

The gyromagnetic ratio (more correctly, $\gamma/2\pi$) of protons is 42.577 MHz/T, yielding a resonance frequency in an 8.1 T NMR magnet of 344.82 MHz. The field-induced torque \mathbf{N} is the cross product of the magnetic moment of the spin and the field

$$\mathbf{N} = \vec{\mu} \times \mathbf{H}_o. \quad (1.23)$$

As torque is the time rate of change of angular momentum, so we also have

$$\frac{d\mathbf{J}}{dt} = \vec{\mu} \times \mathbf{H}_o. \quad (1.24)$$

The equations of motion of the net magnetic moment of a sample are given by

$$\frac{d\mathbf{M}}{dt} = \gamma \mathbf{M} \times \mathbf{H}_o, \quad (1.25)$$

where we have used $\mathbf{M} = \gamma \mathbf{J}$.

As above, a time varying potential in the form of a circular RF magnetic field, \mathbf{H}_1 , is applied perpendicular to \mathbf{H}_o in order to induce magnetic resonance.

As it is difficult to generate a circular magnetic field using a simple coil, our \mathbf{H}_1 field is actually a linear field applied in the \hat{x} direction given by $H_{RF} = 2H_1 \cos \omega_{RF}t$. The linear field can be written as the sum of two oppositely rotating circular fields

$$\mathbf{H}_{RF} = \mathbf{H}_- + \mathbf{H}_+$$

with

$$\mathbf{H}_- = H_1 (\cos(\omega_{RF}t)\hat{x} + \sin(\omega_{RF}t)\hat{y}) \quad (1.26)$$

$$\mathbf{H}_+ = H_1 (\cos(\omega_{RF}t)\hat{x} - \sin(\omega_{RF}t)\hat{y}). \quad (1.27)$$

Because of their natural tendency for precession, the spins will only absorb the left circularly polarized radiation of Eq. 1.26 in a resonant fashion. Thus, the RF field of interest for us is

$$\mathbf{H}_- = H_1 \cos(\omega_{RF}t)\hat{x} + H_1 \sin(\omega_{RF}t)\hat{y}. \quad (1.28)$$

The description of NMR becomes much easier if at this point we perform a coordinate transformation from the lab frame $(\hat{x}, \hat{y}, \hat{z})$ to the frame rotating with H_1 $(\hat{x}', \hat{y}', \hat{z})$. In the rotating frame, Eqs. 1.25 become

$$\frac{d\mathbf{M}}{dt} = \gamma\mathbf{M} \times \left([H_o - \frac{\omega_{RF}}{\gamma}]\hat{z} + H_1\hat{x}' \right). \quad (1.29)$$

The term in parentheses defines the effective field, \mathbf{H}_{eff} , which is the field seen by the spins.

The effective field shows two interesting features. First, its \hat{x}' component is constant in the rotating frame. Second, its \hat{z} component is frequency

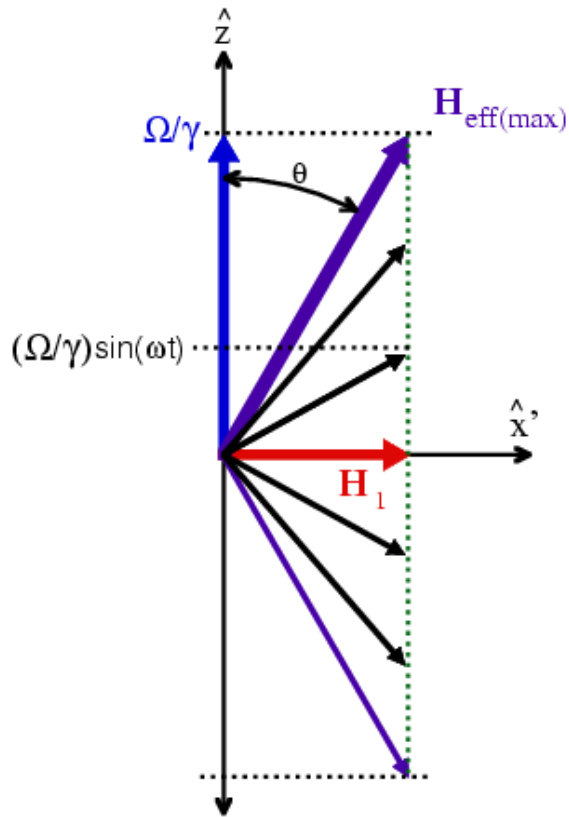


Figure 1.3: \mathbf{H}_{eff} as seen in the rotating frame. The time-dependence of the \hat{z} component shown is used for cyclic adiabatic inversion of nuclear spins, wherein frequency modulation with modulation amplitude Ω is utilized.

dependent. When the frequency of the RF exactly matches the Larmor frequency of the nuclei, we see that $\mathbf{H}_{eff} = H_1 \hat{x}'$. This is the condition for resonance. Figure 1.3 illustrates the effective field in the rotating frame during the process of cyclic adiabatic inversion (see below). The parameter Ω/γ is the deviation of the \hat{z} component of \mathbf{H}_{eff} from resonance, and can be controlled by changing the frequency ω_{RF} .

1.1.3 NMR Spin Manipulation Techniques

In conventional NMR, the spins are generally manipulated with RF pulses of various duration that are on resonance (meaning $\omega_{RF} = \omega_o$). If the RF field H_1 is turned on abruptly, the spins are suddenly exposed to a new effective field that is orthogonal to the previous field. One may think about this situation from the perspective of the field, in which case the spins are now oriented in the plane perpendicular to it. In this case, the spins are not in an eigenstate of the new Hamiltonian, and their expectation values will oscillate with frequency $\omega_1 = \gamma H_1$. From the spin's point of view, the effective field has changed suddenly and is now imposing a torque that will make them rotate in the $\hat{y}'-\hat{z}$ plane. Because of this torque, the RF pulse can cause the magnetization to rotate by an angle θ from its equilibrium position if it is left on for the explicit amount of time $t = \theta/\omega_1$. The most common RF pulses used in NMR are illustrated in Fig. 1.4. These pulses are aptly referred to as $\pi/2$ and π pulses as they rotate the magnetization by $\theta = \pi/2$ and $\theta = \pi$. In calculating the duration of these pulses, one should be certain to use the RF

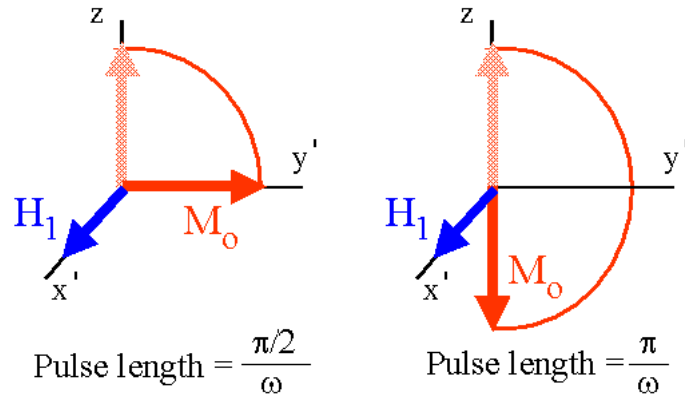


Figure 1.4: Schematic of the effect that $\Pi/2$ and Π pulses have on the magnetization of a sample.

magnetic field strength H_1 , not the homogenous field strength H_o .

One other relevant conventional NMR technique is adiabatic rapid passage. In such a scheme, the frequency of the RF is swept from far above resonance to far below resonance. As Eq. 1.29 implies, doing this inverts the \hat{z} component of the effective field. If the rate of change of the field is slow compared to the angular frequency of the spins about the effective field, then the spins will “follow” the effective field, which results in an inversion of the population of spins (i.e., all spin up nuclei become spin down, and vice versa). Some conventional NMR experiments use this inversion technique in order to steer the magnetization of a sample into the high energy state, then monitor the magnetization as it returns to the ground state; timescales of equilibration are important characteristics of spin systems, and are known generally as relaxation times.

1.1.4 Spin-Lattice and Spin-Spin Relaxation Times

One major use of NMR is to measure relaxation times of nuclei in a polarized sample. Relaxation times shed light on interactions of individual spins with their environment, be it the lattice or neighboring spins. The two fundamental relaxation times are T_1 and T_2 , known respectively as the spin-lattice and spin-spin relaxation times.

The spin-lattice relaxation time T_1 tells us the timescale on which spins come to equilibrium with the lattice. The population difference between spin up and spin down is proportional to the Boltzmann factor

$$\frac{N_{|+\rangle}}{N_{|-\rangle}} = e^{-\Delta E/k_B T}. \quad (1.30)$$

If the magnetization of the sample is destroyed (via a saturation comb of $\pi/2$ pulses), then there is no population difference between the spin states. By introducing a concept known as the “lattice temperature”, we can see that such a state of the system corresponds to having an infinite lattice temperature, since $\exp(-\Delta E/k_B \infty) = 0$. The real temperature of the lattice is not infinite, so the system will eventually “relax” back to a state where the Boltzmann factor accurately describes the population difference with a finite temperature difference; the timescale of this process is proportional to $\exp(-t/T_1)$. If the magnetization of the sample is measured during the relaxation process, then the data can be fit to determine the spin-lattice relaxation time.

The coupling between spins transversely allows energy to be transferred between spins on the time scale T_2 . This spin-spin relaxation time is generally

described as being due to differences in the absolute field that a spin sees because of the fluctuating local dipole fields from its neighbors. Because of this distribution in local fluctuating fields, some spins precess faster than others in the transverse plane, and the relative phases of the precessions quickly become washed away. The timescale on which the relative phase information is lost is the spin-spin relaxation time.

1.2 NMR Force Microscopy Theory

The theory of NMR-force microscopy was first presented by John Sidles in 1991 [9]. The basic idea is that if the moment of a sample, \mathbf{M} , is modulated in time near a magnetic particle whose field gradient is $\nabla\mathbf{B}$, then there will be an oscillatory force coupling the two given by

$$\mathbf{F}(t) = \mathbf{M}(t) \cdot \nabla\mathbf{B}. \quad (1.31)$$

In practice, as illustrated in Fig. 1.5, the magnetic particle is mounted on a very low spring constant, k , mechanical oscillator, whose deflection due to the force $\mathbf{F}(t)$ is detected with a fiber optic interferometer. If the sample's magnetization varies in time with a frequency equal to that of the resonance frequency of the oscillator, then the amplitude of the deflection, A , is increased by the quality factor, Q , of the oscillator so that

$$A = Q \frac{F}{k}. \quad (1.32)$$

The minimum detectable force (i.e., the force sensitivity) of an NMR-FM experiment is limited by the thermal noise of the mechanical oscillator, and

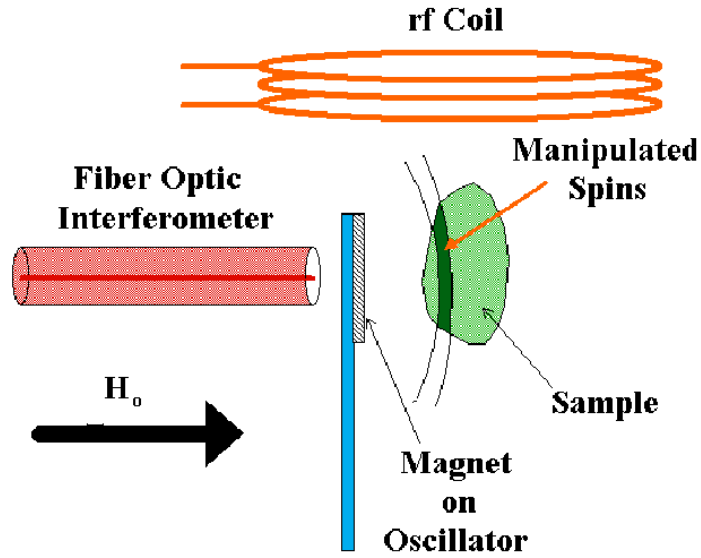


Figure 1.5: Magnet-on-oscillator experimental set up for NMR-FM.

can be written as

$$F_{min} = \sqrt{\frac{4k_{osc} k_B T \Delta\nu}{\omega_{osc} Q}}, \quad (1.33)$$

where k_{osc} , ω_{osc} , and Q are the spring constant, resonance frequency, and quality factors of the mechanical oscillator, and $\Delta\nu$ is the “equivalent noise bandwidth” of the measurement.

1.2.1 Cyclic Adiabatic Inversion

The primary technique used for spin manipulation in NMR-FM is cyclic adiabatic inversion. This technique is superficially identical to the conventional adiabatic rapid passage technique. However, instead of one sweeping pass, cyclic adiabatic inversion repeats many small adiabatic rapid passages so as

to make \mathbf{M}_z not only $\mathbf{M}_z(t)$, but also highly periodic.

In practice, cyclic adiabatic inversion is performed after a decay from far off resonance toward resonance. The reason for this is to slowly tilt the angle of the effective field (very high or low frequencies make \mathbf{H}_{eff} roughly parallel to \mathbf{H}_o). The initial frequency is usually taken to be 300-500 kHz above resonance. Because the Larmor frequency of the spins is 350 MHz, it may seem that such a small deviation from resonance would be insignificant. This is not the case, however, as the important parameter is the angle the effective field makes with the polarizing field, namely $\theta = \tan^{-1} \left(\frac{\mathbf{H}_{eff} \cdot \hat{z}}{\mathbf{H}_{eff} \cdot \hat{x}} \right)$. Figure 1.6 illustrates a real cyclic adiabatic inversion time series by showing its effect on $\mathbf{H}_{eff} \hat{z}$.

Recall that the effective field is given by

$$\mathbf{H}_{eff} = \left([H_o - \frac{\omega_{RF}}{\gamma}] \hat{z} + H_1 \hat{x}' \right). \quad (1.34)$$

If we introduce a frequency modulated wave, then $\omega_{RF} = \omega_{RF}(t)$. We choose the carrier frequency of the FM to be ω_o , the frequency of the modulation to be ω_{FM} , and define the amplitude of the FM as Ω . The frequency of the RF is thus given by

$$\omega_{RF}(t) = \omega_o + \Omega \cos(\omega_{FM}t). \quad (1.35)$$

The effective field will then have a modulating \hat{z} component given by

$$H_{eff} \hat{z} = H_o - \frac{1}{\gamma} (\omega_o + \Omega \cos(\omega_{FM}t)). \quad (1.36)$$

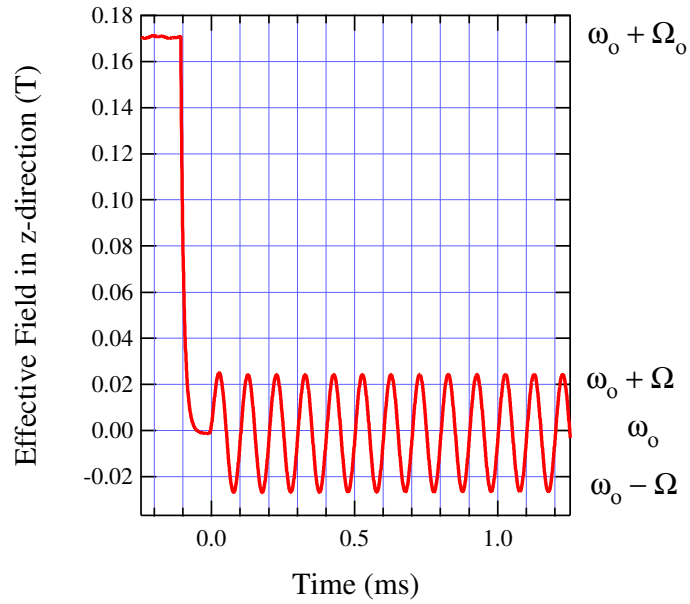


Figure 1.6: Effective field in the \hat{z} direction during cyclic adiabatic inversion. The decay to resonance is important for initially bringing the magnetization parallel to \hat{x}' . The subsequent oscillations of the effective field about resonance are driven by frequency modulating the RF field; their result is the time-varying magnetization of the sample, which causes the force on the oscillator. The frequencies associated with the CADI cycle are indicated on the right.

The result of the time varying $H_{eff}\hat{z}$ is a time varying magnetization. Recalling Eq. 1.31, we see this then results in a time varying force. If we choose the modulation frequency to equal the resonance frequency of the mechanical oscillator onto which the sample or field-gradient-producing magnet is mounted, then the mechanical oscillator will be resonantly excited by the time varying force².

1.3 The Basic MRFM Experiment and Its Components

The basic MRFM³. experiment has five main components, each with its own fundamental importance to the experiment (Fig. 1.5): an RF coil, a field gradient-supplying magnet, a mechanical oscillator, a fiber optic interferometer, and a sample to investigate. In addition to these elements, our experiments have a homogenous external magnetic field that serves to polarize the sample spins and make certain that the gradient-supplying magnet is saturated⁴.

The experiment itself goes something like this: spins in a sample, ini-

²The Army group has exploited the sensitivity of the interferometer to perform MRFM experiments off resonance [10]. In principle, there is no problem with this, but having the factor of Q (from the oscillator resonance) in your signal is always helpful.

³I use MRFM here because the following discussion references work done by other groups on not only NMR, but also electron spin resonance (ESR) and ferromagnetic resonance (FMR).

⁴The homogeneous external field does not necessarily need to be produced by an NMR magnet; a strong permanent magnet will also polarize the spins of the sample, though in this case there will be a field gradient present that will result in different fields within the sample-this may be advantageous for obtaining smaller resonance slices, but would be detrimental if not realized before performing such an experiment.

tially polarized in the \hat{z} direction, are coerced by an AC RF magnetic field to invert their spins such that the \hat{z} component of sample's magnetization is inverted at a frequency equal to the resonance frequency of the mechanical oscillator. Because the sample is also exposed to the magnetic field gradient of a particle attached to the oscillator, there is an oscillating force imposed on the oscillator. Because the magnetization of the sample, and therefore the force, is varied at the resonance frequency of the mechanical oscillator, the oscillator is resonantly excited. The amplitude of the response is proportional to the force and the oscillator's quality factor, while it is inversely proportional to the spring constant. This motion is detected by the interferometer, constituting the force detection of magnetic resonance.

1.3.1 The RF Coil

The RF coil is used to manipulate the magnetization of the sample through various modulation schemes. Recalling the equation for the effective magnetic field in the rotating frame (Fig. 1.3, we see that the RF can make the \hat{z} component of this field time dependent through frequency modulation. We can also make this component time dependent through amplitude modulation, though this is not regularly used because experiments have shown that AM results in a greater signal artifact than FM [11]. In any event, in order for the RF field to affect the spins of the sample, its magnitude must be greater than that of the local nuclear magnetic fields (2-5 Gauss).

1.3.1.1 Relaxation Time Measurements

The RF coil is at the heart of making relaxation time measurements. Through various pulse sequences, the magnetization of the sample can be set to some initial condition, and then after waiting some variable amount of time the \hat{z} component of the magnetization can be measured by performing cyclic adiabatic inversion (or whichever inversion scheme is appropriate). In this manner we can make measurements of the spin-lattice (T_1), rotating frame spin-lattice ($T_{1\rho}$), and spin-spin relaxation (T_2) times.

One area of current investigation is the determination of the relaxation time during cyclic adiabatic inversion, T_{CAI} . This relaxation time is bounded by T_1 and $T_{1\rho}$. T_{CAI} should approach T_1 for large frequency modulation amplitudes Ω/γ and small RF fields H_1 , while it should approach $T_{1\rho}$ for large H_1 and small Ω/γ .

1.3.1.2 Spin Manipulation Regimes

There are three relaxation time dependent regimes of RF spin manipulation, namely, cyclic adiabatic inversion, interrupted cyclic adiabatic inversion, and cyclic saturation. The relaxation of spins during manipulation is a great detriment to signal strength, and is one of the main focuses of ongoing research [12–15]. Each of these regimes is used to maximize the strength of the signal, that is, to actively manipulate the greatest number of spins possible.

For samples with relaxation rates much slower than the resonant frequency of the mechanical oscillator, cyclic adiabatic inversion is used. In this

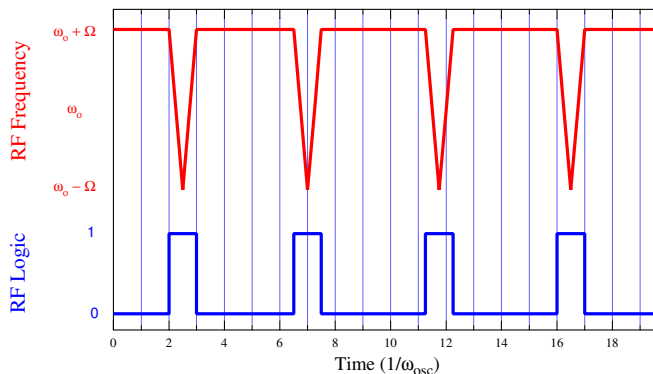


Figure 1.7: Interrupted cyclic adiabatic inversion. This technique is used to manipulate spins whose relaxation rate is on the order of the oscillator resonance frequency.

case, the effective magnetic field looks essentially static to the spins precessing about it. When the spins are locked to the field in this manner, they readily follow it as we modulate its \hat{z} component, resulting in the time dependent magnetization that will excite the mechanical oscillator. In these samples with large relaxation times, the spins will lock to the effective field for thousands of cycles before beginning to relax.

When the relaxation rate is on the order of the resonant frequency of the mechanical oscillator, interrupted cyclic adiabatic inversion is used. In this case, the spins will lock to the effective field for a short time allowing cyclic adiabatic inversion, but they relax after only a few cycles. To combat this problem, the RF is periodically turned off to allow the sample to fully saturate along the external field, as illustrated in Fig. 1.7. It is important that the RF be on for only a few oscillator periods to minimize the recovery time of the magnetization. More importantly, the RF should be off for a whole

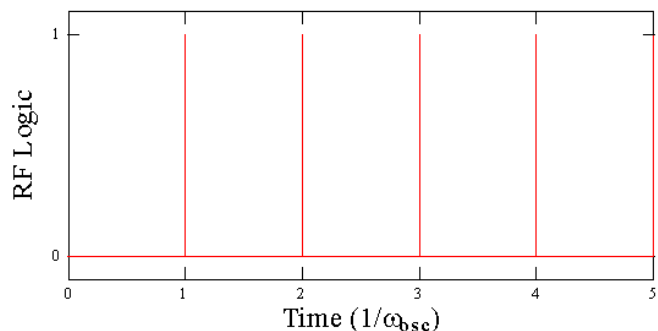


Figure 1.8: Cyclic saturation. This technique is used when the relaxation rate of the spins is much greater than the resonance frequency of the oscillator.

number of oscillator periods so that once it is turned on again, the new force is constructively synchronized with the previous forces in order to readily excite the oscillator. This technique is not quite as efficient as pure cyclic adiabatic inversion because the oscillator will not ring up as easily without a continuous driving force, but is the only option for relaxation rates of this intermediate sort.

If the relaxation rate of the sample is much greater than the resonant frequency of the mechanical oscillator, cyclic saturation is used. In this case, most of the spins will relax from the effective field within one oscillator period. The idea here is simply that of a classical kicked rotor, where the oscillator is the rotor and the kick is a quick change in the magnetization, as depicted in Fig. 1.8. One method of cyclic saturation is to use amplitude modulation by turning on and off with H_1 on resonance. This is as simple as applying a train of π pulses ($\pi = \omega_o t$) to the sample in order to invert M . The pulses must

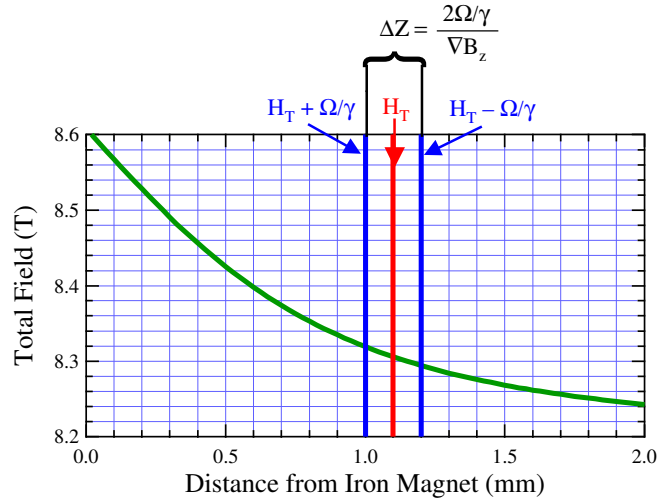


Figure 1.9: Field gradient defines resonance slice. The size of the resonance slice is exaggerated for pedagogical purposes. A realistic resonance slice will be on the order of $1 \mu\text{m}$ or smaller.

come at a repetition rate equal to the resonance frequency of the oscillator so that these quick changes in the magnetization will coherently ring up the oscillator.

1.3.2 Magnetic Field Gradient

The next component of the basic MRFM experiment is a magnetic field gradient. In the early days, the field gradient was supplied by a large permanent magnet [11, 16–18]. The magnitude of the field gradient is important because without it, there would be no force coupled to the mechanical oscillator ($\mathbf{F} = \mathbf{M} \cdot \nabla \mathbf{B}$). As shown in Fig. 1.9 the field gradient helps to define

the thickness of the resonance slice as

$$\Delta z = 2\Omega/\gamma \nabla_z B. \quad (1.37)$$

Large field gradients are thus beneficial for high-resolution microscopy. To this end, many researchers, our group included, have adopted the magnet-on-cantilever geometry, as tiny magnets yield large field gradients. The search for a single spin is much more difficult (at this time) when using small magnets in close proximity to a sample because magnetic noise fluctuations tend to increase the relaxation rate of the spins [13]. Less ambitious experiments may not have such difficulty.

One important point to note is that the field gradient does not affect the strength of the signal if the resonance slice is completely submerged within a sample. This is not obvious because the force equation seems to suggest that the force increases with the gradient. However, the \mathbf{M} in the force equation is magnetization, not magnetization per unit volume. If the resonant slice thickness Δz is less than the thickness of the sample (as it should be for a meaningful imaging experiment), the volume of spins in the resonant slice is inversely proportional to the field gradient. The force equation could then be written more explicitly as

$$F = n A \Delta z \frac{\gamma^2 \hbar^2 I(I+1)}{3k_B T} H_o \nabla_z B, \quad (1.38)$$

where $A \Delta z$ is the volume of the sample contained in the resonance slice. Using Eq. 1.37, the field gradient drops out of the equation and the force reduces to

$$F = n \frac{\gamma^2 \hbar^2 I(I+1)}{3k_B T} H_o \frac{2\Omega A}{\gamma}. \quad (1.39)$$

Thus, we see the force on the oscillator is independent of the field gradient in this case.

1.3.3 Mechanical Oscillators

The mechanical oscillator is another very important element of the basic MRFM experiment. The oscillator provides us with a way to detect extremely small forces created by an extremely small time-varying magnetization. The thermal noise of the mechanical oscillator is the limiting factor of the sensitivity of current experiments, though magnetic noise and proximity effects (such as the Casimir force) have the potential to limit future experiments [13, 19]. The thermal noise force on a mechanical oscillator is given by $F = \sqrt{S_f \Delta\nu}$, where the spectral density S_f is $4k_{osc}k_B T / (\omega_{osc}Q)$. For a given bandwidth, the most sensitive oscillator will have $k \rightarrow 0$, and resonant frequency and quality factors tending toward infinity, and will operate at 0 K. As such, much effort has been put into constructing oscillators with small spring constants, high frequencies, and large quality factors [18, 20–23]. Scanning electron microscope images of several oscillator designs are presented in Fig. 1.10. One of the main focuses of our group, but not of this particular work, is to produce torsional oscillators. The torsional design will be used to obtain quality factors orders of magnitude greater than simple cantilevers. While high sensitivity experiments are performed at low temperature, room temperature MRFM experiments are performed regularly [16, 18, 24–26]. Experimental issues with each of these sensitivity parameters are addressed below.

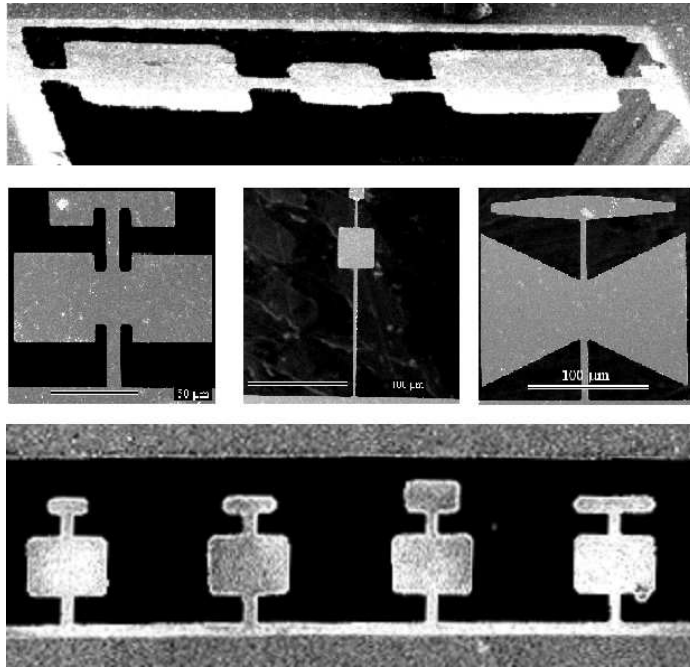


Figure 1.10: SEMs of oscillators used in our lab. The top image is a triple-torsional oscillator made by Michelle Chabot while she was in this lab. The middle images are oscillators also made by Michelle Chabot, though these were made during her post-doc with John Moreland at NIST; we received them through a collaboration. The bottom SEM shows double-torsional oscillators made by Yong Lee with different moment of inertia ratios between the head and wing.

Realizing each “optimal” oscillator characteristic has its downfalls. The best way to achieve low spring constants is to make extremely thin oscillators as $k \propto t^3$ [27]. The most sensitive oscillators demonstrated are 60 nm thick [21] and have $k \sim 10^{-6}$ N/m. Our oscillators are typically in the range of 200 - 300 nm thick and have $k = 10^{-2}$ N/m. The equipartition theorem, however, tells us that a small spring constant implies a large RMS amplitude at a given temperature $\langle x^2 \rangle = k_B T / k_{osc}$. This is not a problem for experiments where the resonant slice is much greater than the RMS amplitude. However, for high-resolution experiments where the resonant slice is on the order of or smaller than this amplitude, the problem is detrimental. One solution to this problem is the use of active feedback, which artificially reduces the RMS amplitude to reasonable levels [28, 29].

Although high resonant frequency oscillators would increase force sensitivity, they are not desired due to the adiabatic condition garnering spin locking. The adiabatic condition depends on the type of modulation scheme implemented, but basically says that spins will readily lock to the effective field if the Larmor frequency about the effective field is much greater than the angular frequency of the effective field. For sinusoidal FM with frequency modulation amplitude Ω/γ , the adiabatic conditional statement⁵ is $(\gamma H_1)^2 / (\omega \Omega) \gg 1$. The only oscillator characteristic that enters this statement is the resonant frequency, and we clearly want it to be low.

⁵Some groups like to define the conditional statement so that values much less than one imply good spin locking. I think this is ridiculous. With the conditional statement defined in this work, the bigger the number, the better the spins are locked. . . psychoanalyze that!

Oscillators with large quality factors can adversely affect the experiment due to long ring-up times. The time it takes an oscillator to reach its steady state amplitude is several characteristic times τ , where $\tau = Q/\omega$. Extremely high Q oscillators will take many cycles of adiabatic inversion to reach their maximum amplitude (where the signal would be the largest). Depending on the spin relaxation time during inversion, it is conceivable that most of the spins may be lost by the time the oscillator rings up to its full amplitude [15, 27]. Long ring up times are unacceptable for imaging purposes (the brightness of a pixel in an image corresponds to the measured force at that point in space. . .one image is made of lots of pixels). Conveniently, the solution to this problem is the same as that of the small spring constant problem, namely, active feedback. Active feedback has been used to artificially damp the quality factor of mechanical oscillators by up to three orders of magnitude [28, 29]. This technique decreases the response time of oscillators to a level that imaging experiments are now regularly performed [30, 31].

1.3.4 Fiber Optic Interferometer

The fiber optic interferometer is essential to the force detection of MRFM. Light from a laser diode is coupled to a fiber optic cable, sent through a directional coupler, and then out of the fiber toward the oscillator. Light reflects from the oscillator back into the fiber, where it then forms an interference pattern with the light that internally reflected from the cleave back down the fiber (see Figs. 1.11 and 1.12). The maximum amount of light re-

Fiber Optic Interferometer

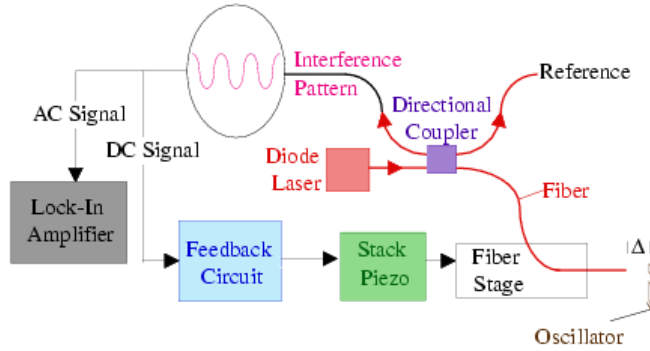


Figure 1.11: Schematic of the fiber optic interferometer with a block diagram of the feedback control.

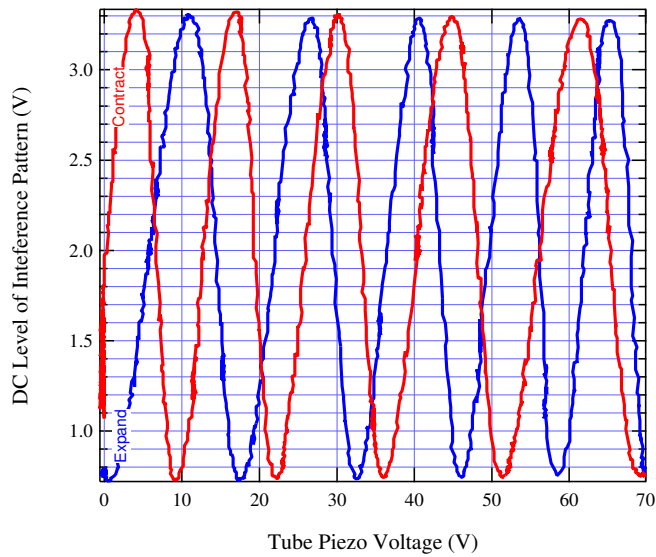


Figure 1.12: The interference pattern formed by the displacement between the oscillator and the end of the fiber optic cable. This pattern was observed by using a quartered tube piezo to make small changes in the displacement (blue is extending, red is retracting). The displacement between maxima (or minima) is $\lambda/2$, while that from maximum to minimum is $\lambda/4$.

flected back down the fiber due to the impedance mismatch going from the fiber to air is only four percent of the incident power [27]. Other groups have improved upon this by coating the fiber with a thin layer of silicon [32]. A photodiode and associated circuitry converts the interfering light power to a proportional voltage; a photodiode responsivity of 0.6 A/W and an amplifier gain of 2×10^6 V/A yield an overall sensitivity of about 600 mV/ μ W. The signal from the photodiode pre-amp circuit is sent to a fringe stability feedback circuit and to a lock-in amplifier. This signal is an AC voltage superimposed on top of a DC voltage. The AC component is due explicitly to the vibration amplitude of the oscillator (and is thus extraordinarily small), and the DC offset is the voltage amplitude of the interference pattern. The fringe stability circuit monitors the low frequency amplitude drifts of the interference pattern and outputs a voltage to a stacked piezo transducer to adjust the position of the fiber relative to the oscillator in order to maintain the set-point DC level⁶. This feedback allows us to lock on the largest slope (right in the center) of an interference fringe, where the sensitivity of the interferometer is greatest and relatively independent of position. Changes in the DC level are due to thermal drift and a lack of vibration isolation. The ability to lock on a fringe is increased to an ideal level when the probe is vibrationally isolated by floating on a half-inflated rubber inner tube⁷. During the experiment, however, the

⁶This “DC level” is the voltage corresponding to the amplitude of the actual interference pattern due to the separation of the fiber and the oscillator, not an offset of the interference pattern.

⁷This vibration isolation technique, while seemingly crude, is used regularly for scanning tunnelling microscopy, which needs far better isolation than NMR-FM currently does.

probe is not quite as well isolated, but the NMR magnet itself has much better vibration isolation than any lab bench. The vibrations seen in the magnet are probably transmitted through the stainless steel vacuum hoses.

The fiber optic interferometer is capable of detecting motion less than 0.01 \AA . This is much better than what we currently need [27]. Other groups have improved this detection limit by thermally tuning their laser [33]. The basic idea here is that the wavelength of light output by the laser depends on the temperature of the laser. By adjusting the wavelength in this manner, they are able to maintain a constant DC level. This technique essentially eliminates the need for the fringe stability piezo.

1.3.5 Lock-in Amplifier

The lock-in amplifier monitors the AC part of the light pattern due to the small changes in the displacement of the fiber and oscillator due to the vibration amplitude of the oscillator. It basically determines the Fourier component of the signal within a given frequency bandwidth. The outputs of the lock-in are typically the elastic and the absorptive amplitudes, X and Y . We can use these to determine the amplitude R and phase Θ of the signal at a single instant in time. An oscillator resonance during a frequency scan is identified by the point at which the elastic amplitude is zero and the absorptive amplitude is maximum. Because the lock-in is a phase sensitive device, we can determine the relative phase of different oscillator modes; just before reaching resonance, if the elastic and absorption amplitudes increase

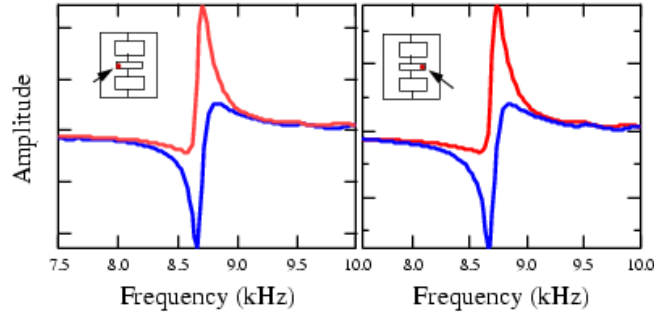


Figure 1.13: X (red) and Y (blue) outputs of the lock-in on opposite sides of the head rise together slightly below resonance, indicating an in-phase relationship between X and Y. Because this phase relationship is the same on both sides of the head, we can conclude that this is a cantilever mode of the oscillator. Additional detection on the wings is necessary to specify the particular cantilever mode.

together they are in phase, but if one increases while the other decreases, they are out of phase. By pointing at different positions of the oscillator (left and right sides of the head and wing) and noting the phase relations at these points, we can uniquely determine the mode of a resonance. Figures 1.13 and 1.14 show phase sensitive detection of the lower and upper torsional modes of a triple torsional oscillator. Lower cantilever and torsional modes will have both sides of the head and wing in-phase, but torsional modes will show the left and right of either the head or wing to be out of phase. Similar reasoning can be applied to the other modes [18].

1.3.6 The Sample

The final component essential to an MRFM experiment is the sample itself. This is the most complex component of the entire experiment. The choice

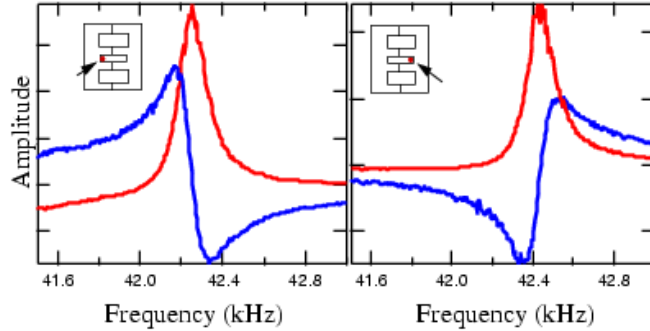


Figure 1.14: X (red) and Y (blue) outputs of the lock-in on opposite sides of the head behave oppositely slightly below resonance, indicating X and Y are out-of-phase. Because this phase relationship is opposite on opposite sides of the head, we can conclude that this is a torsional mode of the oscillator. Additional detection on the wings is necessary to specify the particular torsional mode.

of sample will affect the signal amplitude, the adiabatic conditional statement, and the RF regime used to manipulate the spins. The maximum force for a given field gradient depends on the nuclei under investigation through the magnetization. Curie's law of paramagnetism gives the magnetization of a sample as $M = N \frac{\gamma^2 \hbar^2 (I(I+1))}{3k_B T} H_o$. The gyromagnetic ratio is the most important species-dependent parameter that affects signal strength. Electrons have the largest gyromagnetic ratio, $\gamma = 27.994$ GHz/T, 657.5 times that of a proton. This huge signal advantage is the reason MRFM experiments were first performed with electron spin resonance. To date, NMR-FM experiments have been successfully performed with ^1H , ^{19}F , ^{69}Ga , ^{71}Ga , and ^{75}As [10, 20, 34]. In considering new spins to investigate, one ought to compare the SNR for protons (or other known species) to relative signal strengths and the natural abundance of the isotopes (refer to the NMR tables in the CRC or Varian wall

chart). A large gyromagnetic ratio also helps with signal strength because the adiabatic conditional factor is proportional to its square. This to say that for all other things equal, more spins will be manipulated and contribute to a greater force on the oscillator for large γ nuclei. Be careful not to read this as saying “large γ spins don’t relax”, as this is not true. In fact, relaxation rates are also proportional to γ^2 . This can be a problem for samples with large gyromagnetic ratios if excessive relaxation mechanisms are present. And be careful not to assume that these two effects cancel each other⁸.

⁸Other problems with large gyromagnetic ratios are strictly equipment based. We cannot perform MRFM experiments on electrons in our 8.2 T magnet at this time because we do not have microwave frequency capabilities.

Chapter 2

Experimental Details

*“You’re stupid, you’ve always been stupid,
you’ll always be stupid...See ya’ tomorrow, Tiger!”*

- Al Frasca, my undergraduate advisor

Various elements of our main experimental techniques are described in this chapter. Included are sections about oscillator characterization, blind alignment of the fiber to the oscillator, 2-D and 3-D scanning capabilities, relaxation time measurement electronics, signal artifact, and laser-induced resonant self-excitation of the oscillator. We also emphasize that although you’ve always been stupid, and you’ll always be stupid, you ought to show up tomorrow and see how far your stupidity can get you. . .

2.1 Determining Oscillator Characteristics

The fundamental characteristics of any mechanical oscillator are its resonance frequency, quality factor, and spring constant. In this section we describe the methods we use to experimentally determine each of these quantities.

2.1.1 Determining Resonance Frequencies

There are several ways to determine the resonance frequency of the oscillator. The most convenient method is to observe the vibration amplitude of the oscillator while driving it with a sinusoidal force whose frequency is incremented in small discrete steps. Another way is to digitize the noise from the oscillator and Fourier Transform this signal. LabVIEW programs have been written to perform both of these methods. The FFT is a faster method, but due to current sampling rate limitations, both methods work roughly the same.

2.1.1.1 Frequency Scans

In a conventional frequency scan, a sinusoidal voltage is applied for a time interval ΔT from a Stanford Research Systems DS345 function generator to both a piezo plate (on which the oscillators have been mounted) and the reference channel of the lock-in. The voltage on the PZT 840 piezo plate (American Piezo Ceramics, Inc.) causes the ceramic to expand an amount Δh according to the formula

$$\Delta h = d_{33}V, \quad (2.1)$$

where d_{33} is a piezo-dependent constant equal to 290×10^{-12} m/V. Since the oscillators have been silver epoxied to the piezo, the oscillatory expansion imposes a driving force on the oscillator at the frequency of the voltage. The voltage input to the reference channel tells the lock-in to which frequency it

should listen. The vibration signal from the interferometer is sent to the lock-in, where it is averaged with a time-constant τ_c . The shaking interval ΔT is set to be 3-5 times τ_c to ensure the output of the lock-in is stable for a stable input. The equivalent noise bandwidth of the lock-in is $\Delta\nu = 1/4\tau_c$ when the normal 6 dB/octave filter is used¹. This means that the lock-in is effectively listening to frequencies in the range $(f_o - \Delta\nu, f_o + \Delta\nu)$. Additionally, τ_c tells us the time over which the signal is being averaged by the lock-in. After shaking the oscillator for ΔT , the program stores the output of the X and Y channels of the lock-in, increments the frequency of the DS345, and repeats. The output of the program is a delimited text file that is analyzed using Igor Pro. The resonance frequency and an (under) estimate of the quality factor are obtained using Igor's Lorentzian curve fitting algorithm.

2.1.1.2 Fourier Transforms

Fourier transform programs written in LabVIEW also allow the resonance frequency of the oscillator to be determined. In this scheme, we detect the noise vibrations of the oscillator, not its driven motion. Thus, when using this method, the electrodes of the piezo plate are grounded. In these programs the lock-in samples and stores the X and Y outputs to its buffer at its maximum sampling interval $\Delta t = 1/(512 \text{ Hz})$. This time series is then fourier transformed in LabVIEW using a complex fast fourier transform (FFT) algorithm. If N samples are stored by the lock-in, then the fourier transform will

¹Refer to the manual to determine the bandwidth for other filters.

have a frequency resolution given by

$$\Delta f = \frac{1}{N\Delta t}. \quad (2.2)$$

When using the FFT programs, it is required that the bandwidth of the lock-in ($\Delta\nu$) be at least twice as large as the spectrum that results from the FFT. This is due to the gaussian shape of the lock-in; the roll-off of the filter causes erroneous results because the amplitudes of outlying frequencies are attenuated. With this in mind, the bandwidth of the lock-in must obey

$$\Delta\nu \geq \frac{2}{\Delta t}. \quad (2.3)$$

The input to the complex FFT is the complex number $X + iY$, where X and Y are the X and Y outputs of the lock-in. One advantage to using the lock-in is that the complex FFT then gives a double-sided spectrum; negative frequencies correspond to frequencies below the center frequency and are not simply degenerate positive frequencies (as in the case of a real FFT).

The limitation of the sampling rate of the lock-in means that only 512 Hz can be observed at once. One FFT program was written to scan the center frequency in 512 Hz steps, but with low resolution ($N = 512$), and another was written with $N = 2^n$, where n is programmable, for taking high resolution spectra. After determining the position of the resonance with the scanning FFT program, the high resolution FFT program is then used to monitor the resonance. This has proven to be a valuable time and money²

²The high field magnet used in those studies uses 35 L of liquid helium in about six hours.

saving technique: in a continuation of the field effects on magnetically capped oscillators study of Chapter 4, four times as much data was taken in less than half the time.

2.1.2 Determining Quality Factors

The quality factors of our oscillators can be measured using frequency scans or the ring-down of an excited oscillator. In the former, the shape of the resonance is fit to a Lorentzian using the Lorentzian curve fitting algorithm in Igor Pro. In the latter, the oscillator's amplitude is monitored as a force driving it is turned off; the time constant of the exponential decay is directly proportional to Q .

2.1.2.1 Frequency Scans

Frequency scans are obtained in the way described above in Section 2.1.1.1. Fitting the resonance to a Lorentzian gives a decent estimate of Q if appropriate measures are taken. In general, it is most efficient to make sure that the frequency increments are equal to the bandwidth of the measurement. Note that for high Q resonances, where the full width at half maximum (FWHM) may be less than one hertz, large time constants are necessary. If the time constant is chosen to be too short, there will be artificial broadening of the resonance due to the convolution of the impulse response function of the instrument with the actual signal. This is to say that since the noise bandwidth of the lock-in is a gaussian with width $\Delta\nu$, a frequency scan with

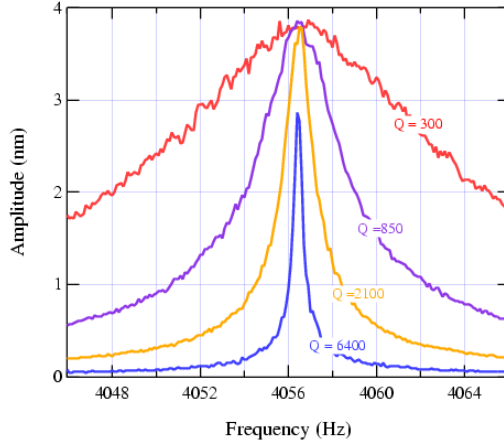


Figure 2.1: Frequency scans of an oscillator resonance showing the effect of using different time constants. Quality factors of the resonance are indicated on each curve. From broadest to sharpest, the Q values correspond to time constants of 30 ms, 100 ms, 300 ms, and 1000 ms. The amplitude of the $\tau_c = 1000$ ms curve is shorter than the rest because the bandwidth was smaller than the step size and the peak was thus skipped over; a shorter step size would have revealed the peak amplitude equal to the others.

infinitely small steps would broaden a delta-function resonance so that the signal observed would be a gaussian of width $\Delta\nu$. In order to determine the true shape of the resonance, and therefore its intrinsic Q , a deconvolution of the signal with the lock-in's impulse response function would have to be performed. Note that the “intrinsic” value is a function of temperature and pressure; all of our quality factors are pressure limited because our best pressures are only ~ 0.1 mTorr. Figure 2.1 shows the effect of using too small of a time constant.

2.1.2.2 Ring-Down

The quality factor can also be determined from the decay of the oscillator's amplitude if a driving force is removed. To this end, a sinusoidal voltage is sent to the piezo plate at the resonance frequency of the oscillator and is then suddenly turned off. This event triggers a Nicolet Digital Oscilloscope (with a significant pre-trigger) to digitize the R output of the lock-in. The de-excitation of the oscillator is fit to an exponential to find the $1/e$ time constant τ of the decay. Q is then calculated according to

$$Q = \pi\tau f_{osc}. \quad (2.4)$$

A significant study of quality factors of oscillators appropriate for NMR-FM was published by Rugar's group in March, 2000 [35]. Most other MRFM groups determine the quality factors of their oscillators using this ring-down technique.

The ring-down method is more appealing from an experimental point of view because it is quick and reliable. However, in an erroneous effect opposite of that of the scanning method, the Q of the oscillator can be artificially enhanced by the lock-in if its time constant is too large. In order to reasonably estimate the Q from the ring-down, the time constant should be quite short. To make sure the time constant is short enough, the ring down is observed for several time constants. As shown in Fig. 2.2, the calculated Q will plateau when it becomes independent of the time constant; this is the intrinsic Q of the oscillator.

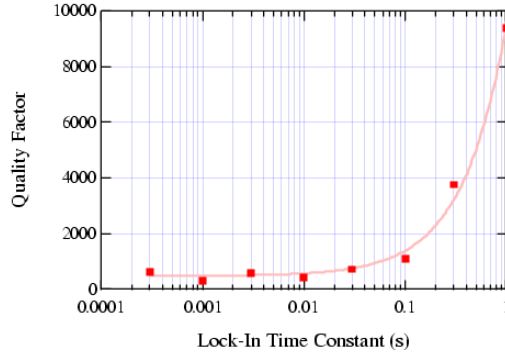


Figure 2.2: When using the ring-down method, the calculated mechanical quality factor plateaus at the oscillator’s intrinsic Q for a given temperature and pressure. The line is a guide to the eye.

2.1.3 Determining Spring Constants

Perhaps the most elusive oscillator characteristic to date has been the spring constant, k_{osc} . Direct measurement of the spring constant is not possible at this time³. Instead, we go through a grand scheme utilizing the Equipartition Theorem

$$\frac{1}{2}k_{osc}\langle x^2 \rangle = \frac{1}{2}k_B T, \quad (2.5)$$

where we measure $\langle x^2 \rangle$, the mean square noise vibration amplitude of the oscillator, at a known temperature then calculate k_{osc} .

Determining $\langle x^2 \rangle$ is not straightforward. It is not simply the maximum

³One may be able to apply a force and detect the deflection of the oscillator using an AFM, but this is probably infinitely more trouble than its worth [36].

noise vibration amplitude squared⁴ Its definition is

$$\langle x^2 \rangle = \int_0^\infty |G(f)|^2 S_F df. \quad (2.6)$$

The integrand is sometimes called the noise power spectrum. $|G(f)|^2$ is the absolute square of the mechanical transfer function, and is (usually) written as

$$|G(f)|^2 = \frac{f_{osc}^4/k_{osc}^2}{(f_{osc}^2 - f^2)^2 + (f_{osc}f/Q)^2}. \quad (2.7)$$

S_F is the noise spectral density, which is given by

$$S_f = \frac{4k_{osc}k_B T}{2\pi f Q}. \quad (2.8)$$

The lock-in itself measures the RMS noise vibrations $\sqrt{|G(f)|^2 S_F}$ with a bandwidth $\Delta\nu$. Choosing the bandwidth to be very small allows us to reconstruct the shape of $\sqrt{|G(f)|^2 S_F}$ by determining the RMS value for discrete frequencies in the spectrum. This cannot simply be done using a standard frequency scan with a long time constant because the amplitude R that is sampled will sometimes be zero (it is noise after all). In order to determine the RMS noise amplitude for a given frequency, a time series must be taken by digitizing the outputs of the lock-in; the RMS value of this time series will be a point plotted on the RMS noise amplitude spectrum. The

⁴We have had several discussions with Sean Garner from Marohn's Cornell group about this. Their method is to determine the RMS value of the R output of the lock-in with a bandwidth that envelopes the resonance ($\Delta\nu \sim 3 \times FWHM$). We have not been able to show that their method is equivalent to ours, though they and John Sidles believe they yield the same spring constants. The discrepancies may be due to bandwidth conventions.

resulting line shape will resemble a driven oscillator scan, and can be fit to a Lorentzian to determine Q .

The power spectrum (the integrand of Eq. 2.6) is obtained by squaring the RMS noise amplitude spectrum, then dividing the result by the bandwidth used in determining each RMS amplitude. The resulting curve is much narrower than the RMS amplitude. As a result, there may not be very many data points near the peak of the power spectrum for large Q oscillators. The shape of the power spectrum is, however, still a Lorentzian, and can thus be readily fit using Igor. The resulting curve fit is integrated over frequency to give us our value for $\langle x^2 \rangle$.

An example is in order. The significant benchmarks for using the above process are illustrated in Fig. 2.3. The oscillator investigated was a simple $30 \mu\text{m} \times 30 \mu\text{m}$ paddle with a $180 \mu\text{m} \times 3 \mu\text{m}$ neck that was $\sim 300 \text{ nm}$ thick. To determine the value of each point on $\sqrt{|G(f)|^2 S_F}$, the R output of the lock-in ($\tau_c = 3 \text{ s}$) was digitized using the Nicolet for 10 s with a sampling interval of 20 ms at room temperature. This waveform was converted to a vibration amplitude by multiplying it first by the scale factor of the lock-in (giving it units of real Volts), then by the Volts-meters conversion factor $\lambda/2\pi V_{pp}$, where λ was the wavelength of the laser (660 nm), and V_{pp} was the peak-to-peak fringe size (4.0 V). The RMS value of the resulting time series (i.e., the actual point plotted in the top figure of Fig. 2.3) was calculated using the wavestats function in Igor. The lock-in reference frequency was incremented by 0.1 Hz between time series. After $\sqrt{|G(f)|^2 S_F}$ was con-

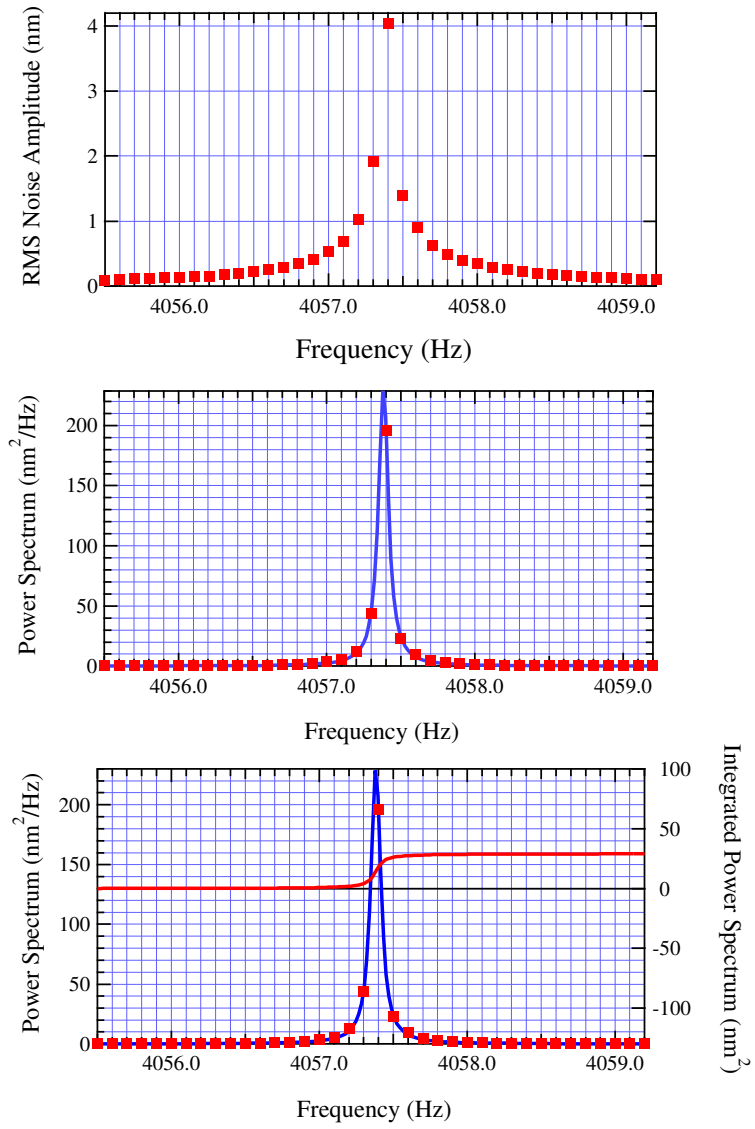


Figure 2.3: Example of $|G(f)|^2 S_F$ and its integral used in determining the spring constant of an oscillator.

structed, it was squared, then divided by $\Delta\nu = 1/(4 \times 3 \text{ s})$, and then fit to a Lorentzian (center graph of Fig. 2.3). The curve fit was then numerically integrated to determine $\langle x^2 \rangle$. The last graph in Fig. 2.3 shows the power spectrum and its integral. Note that that using the curve fit as the integrand will yield a larger value for $\langle x^2 \rangle$ than a trapezoidal integration of the actual data points. Integrating the curve fit will thus yield a larger spring constant, which is best for conservative estimates of F_{min} . Plugging $\langle x^2 \rangle$ for this oscillator into Eq. 2.5 determines $k_{osc} = 2.0 \times 10^{-4} \text{ N/m}$. This is in good agreement with the estimate $k_{osc} = 4.2 \times 10^{-4} \text{ N/m}$ from its geometry [37].

2.1.4 Fringe Locking Circuit

An important element used in determining the oscillator characteristics is the fringe locking circuit. This feedback circuit allows us to maintain a constant DC level on the interference pattern while we characterize the oscillator. As indicated in the introduction, we want to fix our DC level at the middle of the interference pattern where the absolute value of the slope is maximum. The slope at this point is given by

$$\left| \frac{dV}{dz} \right|_{max} = \frac{2}{\pi} \times \frac{\lambda}{4}, \quad (2.9)$$

where λ is the wavelength of the laser. It is important that this slope not change during the experiment because this is the conversion factor we use to translate the voltage from the lock-in to a deflection amplitude. Experimentally, one determines the conversion factor by measuring the peak-to-peak deviation of the fringes (V_{pp}) as the fiber is moved using the P- output of the

locking circuit⁵, and plugging into the formula

$$\beta = \frac{\lambda}{2\pi V_{pp}}. \quad (2.10)$$

Taking into account the sensitivity of the lock-in S , the final translation from the lock-in signal V_{LIA} to amplitude A is given by

$$\frac{A}{[nm]} = \frac{\beta}{[nm/V]} \frac{V_{LIA} \times S}{[V]}. \quad (2.11)$$

The feedback circuit currently used is depicted in Fig. 2.4. The design is functionally the same as past circuits used for NMR-FM. The differences are the addition of isolating buffers between stages, and more importantly the switch that optionally accesses the last inverting amplifier and thus allows for locking on either slope of the fringe.

2.2 Blind-Aligning of Fiber to Oscillator

It is often the case that when the can is placed on the probe, the alignment of the laser to the oscillator is lost. This is due to impulses that slightly displace one of the many moving parts of the probe. Loss of alignment can simply mean that there was some lateral motion in the $\hat{x} - \hat{y}$ plane, or it can mean catastrophic decapitation of the oscillator by the fiber as it slides forward in the \hat{z} direction. It is important to be able to blindly recover the alignment so that the vacuum doesn't have to be broken each time the fringes

⁵It is sometimes desirable to use an external DC voltage supply instead of the P- output in order to move through several fringes; it may be advantageous to develop a high-voltage fringe locking circuit.

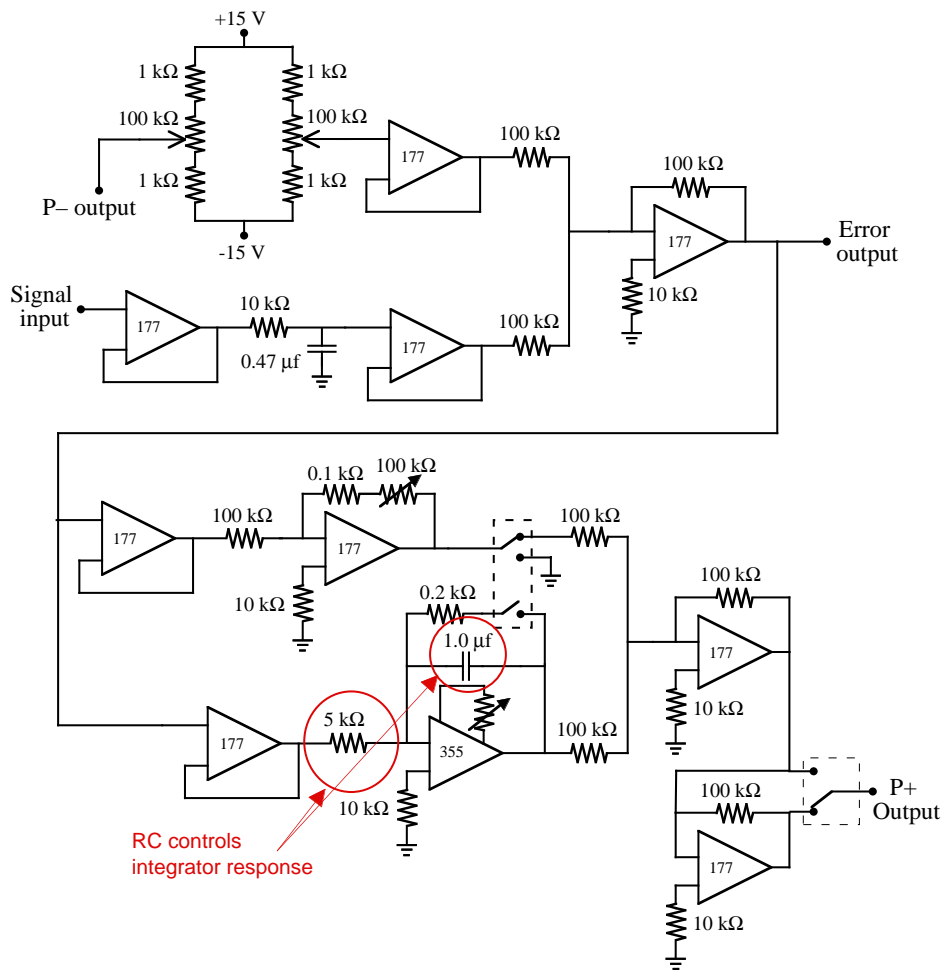


Figure 2.4: Fringe lock circuit used to maintain a constant position and slope on the interference pattern during experiments.

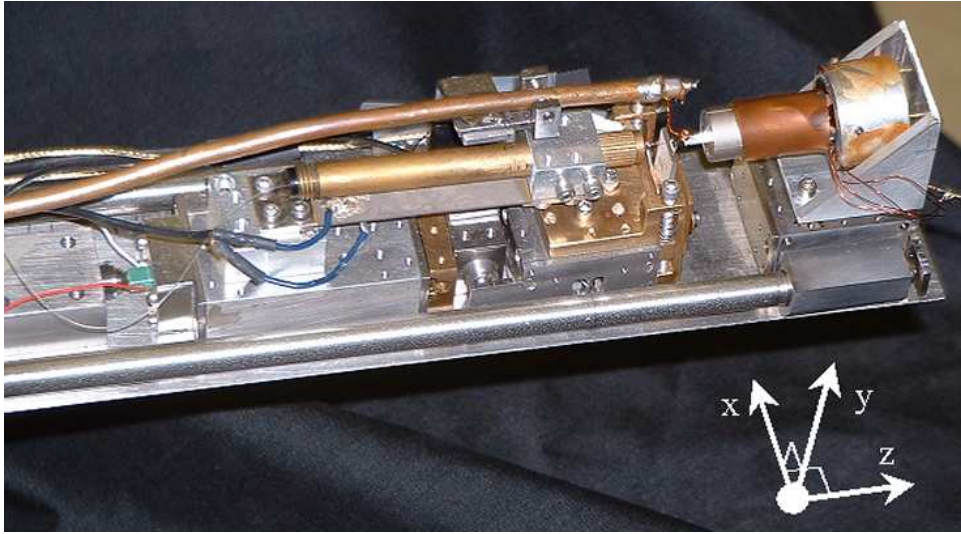


Figure 2.5: Coordinate system for the probe.

are lost. This section sets forth a fairly reliable realignment procedure, and details the positioning capabilities of the current probe.

First, we define our coordinate system with $+\hat{z}$ along the fiber toward the oscillator, $+\hat{x}$ right-to-left on the oscillator (looking toward $+\hat{z}$), and $+\hat{y}$ from the base to the head of the oscillator, as depicted in Fig. 2.5. As the probe is currently configured, rotating the \hat{x} positioning knob clockwise advances the oscillator stage in the $+\hat{x}$, applying a positive voltage to the piezo bimorph raises the fiber in the $+\hat{y}$, and rotating the \hat{z} knob counter clockwise advances the fiber stage in the $+\hat{z}$ direction.

The externally-controllable stages that position the oscillator, fiber, and sample have been characterized using the interferometer to measure their motion. One full counterclockwise turn of their respective positioning knobs

moves the oscillators in the $+\hat{x}$ direction by $160\ \mu\text{m}$, the fiber in the $-\hat{z}$ direction by $90\ \mu\text{m}$, and advances the sample in the $+\hat{z}$ direction by $81\ \mu\text{m}$. Additionally, the piezo bimorph shifts in the $\pm\hat{y}$ direction by roughly $\pm 2\ \mu\text{m}/\text{V}$. The backlash in the oscillator stage is roughly $3/14$ of a turn in both directions. Backlash in the other stages was too difficult to measure because the vibrations caused by reversing the direction of the knob disturbed the interference pattern.

Before putting the can on, it is important to know and record the DC level of the fiber when it is pointing at nothing (light reflected is only from impedance mismatch of glass and air), and the maximum DC level of the interference pattern when it is perfectly aligned to the oscillator. These two levels will serve as benchmarks for what is happening during the alignment. For instance, if the DC level falls below the former (with no fringes), the fiber is most likely damaged from some sort of impact. Likewise, if the maximum DC level rises above what you've defined as perfect, then the fiber is too close to, or perhaps even touching the oscillator.

The DC level and fringe size are our eyes for the blind align. Before putting the can on and after the perfect alignment has been obtained, the fiber should be retracted a few turns (record the actual number), and displaced in the \hat{x} direction so it points between oscillators. This is a precautionary step that will save oscillators from being speared by the fiber from shocks to the probe. Once a good vacuum has been established, replace the fiber to its starting position taking into account the backlash of the gear systems (see

below).

It has been found easiest to align by moving in the \hat{x} direction manually, while continuously scanning in the \hat{y} direction. The scanning is performed with a 0.25 Hz, $10 V_{op}$ sine wave from a signal generator. This amplitude scans roughly half of the oscillator height ($\sim 50 \mu\text{m}$). This scanning motion allows quick determination of whether or not the fiber is pointed something: if the voltage level is oscillating more than when the fiber is pointed at nothing ($\pm 3\%$), then you are pointed at something (hopefully the oscillator, but perhaps the substrate). Beginning from the safe position (fiber retracted, oscillators displaced), turning the \hat{x} knob in quarter turns will advance the oscillator stage in small enough steps that the DC level should increase when the oscillator passes in front of the fiber⁶. If no increase in the DC level is observed within a reasonable region, advance the fiber one half turn, and reverse the direction of the oscillator stage. This is repeated until the DC level notably increases. If you can repeatedly scan past the same few positions and observe the DC level first increase and then decrease a few turns later, then you are most likely pointed at the oscillator. If you believe you are pointed at the oscillator, advance the fiber to (nearly) recover the DC level and fringe size that you initially recorded for your perfect position. This whole process only took one paragraph to write, but could take an hour or so to perform in practice, so, as always, be patient.

⁶If the oscillator-fiber distance is fairly large, then you will not see appreciable fringes from this safe position.

Where are you pointed? Once you have found the oscillator, it is important to determine where the fiber is actually pointing. This will give us the capability of knowing which modes of the oscillator we should expect. Additionally, knowing where the fiber points will help the data analysis as important corrections are necessary to determine the actual force imposed on the oscillator because the amplitude of oscillation is position dependent⁷.

During the hunt for fringes, the left and right sides of the oscillator are determined. In order to determine the \hat{y} position, we need to use the bimorph and observe the DC level as it scans. Since the angle of deflection relative to the oscillator is small, decent sized fringes ($> 1 V_{pp}$) are attainable at all times during scanning when there is good alignment to the oscillator. Once fringes are recovered, if it is found that the DC level drops drastically during the \hat{y} scan cycle, then the fiber is near the top or bottom of the oscillator—when this case is observed, distinguish between top and bottom of the oscillator by manually applying a DC voltage of known polarity. If, however, the fiber is pointed right in the middle of the oscillator, a change in the DC level may not be observed because the scanned range is too small. In this case, you will have to scan manually with a ± 50 V voltage supply in order to cover the whole oscillator. When switching to this higher voltage, you should move slightly off the oscillator in the \hat{x} direction and record the negative voltage level that then increases the DC level—this is the silicon ledge that has been undercut

⁷For example, in the lower cantilever mode, if you are pointed at $L/2$, the amplitude is, to first order, half what is expected if you are pointed at the end of the cantilever.

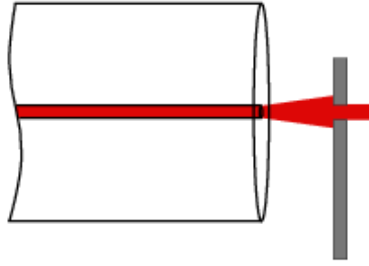


Figure 2.6: A dip in the peak-to-peak amplitude of the interference pattern while moving the fiber in the \hat{y} direction is due to light escaping through the head-wing gap.

during the etch. Voltages more negative than this should be avoided to save the integrity of the fiber.

Distinguishing the head of the oscillator from its wing is an interesting process. It is quite clear whether you are initially pointed at the top of the head or the bottom of the wing because of the dramatic difference in the DC level when you are pointed somewhere on the oscillator compared to nothing. However, when you want to transition from the wing to the head, you will always have fringes because the laser beam diverges enough that some light is always striking the oscillator, as depicted in Fig. 2.6. It is thus important to closely monitor the fringe size at each position along the oscillator (i.e., at each voltage applied to the bimorph). As illustrated in Fig.2.7, when starting from the wing, if a positive voltage is applied, the fringe size remains constant, then dips, then recovers to its initial value. The dip is the location of the head-wing gap, and can extend over only a few volts, depending on how far the fiber resides from the oscillator.

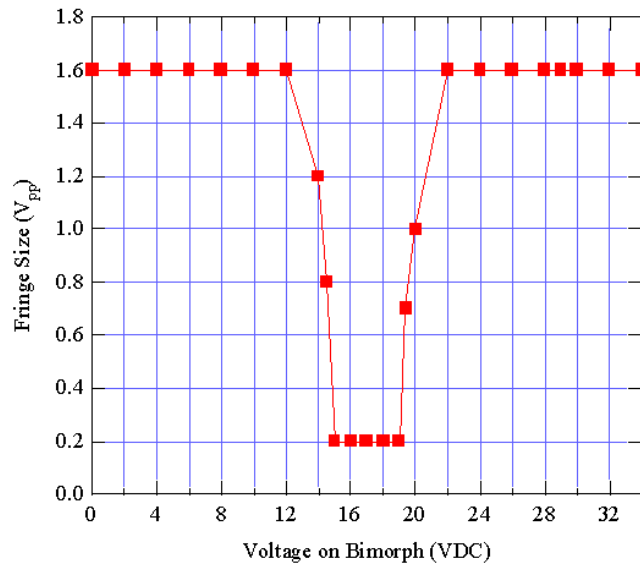


Figure 2.7: Head-wing gap seen by a severe dip in the peak-to-peak amplitude of the interference fringes.

2.3 Tube Piezo for 2-D and 3-D Scanning

A quartered-tube piezo has been installed in the microscope for two and three dimensional scanning experiments. The EBL #2 tube (Staveley Sensors) has a length of 1.25", an OD of 0.125", and a wall thickness of 0.014". The electrodes were chosen to be gold instead of the standard nickel to eliminate any unwanted magnetic effects when the probe is inserted into the NMR magnet. The urethane coating on both ends of each lead was removed by first burning it with a lighter, then removing the residue with a scouring pad to reveal the copper wire. After trimming the leads so that only 1 cm of copper was exposed, two short (~ 3 mm) pieces of shrink wrap separated by ~ 1 cm were used to hold the leads firmly against their respective electrodes leaving

the bare wire exposed. The leads were then silver epoxied in place to establish electrical contact with the electrodes using a free sample of mix-free silver epoxy from Lakeshore Cryogenics. The shrink wrap was left on in order to protect the epoxy joints from unnecessary stressing due to moving the leads. The leads connect to thin diameter RG174 coax that connects to the vacuum compatible BNC electrical feedthrough⁸ at the top of the probe.

2.3.1 Piezo Stage Design

The stage for the tube piezo has been assembled so that motion is possible along all three of the probe's axes. This has proven invaluable for aligning samples to the oscillators. A coarse, externally controllable, \hat{z} -positioning stage (see [38]) is mounted directly on the base plate of the probe. A smaller stage (see [39]) is screwed onto the \hat{z} -stage and gives \hat{x} -positioning capabilities. The \hat{y} -stage is permanently fixed in the moving part of the \hat{x} -stage. The axis of the tube piezo is aligned with the \hat{z} direction if it is mounted perpendicular to the \hat{y} -stage.

The tube has been epoxied to a triangular macor spacer in order to keep it isolated from the rest of the probe. The spacer has a slice in it (almost giving it a V-shape) through which the lead to the inner electrode (ground) of the piezo tube passes; this allows the piezo to sit perpendicular to its base, and also frees-up the other end of the tube for a sample holder. This assembly

⁸See the Appendix for a reliable method for making vacuum compatible BNC electrical feedthroughs.

was then epoxied to a brass base with Torr Seal. The brass base is separated from the \hat{y} -stage by a $1/16''$ diameter steel ball bearing. Three screws on the circumference of a $0.25''$ circle that are 60° degrees apart pass through the \hat{y} -stage and screw into the brass plate in order to firmly pull the base, ball bearing (centered in the screws' circle), and \hat{y} -stage together. The tube can be tilted within a solid angle of about 20° by the relative tightening of these three screws because the base pivots on the ball bearing.

The sample is held at the free end of the tube. An aluminum cylinder was machined to fit tightly, yet freely, into the tube. A flattened strip ($1\text{ mm} \times 2\text{ mm}$) of aluminum foil serves as a shim to hold the insert in place, and to ensure an electrical connection to the grounded inner electrode. The foil was also used as a precautionary measure to protect the tube from cracking if the insert fit too tightly. The insert contains a 0.5 mm through hole with a deformed mouth on the face that is inside of the tube. The deformation anchors and grounds a graphite rod (0.5 mm pencil lead) that serves as a sample holder.

2.3.2 Scanning Tube Electronics

This is the first generation of scanning for our NMR-FM general purpose probe. As such, the electronics are manually controlled voltage dividers. Each quarter of the tube piezo has its own high voltage op-amp. A schematic of these simple identical circuits is presented in Fig. 2.8. In the future, one might imagine the tube piezo being controlled with sophisticated software like

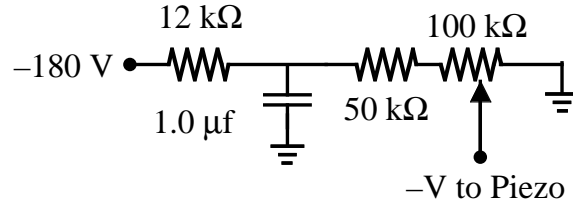


Figure 2.8: Voltage divider used to apply variable voltage to the tube piezo quadrants. This setup extends the piezo, while using a positive voltage source retracts the piezo.

those found in AFM and STM systems.

2.3.3 \hat{z} Piezo Characterization

At this point, the tube piezo is only used for 1-D scanning in the \hat{z} direction. The tube piezo polarity is such that the quartered electrodes should be positively biased relative to the inner electrode⁹. Applying a negative voltage makes the piezo contract. In order to accurately characterize its contraction, the interference pattern was monitored as a voltage was applied to all four quadrants of the piezo. The laser was pointed at the tip of the graphite sample holder sticking out of the end of the piezo. The voltage was applied by rotating the 10-turn potentiometer of a voltage divider. The shift of the interference pattern and the applied voltage were recorded with the Nicolet digital oscilloscope as a function of time. The pattern was then plotted as a function of the applied voltage, as shown in Fig. 2.9. Because the contraction of the

⁹Applying the opposite polarity is not bad if the voltage is kept below the tube's depolarization voltage.

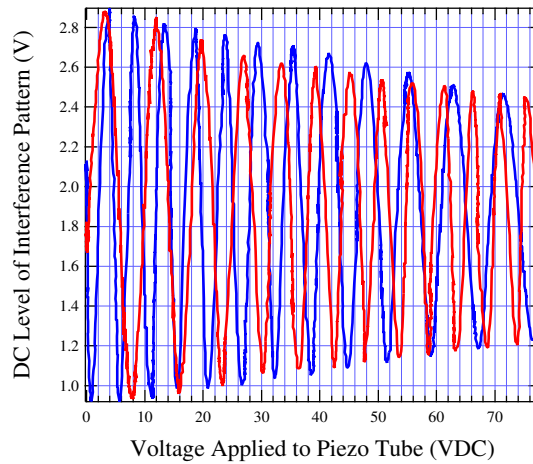


Figure 2.9: Interference pattern as a function of voltage applied to the four quadrants of the tube piezo. The non-linear contraction of the piezo is realized by the inequivalent voltage changes required to reach successive extrema of the pattern. The decrease of the peak-to-peak amplitude with applied voltage is caused by a decrease in intercepted light reflected from the target as the fiber-target distance is increased (the beam diverges).

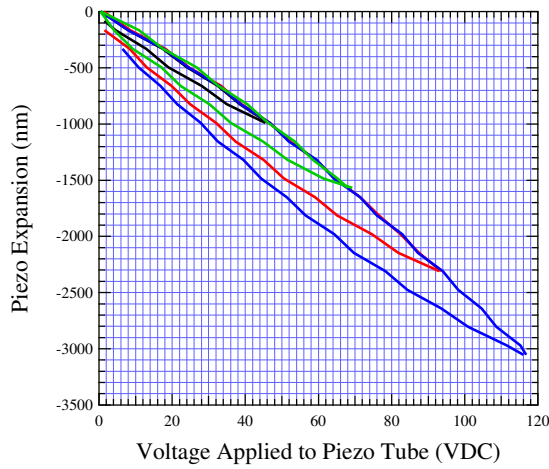


Figure 2.10: Contraction of the tube piezo as a function of applied voltage. The major loop was performed first, followed in succession by the smaller loops. All five electrodes of the piezo were grounded upon returning to zero applied voltage.

piezo is nonlinear, it is easiest to convert from the digitized interference pattern to a measure of contraction by knowing that the points that correspond to the peaks in the pattern are separated by $\lambda/4$. The contraction of the tube piezo can then be plotted as a function of applied voltage as in Fig. 2.10.

It is important to note that the piezo electrodes must be grounded upon returning to zero applied voltage. This allows any accumulated charge to be liberated. If the electrodes are not grounded, the excess charge does not allow the piezo to reproducibly expand. This unwanted effect is illustrated in Fig. 2.11.

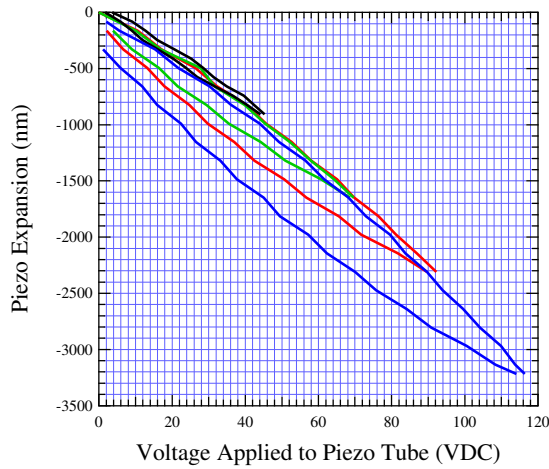


Figure 2.11: Contraction of the tube piezo as a function of applied voltage. The major loop was performed first, followed in succession by the smaller loops. The electrodes were not grounded between loops, causing the sag in contraction.

2.4 Relaxation Time Measurement Electronics

Very versatile electronics were built to measure relaxation times with cyclic adiabatic inversion (CAI). With these electronics, we now have the ability to measure the spin-lattice relaxation time T_1 , the spin-spin relaxation time T_2 , the rotating-frame spin-lattice relaxation time $T_{1\rho}$, and the relaxation time during cyclic adiabatic inversion T_{CAI} . These electronics have been integrated with the digital pulse programmer of the NMR spectrometer to allow the application of 10 ns rise-time pulses that are accurate in duration to 100 ns. This section is devoted to describing the functionality of these electronics. The circuit itself is presented in Fig. 2.12.

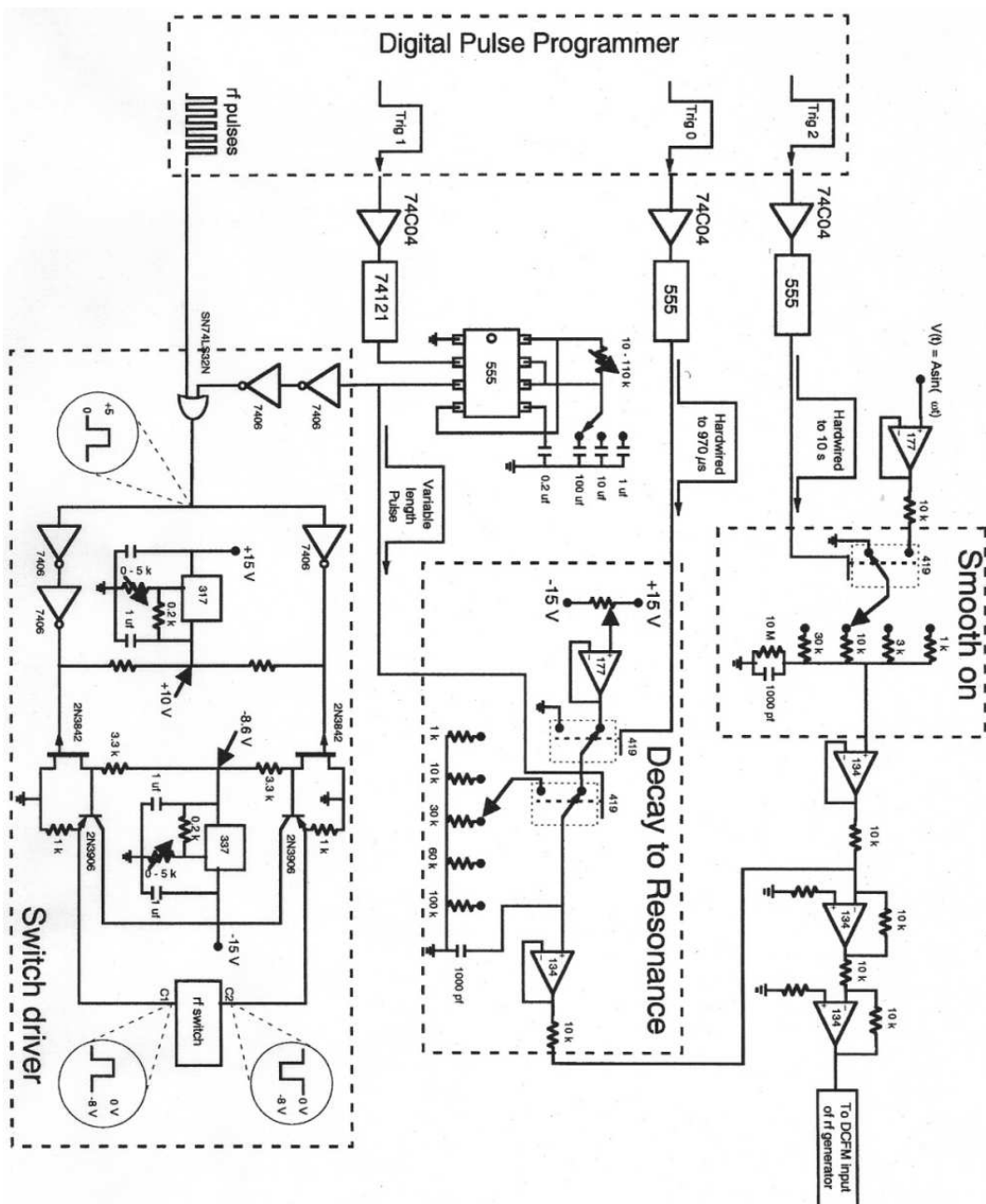


Figure 2.12: Relaxation time measurement electronics circuitry.

2.4.1 Circuit Analysis

There are three major portions of the electronics whose relative triggering times give the electronics their broad measurement capabilities. These sections shall be referred to by their functionality, namely “Decay-to-Resonance”, “Smooth-On”, and the “Switch Driver”. The output of Decay-to-Resonance and Smooth-On are added and sent to the DCFM input of an HP6546B RF signal generator. The DCFM function shifts the carrier frequency by an amount proportional to the input voltage. The Switch Drivers open and close an RF switch for pulsing and cyclic adiabatic inversion.

The Decay-to-Resonance portion of the circuit is triggered twice during an experiment, once by Trigger Zero, then at a later time by Trigger 1. Decay-to-Resonance is ultimately responsible for setting the output of the RF generator to the resonance frequency of the spins ($\gamma(H_o + H_{perm})$) when pulse sequences are used (Trigger Zero), and sets the DC offset to zero during the CAdI sequence (Trigger One).

Trigger Zero comes from the “B output” of Channel B of the pulse programmer¹⁰. It initiates a long (currently hard-wired to 60 ms) high pulse output from a 555 timer¹¹ that is sent to the gate of a DG419 solid state SPDT switch. The high gate voltage connects the output (Pin 8) from Pin 1 (normally closed) to Pin 2 (normally open), which grounds the output in

¹⁰Channel B can only output 10^n pulses, so is used as a delay/initial trigger channel instead of being used to send out arbitrary pulses.

¹¹Currently has a debouncer and 74121 before the 555, which allows the electronics the capability to be triggered manually with a mechanical switch.

about 30 ns. The output of the DG419 switch is connected to the input of a OP134 buffer through Pin 1 of a second DG419. The buffered signal is added to the Smooth-On output (which is ground at this time), then sent to the signal generator. The quick change in voltage from the DC offset to ground causes the HP to quickly change its output from far off resonance to exactly on resonance. The gate stays high for the duration of any necessary pulses if, for instance, one is using a saturation comb. When the gate voltage goes low again, the HP again outputs RF far off resonance.

Trigger One triggers the decay to resonance that is essential to cyclic adiabatic inversion. Trigger One comes from the “Trig Out” output of the pulse programmer’s Channel A some time after the DC offset rebounds from ground. For the decay to resonance, Trigger One initiates a variable length pulse output from a 555 that is simultaneously sent to the gate of the second DG419 switch and into the Switch Drivers. With the gate on the DG419 high, Pin 2 is connected through a selectable resistance to ground. This then allows the capacitor to discharge with a time constant variable between 1 μ s and 10 s. The voltage decay is buffered and then added to the output of the Smooth-On portion of the circuit before being sent to the DCFM input of the HP signal generator. This (relatively) slow decay is responsible for tilting the effective field from the \hat{z} direction into the \hat{x}' direction.

The Smooth-On portion of the circuit is responsible for the initiation of the cyclic adiabatic inversion sequence that allows us to measure the magnetization. A sine wave whose frequency equals that of the mechanical oscillator

is buffered with a OP177. The output of this buffer connects to Pin 2 (NO) of another DG419 switch. The switch prevents the sine wave from being mixed with the outputs of Decay-to-Resonance, and has Pin 1 normally shorting the input of the buffer to ground. Trigger Two initiates a high pulse (currently hard-wired to ~ 3.5 s) from a 555 timer that connects the switch output to the sine wave at Pin 1. Trigger Two is currently the “B Start” output of channel A. The high voltage on the gate directs the AC into an awaiting RC circuit with a selectable time constant ranging from $1 \mu\text{s}$ to $30 \mu\text{s}$ ¹². The effect of the RC circuit is to slowly increase the amplitude of the AC as it is added to the output of Decay-to-Resonance. As shown in Fig. 2.13, this results in a smooth, yet quick, turn-on of CAdI and eliminates a sudden change of the frequency output to the sample. We want the turn-on to be smooth to eliminate any sudden changes in the effective field that could result in a detrimental loss of locked spins.

At this point, the outputs of Decay-to-Resonance and Smooth-On are added together at the input of a unity gain OP134 inverting amplifier, inverted again through another OP134, then sent directly to the DCFM input of the HP signal generator. Figures 2.14 and 2.15 show the actual output of the signal generator due to the signals generated by these electronics being sent to the DCFM input of the generator.

The Switch Driver part of the circuit controls the RF switches that al-

¹²A $10 \text{ M}\Omega$ resistor was inserted permanently in parallel with the capacitor to alleviate a mysterious downward trend of the output that we attribute to charging of the capacitor.

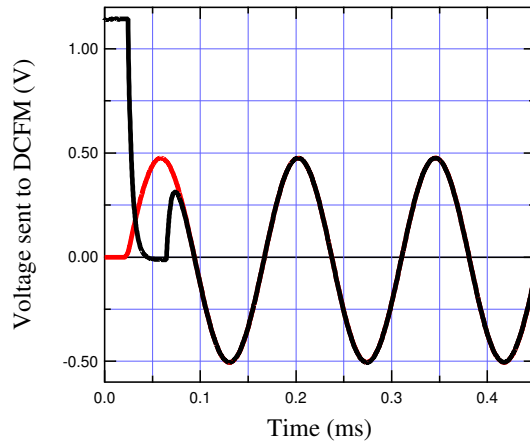


Figure 2.13: Experimental demonstration of the Smooth-On functionality of the circuit. The extension of the sine wave (red) shows that there would have been a sudden change in the RF frequency when the CAdI cycle was initiated if this part of the circuit did not exist. Such a discontinuity would be a diabatic process that could result in a loss of locked spins and therefore force signal.

low RF energy to be transmitted to the coil. The first element of this portion is an OR gate whose inputs are TTL signals from the pulse programmer itself and the 555 output initiated by Trigger One. The TTL from the pulse programmer’s “A Output” opens the switch for pulse sequences. The signal from Trigger One opens switch for the CAdI sequence. The switch driver was duplicated from Jonathan Cobb’s dissertation; a description of its functionality can be found therein [40].

2.4.2 Making Relaxation Time Measurements

Making relaxation time measurements is straightforward with these electronics. This section outlines the steps need to make measurements of the

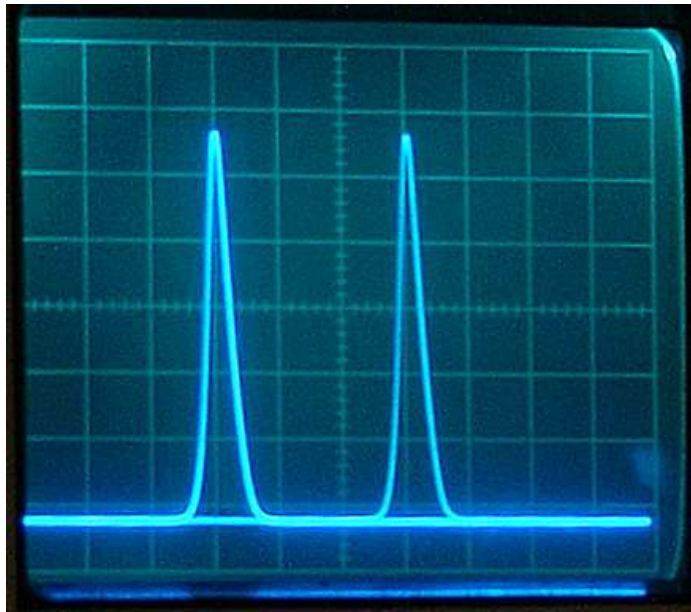


Figure 2.14: Decay from above toward resonance as seen on a spectrum analyzer. The right peak corresponds to a frequency far above resonance, and the left peak is on resonance. The horizontal grid-lines are separated by 100 KHz. The width of the peak has been broadened by the spectrum analyzer.

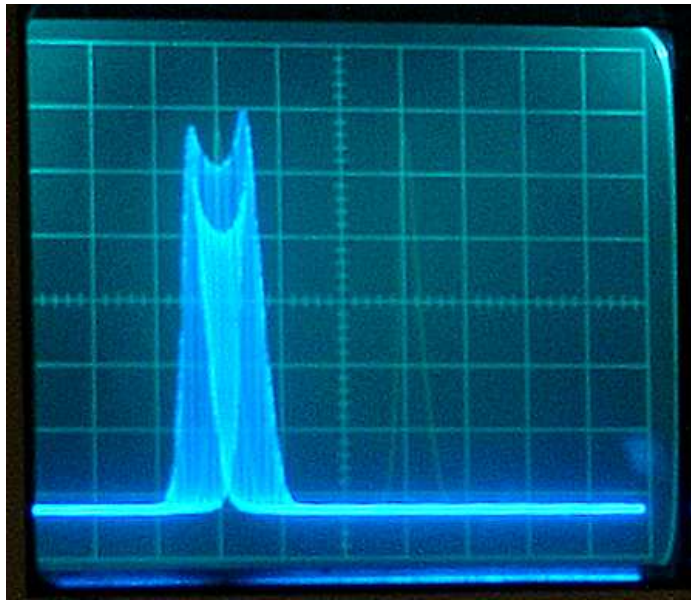


Figure 2.15: FM portion of cyclic adiabatic inversion as seen on a spectrum analyzer. In this example, the FM amplitude $\Omega = \sim 50$ kHz. The horizontal grid-lines are separated by 100 kHz. The ghost of the off-resonance initial frequency can still be seen on the right side of the scope.

T_1 , T_2 , $T_{1\rho}$, and T_{CAdI} . With appropriate preparation, the measurement of the relaxation times can be semi-automated¹³ using the digital pulse programmer.

Spin-lattice relaxation time measurements utilize all aspects of our electronics. First, the magnetization of the sample must be destroyed by a saturation comb. Our typical comb uses six $\pi/2$ pulses separated in time by 5π . The lengths and interval between the comb's pulses are controlled with the digital pulse programmer. After the saturation comb, the magnetization is allowed to grow toward equilibrium for a time τ , after which we sample the magnetization with a cyclic adiabatic inversion (CAI) sequence. This is done for several values of τ , and the resulting magnetization as a function of τ is fit to an exponential $e^{-\tau/T_1}$ to determine T_1 . Figure 2.16 shows the frequency-controlling output of the electronics during a T_1 measurement sequence.

Spin-spin relaxation time measurements are more intricate than those of T_1 , and are by far the most tedious measurements to make. Additionally, one extra channel of the pulse programmer needs to be used in order to send both π and $\pi/2$ pulses. The first pulse sent to the coil is a $\pi/2$ pulse that sends the spins into the transverse plane. The spins immediately begin to dephase in the transverse plane relative to each other due to the different local fields and dipole-dipole interactions they encounter in the sample. After a time τ of dephasing, a π pulse is applied. This pulse reorients the spins so that they now have a relative rephasing. At a later time τ the spins should maximally

¹³Full automation will probably not be feasible for a long time because of the necessity for scanning the relative position of the oscillator and sample.

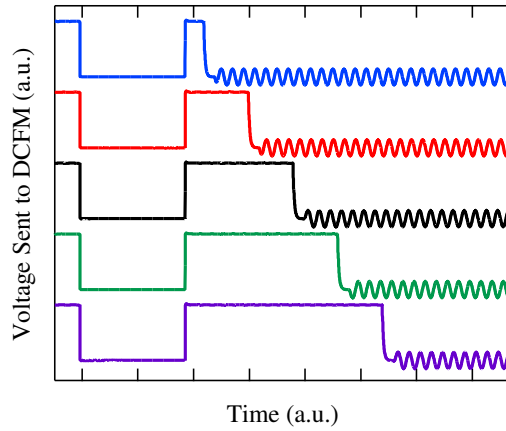


Figure 2.16: Spin-lattice relaxation time T_1 measurement sequence. Each curve is a digitized signal from the output of the electronics. The traces have been offset vertically for clarity.

rephase and should be pointing back along the \hat{y}' direction. In conventional NMR we would simply listen for the rephasing as a spin echo. But in NMR-FM, we don't have that luxury, and in order to actually see an entire spin echo, we need to sample the magnetization in a range of time from $\tau - \delta t$ to $\tau + \delta t$ with separate CAdI sequences¹⁴. This process is repeated for several τ , and the peaks of the spin echoes are fit to an exponential function $e^{-2\tau/T_2}$ to determine T_2 . Figure 2.17 shows the output of the electronics during a T_2 measurement sequence.

The spin-lattice relaxation time in the rotating frame is experimentally as straightforward to measure as T_1 with the electronics. This measurement

¹⁴ δt is an empirical number that needs to be determined for each τ .

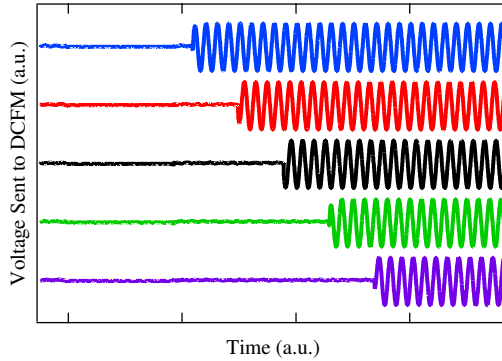


Figure 2.17: Spin-spin relaxation time T_2 measurement sequence. Each curve is a digitized signal from the output of the electronics. The traces have been offset vertically for clarity.

needs no pulse sequences or preparation of the magnetization of the sample. We simply decay the magnetization adiabatically into the \hat{x}' direction where it lies along \mathbf{H}_1 . Because the equilibrium value of the magnetization due to H_1 is some four orders of magnitude smaller than that along \mathbf{H}_0 , the magnetization will decay once tilted along \hat{x}' . By varying the time between Trigger One and Trigger Two, τ , we allow the magnetization to decay before it is sampled with the CAI sequence. The resulting magnetization versus τ curve is fit to the exponential $e^{-\tau/T_{1\rho}}$ to determine $T_{1\rho}$. Figure 2.18 shows the output of the electronics during a T_2 measurement sequence.

In order to measure the relaxation time during cyclic adiabatic inversion, one would follow the steps for a $T_{1\rho}$ measurement, but would make certain that the duration of the CAI cycle was long enough that the force on the oscillator had decayed substantially. The decay of the force can then be fit to

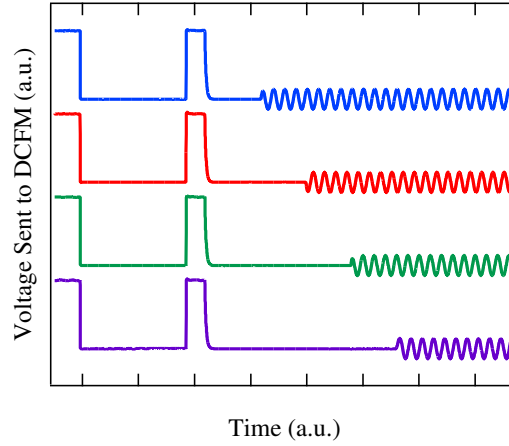


Figure 2.18: Spin-lattice relaxation time $T_{1\rho}$ measurement sequence. Each curve is a digitized signal from the output of the electronics. The traces have been offset vertically for clarity.

an exponential with a characteristic time T_{CAI} . The variations on this study are found in the frequency modulation amplitude Ω and the RF field strength \mathbf{H}_1 . As described in the § 3.2, by changing the relative sizes of these two parameters, the spins can see either an effective field that is closer to \mathbf{H}_o or \mathbf{H}_1 in magnitude. In these cases, T_{CAI} will approach T_1 and $T_{1\rho}$, respectively.

2.5 RF Signal Artifact

The presence of RF near the oscillator results in a spurious vibration amplitude. Thus, when cyclic adiabatic inversion is performed, the oscillator appears to ring-up. The following is a detailed study of the parameters of the RF that affect the presence of the RF signal artifact. The parameters investigated included power of the RF with and without FM, frequency of

FM, FM amplitude, and carrier frequency of the RF.

All of the data presented here was taken with the probe isolated from environmental noise by a half-inflated rubber inner tube upon which heavy lead bricks (and the probe) were placed; this spring-mass system formed a low-pass filter with a resonance frequency of roughly 1 Hz. This vibration isolation is far superior to that when the probe is in the NMR magnet. This study is, therefore, ideal for determining the direct effects of the RF magnetic field H_1 on the oscillator.

2.5.1 Experimental Method

The oscillator under investigation was determined in the manner described in Section 2.1.1.1 to have a resonance frequency of 4007.0 Hz, and a quality factor of 2500. The tank circuit of the probe was tuned to 344.817 MHz using the Smith Chart function of a network analyzer. The interference pattern of the interferometer had a peak-to-peak amplitude of 2.0 V. The fringe-locking circuit was used to lock to the smooth, positive slope of the fringe. The cyclic adiabatic inversion RF sequence used, with home-made decay and modulation electronics guiding the FM through the DCFM input of a HP 6546B signal generator. The lock-in amplifier was used with a time constant of 30 ms, and sensitivity of 500 mV; its internal reference frequency was used instead of the DS345 signal generator. The X and Y outputs of the lock-in were digitized with the Nicolet digital oscilloscope.

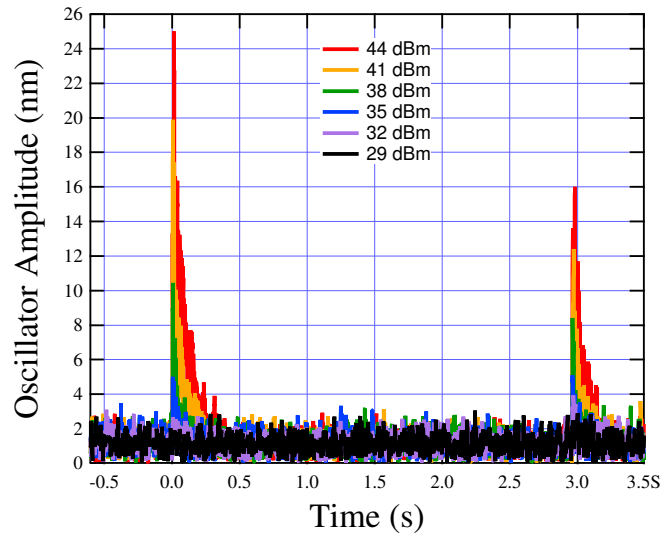


Figure 2.19: Mechanical ringing occurs when the RF field is turned on or off.

2.5.2 Initial Ringing

When the RF is introduced and removed, with or without frequency modulation, the artifact shows two impulses followed by their decay. Examples of these spikes for various power levels and no frequency modulation are presented in Figs. 2.19 and 2.20. The ring-down is periodic with a frequency of 100 Hz, supporting the mechanical ringing hypothesis. The peak amplitude of this ringing is shown in Fig. 2.21 to depend heavily on the RF power. These spikes are presumably caused by Lenz's law and the ensuing mechanical ringing of the coil itself.

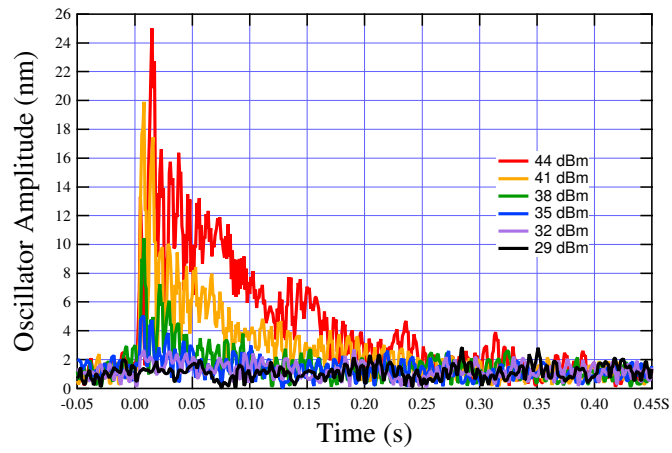


Figure 2.20: Zoom showing the detail in the mechanical ringing. The oscillations have a frequency of 100 Hz.

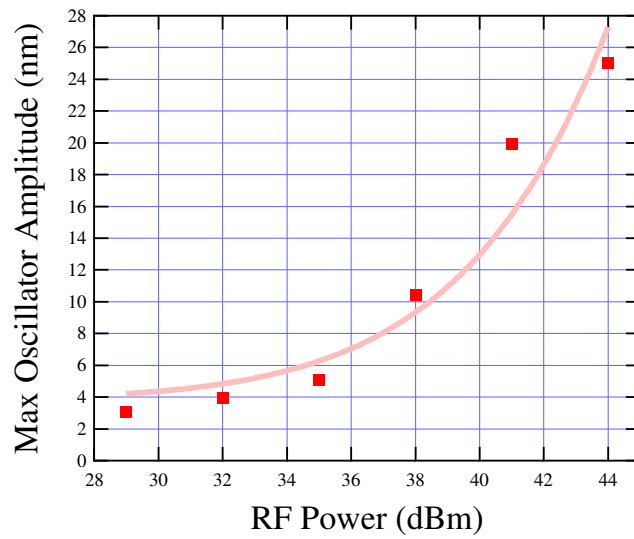


Figure 2.21: Peak mechanical ringing amplitude as a function of RF power. The solid line is a fit of the data

2.5.3 Frequency Modulation Effects

When frequency modulation at the oscillator's resonance frequency is turned on, the oscillator is excited to a steady state amplitude. For these data, unless noted, the RF power from the HP signal generator was held constant at -6 dBm, (corresponding to $+35.1$ dBm sent to the tuned tank circuit¹⁵), and the modulation amplitude was 100 kHz. Figure 2.22 shows the effect of the FM for various delay times between initial RF turn-on and initiation of the FM. The steady state amplitude of the excited oscillator is shown to be a function of RF power in Fig. 2.23.

If the frequency of the FM (f_{FM}) is slightly different from the oscillator's resonance frequency (f_{osc}), an oscillating amplitude is observed. Examples of low and moderate frequency beats are shown in Fig. 2.24 The frequency of these beats is equal to the absolute frequency difference

$$f_{beat} = | f_{FM} - f_{osc} | .$$

Using a least squares fitting algorithm in Igor, the beat amplitude was fit to a sine wave for several modulation frequencies. The dependence of the beat frequency as a function of the modulation frequency is shown in Fig. 2.25, and the dependence of the beat amplitude is shown in Fig. 2.26.

The next parameter we investigated was the FM amplitude Ω . Here, the modulation frequency was 4007.0 Hz. Figure 2.27 shows the dependence

¹⁵The one stage of the $+50$ dBm amplifier is burned out, resulting in a total amplification of $+41.1$ dBm.

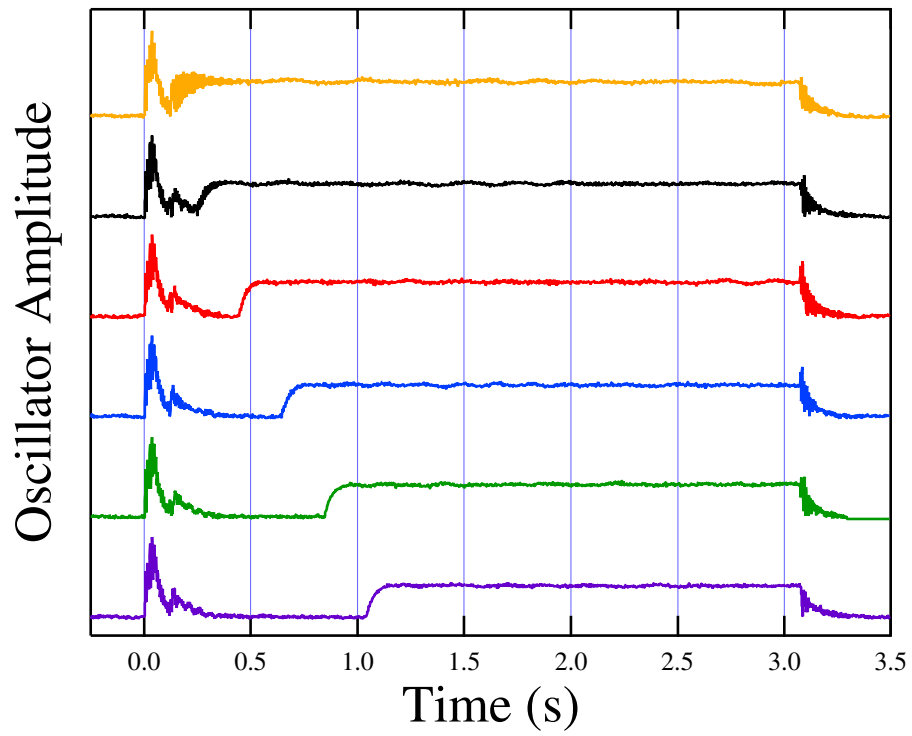


Figure 2.22: The delay time for turn on of the FM shows the dependence of the oscillator ring-up on the presence of the FM. The amplitudes of the steady-state values are roughly 22 nm for each curve.

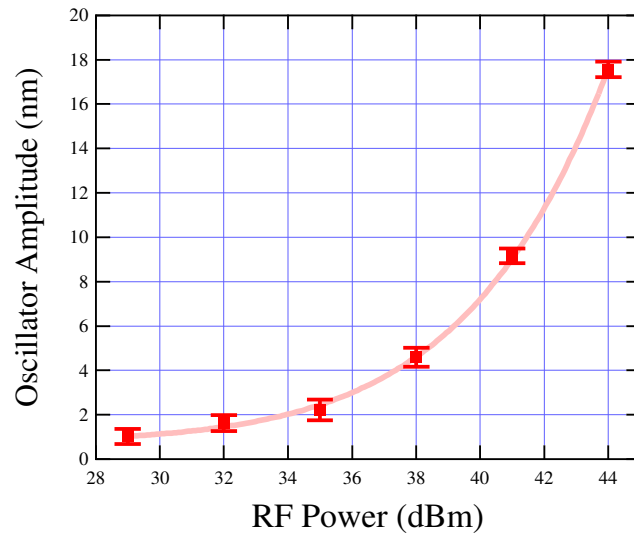


Figure 2.23: Steady state amplitude of the oscillator in the presence of FM as a function of RF power. The solid line is a fit of the data.

of the steady-state value of the oscillator excitation as a function of Ω .

2.5.4 Relative Tuning of Tank Circuit

We also investigated the affect of not having the tank circuit tuned to the carrier frequency of the RF. For these data, the RF power was +41.1 dBm, the FM modulation frequency was 4007.0 Hz, and Ω was 100 kHz. Since the tank circuit had previously been tuned to 344.817 MHz, we simply changed the carrier frequency instead of changing the actual tuning of the circuit itself. As the data in Fig. 2.28 shows, the steady state amplitude of the oscillator is strongly dependent on the carrier frequency. There is a small region around the tuned frequency where the artifact level has a local minimum. The width

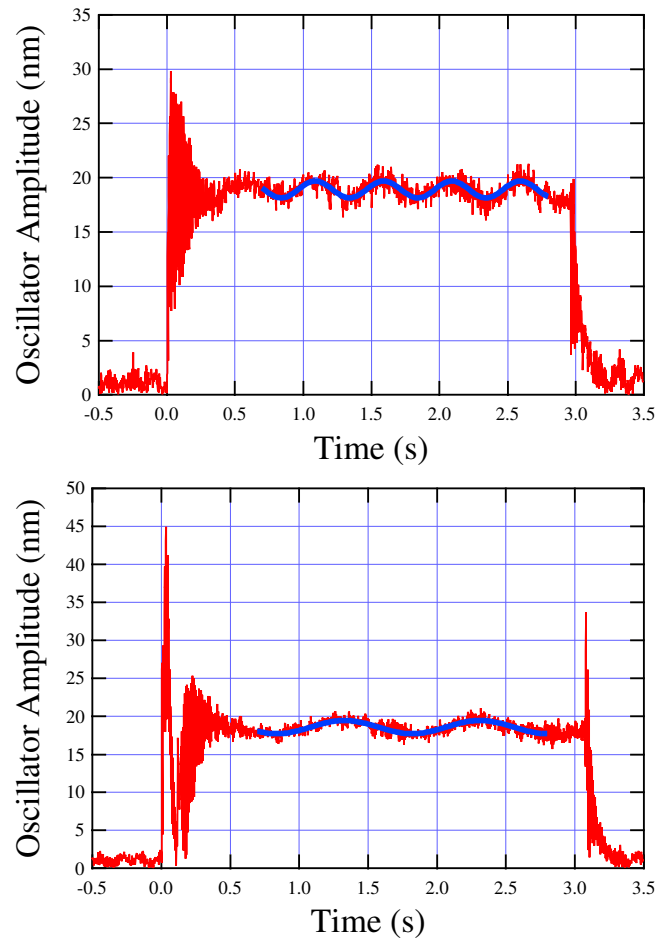


Figure 2.24: Beats due to a difference in FM modulation frequency and the oscillator resonance frequency. The blue curves on each are fits to a sine function.

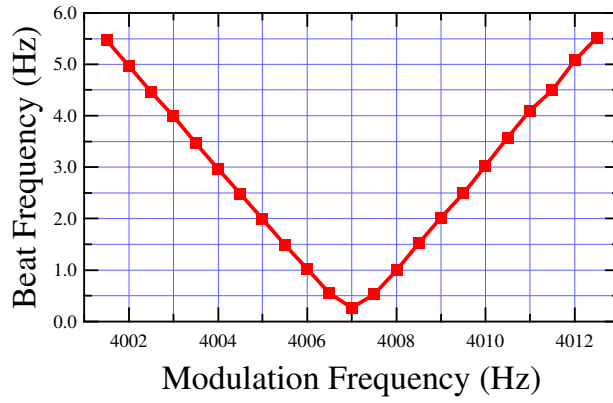


Figure 2.25: Beat frequency of artifact as a function of the FM modulation frequency.

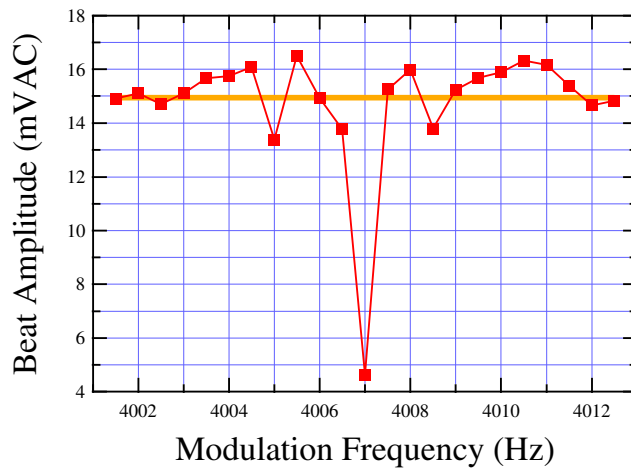


Figure 2.26: AC beat amplitude of the oscillator in the presence of FM as a function of FM modulation frequency.

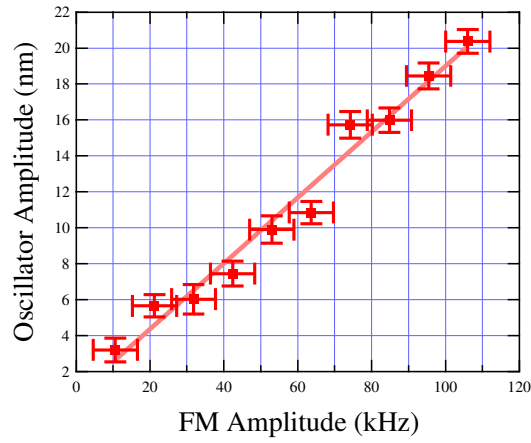


Figure 2.27: Steady state amplitude of the artifact in the presence of FM as a function of FM amplitude. The solid line is a linear fit to the data, which yields $A/nm = 0.70 + 0.18\Omega/\text{kHz}$.

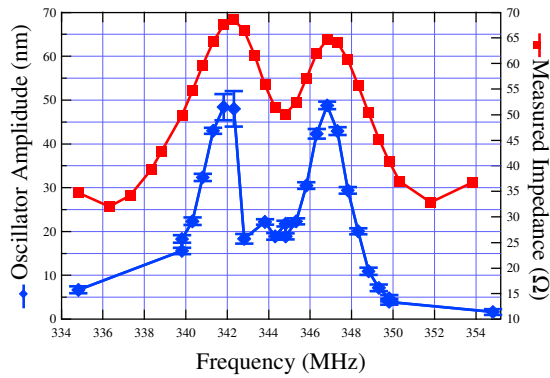


Figure 2.28: Steady state amplitude of the oscillator artifact (blue) as a function of RF carrier frequency. Also shown (red) is the measured impedance of the tank circuit for each frequency.

of this minimum may be advantageous to running long experiments because the tuning of the coil can be moderately dynamic. Additionally plotted on Fig. 2.28 is the measured impedance of the tank circuit for each frequency that was used in the experiment. The plotted impedance was calculated as $Z = \sqrt{Z_{re}^2 + Z_{im}^2}$, where the real and imaginary parts were measured with the network analyzer.

2.6 Laser-Induced Self-Excitation of Oscillators

An interesting “problem” was recently discovered: laser-induced self-excitation of the oscillator. This is a fairly well-known effect that has been researched by others [41–44]. Briefly: absorbed light energy (the “photothermal effect”) causes the oscillator to bend in, say, the $+\hat{z}$ direction. If the slope of the interference pattern is such that moving in this direction decreases the absorbed energy, then the oscillator cools and tries to return to its equilibrium position. However, as it passes its equilibrium position, it absorbs more light, heats up, and bends back toward the $+\hat{z}$ direction. This kind of cycle results in a positive feedback loop that causes the self-oscillation phenomenon. On the other side of the interference fringe, negative feedback is established because the heating and deflection are out of phase; the oscillator’s amplitude is consequently damped. Figure 2.29 shows the resulting behavior of the fringes. The “cold side” of the fringe resembles what would be expected for any interference pattern. The “hot side” has a region in space where the self-oscillations occur. The boundaries of this region are where the slope of the fringe becomes

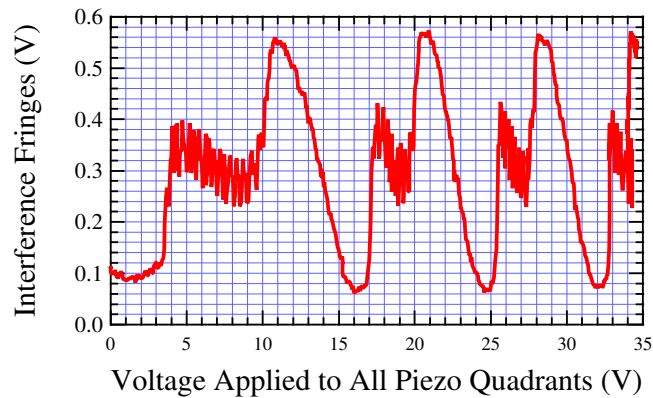


Figure 2.29: Interference pattern showing the smooth “cold” side and the “hot” side of the fringe for four successive fringes. The data have not been corrected for the hysteresis of the tube piezo, so the fringes appear to have an unequal peak-to-peak separation.

too small to induce the positive feedback. The interference pattern shown was digitized with the Nicolet as the voltage on the tube piezo was increased from zero. The trace on an oscilloscope that corresponds to each point on the fringe should be a flat line, and it is just that for the cold side. The hot side, however, causes the trace to be a sinusoid. This is the oscillator’s deflection amplitude¹⁶.

We performed a detailed analysis of the self-excitation phenomenon to determine the severity of its existence. We compared the amplitude of the oscillator as a function of a driving voltage applied to the piezo plate on which the oscillator was mounted for both the hot and cold sides of the fringe. All

¹⁶The sinusoid will also be seen on the cold side if the piezo plate is used to drive the oscillator.

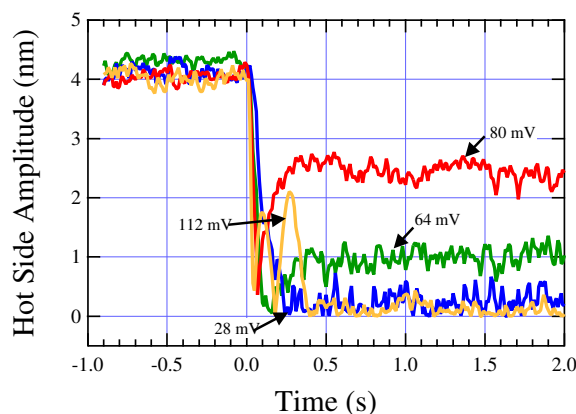


Figure 2.30: Digitized lock-in signal as an external force is applied to the oscillator with the interferometer locked to the hot side of the fringe. The steady-state amplitude for $t < 0$ is the self-excitation. Only four curves are shown because otherwise the behavior would make the graph a mess. The AC voltage sent to the piezo plate is indicated for each curve. The strange behavior for the 112 mV curve is repeatable, and is included as an example of the oddity of the hot side response.

data shown used a 30 ms lock-in time constant. Figures 2.30 and 2.31 show the amplitude of the oscillator before and after the driving force was applied (at $t = 0$ s) for the hot and cold sides of the fringe, respectively. Clearly, the cold side is more well behaved. Because of the uncanny response of the hot side, only a few of the time series are plotted. Figure 2.32 shows the RMS value of the steady-state driven amplitude ($t > 0.5$ s) for the data used in Figs. 2.30 and 2.31. The non-linearity of the hot side response indicates that meaningful force detection experiments may be almost impossible to analyze on this side of the fringe. This conclusion is further supported by Fig. 2.33, which shows that noise level is not well-behaved.

We believe this phenomenon has always been present in our microscope,

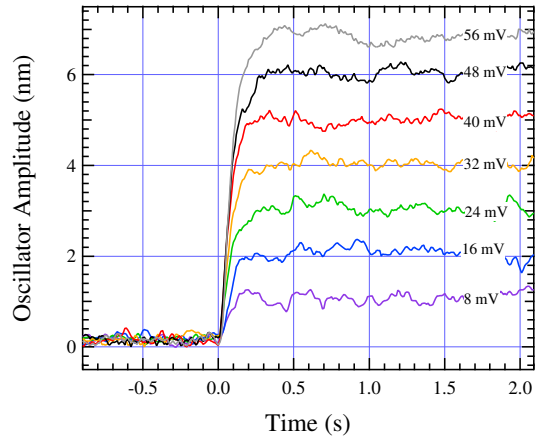


Figure 2.31: Digitized lock-in signal as an external force is applied to the oscillator with the interferometer locked to the cold side of the fringe. The AC voltage sent to the piezo plate is indicate for each curve. The steady-state driven amplitude scales linearly with the applied force. Note that the noise amplitudes are smaller than on the hot side.

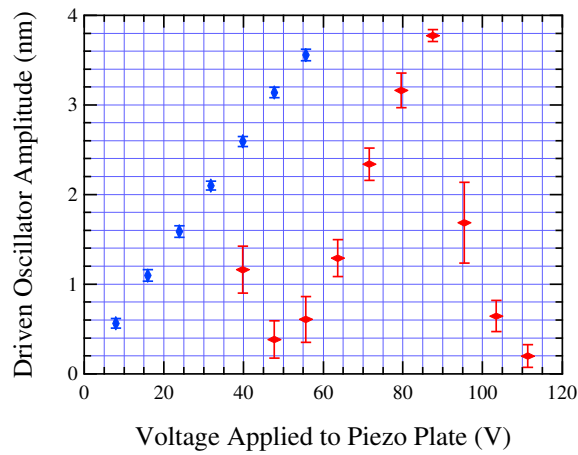


Figure 2.32: Steady-state driven amplitude of the oscillators for the cold side (blue, vertical diamonds) and the hot side (red, horizontal diamonds). The linear behavior of the cold side implies that it may be reliably used for force measurements, while the odd response of the hot side implies that it cannot be used at this time.

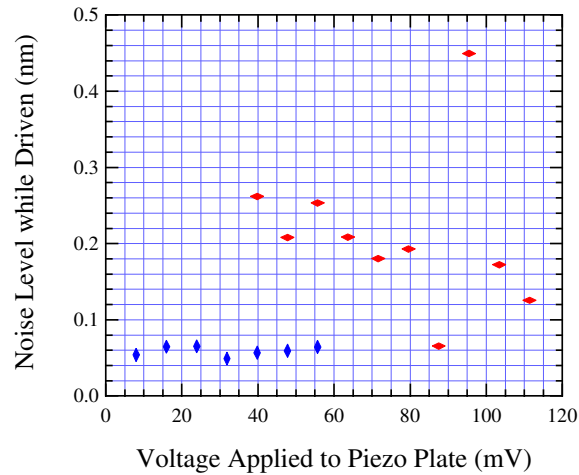


Figure 2.33: Noise level for the cold side (blue, vertical diamonds) and the hot side (red, horizontal diamonds). These data support the conclusion that the cold side is usable and the hot side is not.

but we have been unable to observe it until now for at least one of the following possible reasons. First, the fringe-locking circuit was upgraded to include the ability to lock to either slope of the interference pattern. Since the self-excitation only occurs on one slope, it is possible all of the previous locking circuits locked onto the smooth slope, leaving the oscillations undetected. Second, the addition of isolation virtually eliminated external vibrations from the probe. This allowed us to see crisp interference fringes with noise that was limited only by our electronics, and thus made the detection of the self-excitation easy.

The solution to the self-excitation problem is to have the oscillator absorb less light energy. One way to do this would be to change to infra-red

lasers. Silicon does not readily absorb infra-red, and actually has an absorption peak near our current laser wavelength. The other way around this problem is to use less light power. We currently deliver around 3 mW to the laser. Literature suggestions for the threshold power (i.e., the power below which the feedback loop is not functional) of oscillators with characteristics similar to ours are around 1 μ W [41].

In the future, however, it may be possible to take advantage of the self-excitation. We may be able to use the hot side of the fringe to synchronize the output of the DS345 function generator. This may be advantageous (or at least may make the hot side of the fringe usable) because the oscillator itself will then be controlling the phase of the force applied to it, be that from the piezo plate or from an actual NMR signal. If this were the case, then the amplitude of the signal would add constructively with an applied force. As it stands, one major reason for the non-linearity of the driven oscillator amplitude shown in Fig. 2.32 is likely the randomness of the phase of the self-excitation and the force from the piezo plate. Figure 2.34 shows that before the application of the driving force at $t = 0$ s, the self-excitation had a constant phase. The application of the force then alters this phase. For low driving voltages, the phase appears to decay into its new state, but for high voltages the transition seems rather violent. For completeness, Figure 2.35 shows the phase seen with the cold side of the fringe to be rather random before the force is applied. The oscillator immediately picks up the phase of the force, as indicated by the constant phase for $t > 0$ s.

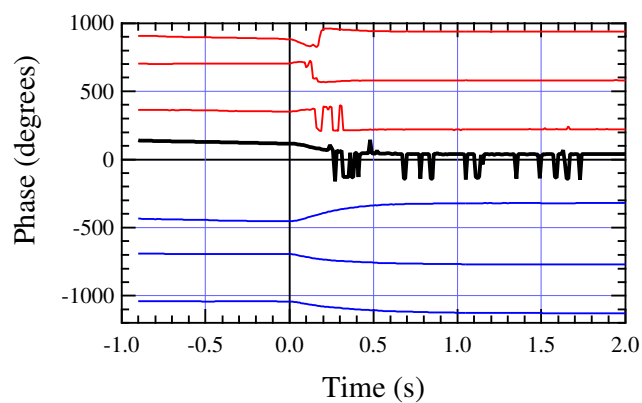


Figure 2.34: Phase relationship while being locked on the hot side before and after the driving force is applied. From bottom to top, the piezo plate's peak-to-peak driving voltages were 0.4 V, 0.5 V, 0.6 V, 0.7 V and 0.8 V. There is a transition at ~ 0.6 V, below which the phase of the oscillations smoothly incorporates the external force, and above which the phase is violently changed; the 0.6 V curve shows qualities of both regimes.

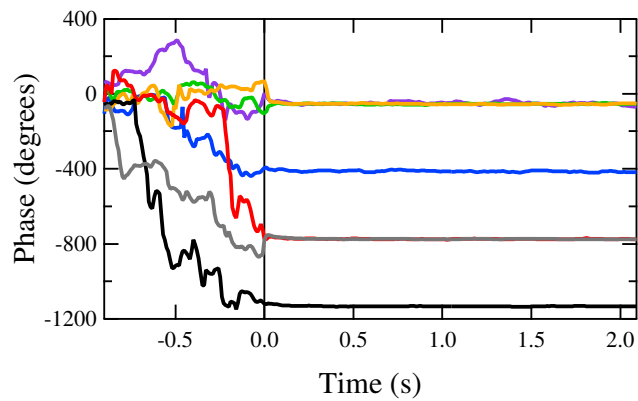


Figure 2.35: Phase relationship while being locked on the cold side before and after the driving force is applied. The curves are for different AC voltages sent to the piezo, but this is not the point of this graph. The point is to show the somewhat random nature of the phase for $t < 0$, which implies the absence of a significant driving force (i.e., there is no positive feedback loop). As a result, when the force from the piezo is applied, its (constant) phase is immediately assumed by the oscillator.

Chapter 3

Testing the Adiabatic Condition

“I don’t know what to tell ya’, Case...Have a drink for me.”

- John Markert, on the occasion of my laser exploding

In this chapter investigations of the adiabatic condition governing nuclear magnetic resonance force microscopy are described. The adiabatic condition is presented and the parameters involved are discussed in the light of the maximum allowable manipulated magnetization. Data is then presented that determines the necessary adiabatic factor for force detection of proton NMR in ammonium sulfate crystals using cyclic adiabatic inversion. Adiabatic following is then discussed in the theoretical terms of a “following probability” in the manner of Sawicki and Eberly [45]. The adiabatic following theory and our data are compared, and future investigations are presented to further test the applicability of this theory to NMR-FM.

3.1 Statement of the Adiabatic Condition

In its simplest form, the adiabatic condition says that the Larmor frequency of the spins must be much greater than the angular frequency of the

effective field. Translating this into a specific mathematical statement depends on the particular inversion scheme, but the general adiabatic condition can be written as

$$\gamma (H_{eff})_{min} \gg \left(\frac{d\phi}{dt} \right)_{max} \quad (3.1)$$

where $\gamma (H_{eff})_{min}$ is the minimum Larmor frequency of the spins, and $(d\phi/dt)_{max}$ is the maximum angular velocity of the direction of the effective field. In the case of cyclic adiabatic inversion where the frequency modulation is sinusoidal¹, $\gamma (H_{eff})_{min}$ is the rotating-frame Larmor frequency on resonance; the maximum angular velocity occurs as the field passes through resonance as well. With $\mathbf{H}_{eff} = (H_1, 0, (\Omega/\gamma) \sin(\omega_{osc}t))$, we define ϕ by

$$\tan \phi = \frac{\mathbf{H}_{eff} \cdot \hat{z}}{\mathbf{H}_{eff} \cdot \hat{x}'} \quad (3.2)$$

Simple differentiation results in the specific adiabatic statement for cyclic adiabatic inversion as

$$\gamma H_1 \gg \frac{\omega_{osc} \Omega}{\gamma H_1}. \quad (3.3)$$

The adiabatic conditional statement used throughout this work compares experimental parameters to unity, with a large number implying the adiabatic condition is well met:

$$\frac{(\gamma H_1)^2}{\omega_{osc} \Omega} \gg 1. \quad (3.4)$$

¹Other groups have used different modulations such as triangular FM [46]; determining the explicit adiabatic condition is a simple matter of differentiation.

The data presented in this chapter tests the level of adiabaticity necessary to lock spins during cyclic adiabatic inversion (i.e., determines what \gg really means for some particular spin system).

3.2 Ω - H_1 Parameter Space

Equation 3.4 implies the importance of three major experimental parameters, namely, the oscillator resonance frequency ω_{osc} , the frequency modulation amplitude Ω , and the RF field strength H_1 . The interplay between these three parameters will determine whether or not cyclic adiabatic inversion can be used.

While we do not have much control over ω_{osc} once the oscillators are fabricated, we have some control over both Ω and H_1 . Our current RF signal generator is capable of frequency modulating a carrier of up to 500 MHz with a modulation amplitude $\Omega \in [0, 100 \text{ kHz}]$ when operating in external DCFM mode. This simply means that a DC voltage of $\pm 1 \text{ V}$ input to the external modulation jack will shift the RF frequency output by the instrument by $\pm 100 \text{ kHz}$. The field strength H_1 is obviously dependent on the amplitude of the RF sent to the coil, which we can adjust from -120 dBm up to 13 dBm directly from the signal generator². If the $+50 \text{ dBm}$ RF amplifier is used and its input restrictions are observed, then the signal level can reach 50 dBm . With these parameters in hand, one may set out to map the NMR-FM response

²X dBm is defined relative to 1 mW of power as $X \text{ dBm} = \log_{10} \frac{P}{1 \text{ mW}}$. Thus, 0 dBm is equal to 1 mW, -3 dBm is 0.5 mW, etc.

throughout the Ω - H_1 parameter space of a particular sample.

3.2.1 Manipulated Magnetization

For a given set of parameters, how much magnetization can we expect to manipulate? For the following discussion, imagine we have all of the spins available locked without considering relaxation. The time varying \hat{z} component of the magnetization as a function of ω_{osc} , Ω and H_1 is given by Chabot as [27]:

$$M_z(t) = M_o \frac{\frac{\Omega}{\gamma} \sin \omega_{osc} t}{\sqrt{(\frac{\Omega}{\gamma} \sin \omega_{osc} t)^2 + H_1^2}}. \quad (3.5)$$

The maximum clearly occurs when $\sin \omega_{osc} t = 1$, so it helps to rewrite Eq. 3.5 as

$$\left(\frac{M_z}{M_o}\right)_{max} = \frac{\frac{\Omega}{\gamma}}{\sqrt{(\frac{\Omega}{\gamma})^2 + H_1^2}}, \quad (3.6)$$

which we can reduce to³

$$\left(\frac{M_z}{M_o}\right)_{max} = \frac{1}{\sqrt{1 + (\frac{\gamma H_1}{\Omega})^2}}. \quad (3.7)$$

A plot of $\left(\frac{M_z}{M_o}\right)_{max}$ as a function of Ω is given in Figure 3.1 for several H_1 . Additionally, a plot of $\left(\frac{M_z}{M_o}\right)_{max}$ as a function of H_1 is given in Figure 3.2 for several Ω .

From Eq. 3.7 we see that the maximum magnetization one can expect to manipulate is independent of the oscillator resonance frequency. This seems,

³This form shows an interesting similarity to the adiabatic statement of Eq. 3.4.

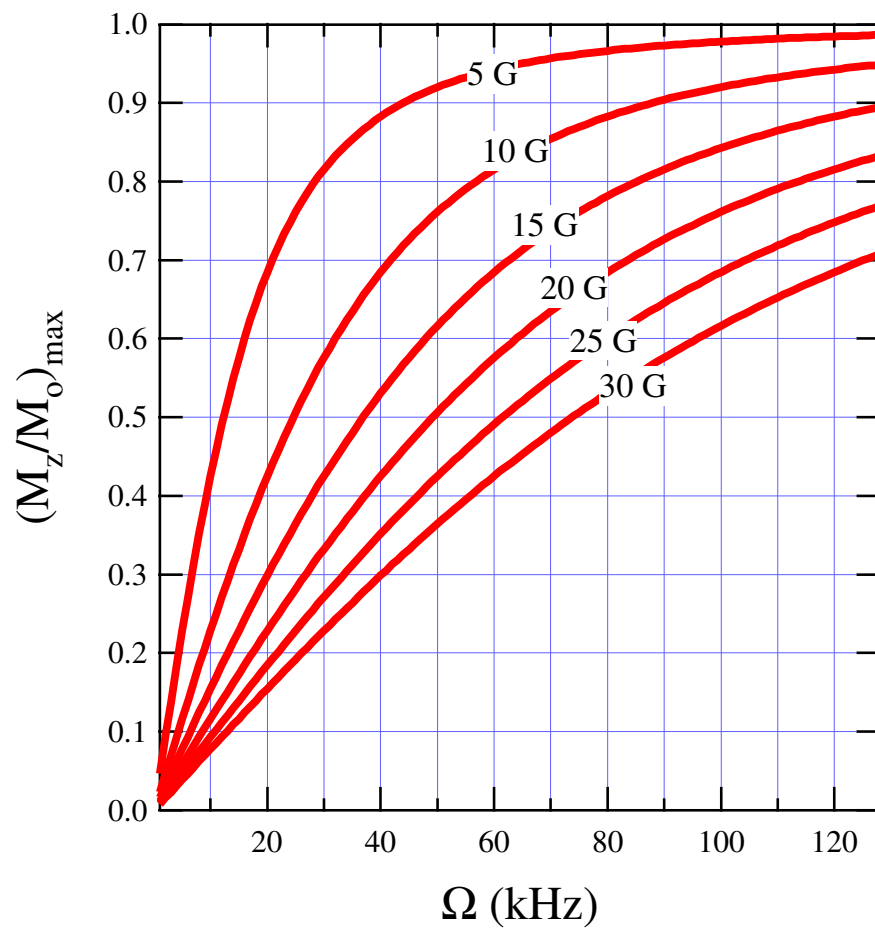


Figure 3.1: Maximum allowed magnetization in the \hat{z} direction as a function of the FM modulation amplitude Ω , according to Eq. 3.7. RF field strengths are indicated on each curve.

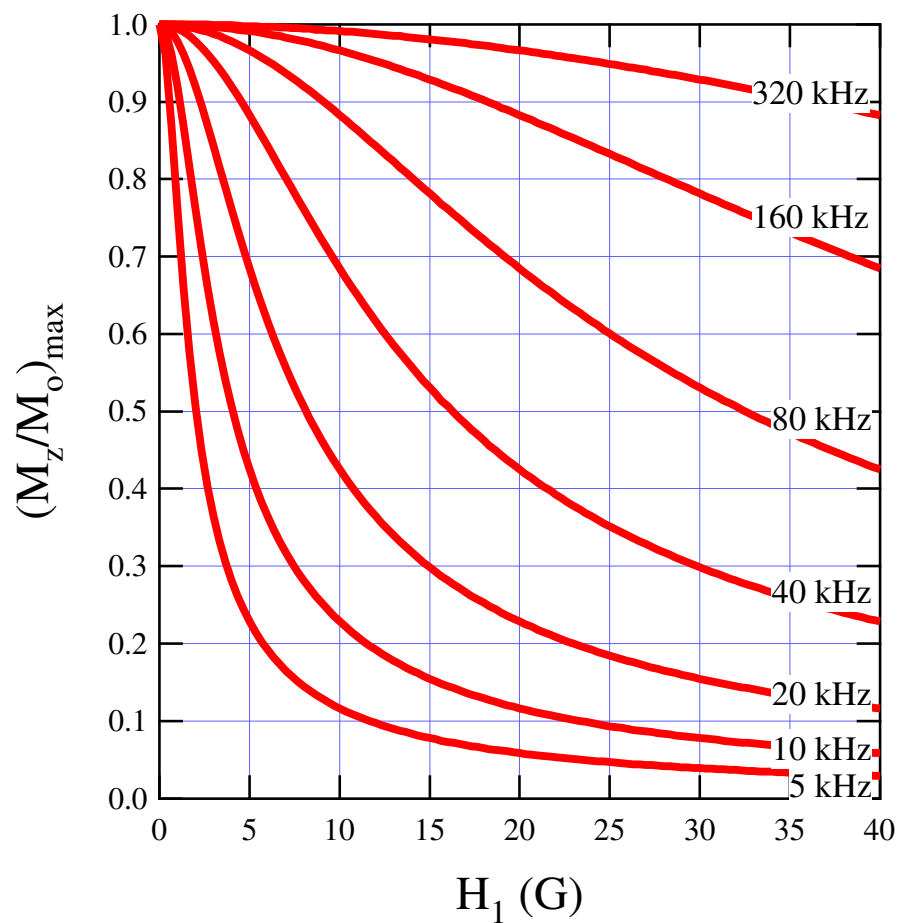


Figure 3.2: Maximum allowed magnetization in the \hat{z} direction as a function of the RF field strength H_1 , according to Eq. 3.7. FM modulation amplitudes are indicated on each curve.

at first glance, to be odd given our assumption that all of the spins are locked. This confusion can be easily remedied by considering the components of the effective field vector: $\mathbf{H}_{eff} = (H_1, 0, \Omega/\gamma)$. Because both the field strength and modulation amplitude play important roles, the most convenient parameter is actually the angle \mathbf{H}_{eff} makes with the \hat{x}' axis, namely $\phi = \tan^{-1}(\frac{\Omega}{\gamma H_1})$. Thus, when one adjusts the relative size of the two independent parameters Ω and H_1 , then ϕ is also adjusted. For $\phi \sim \pi/2$, $\Omega/\gamma \gg H_1$, and $\mathbf{M}_z \sim \mathbf{M}_o$. On the other hand, for $\phi \sim 0$, $\mathbf{M}_z \sim 0$. The idea to take home here is that in order to have most of the magnetization under your control, *regardless of your detection scheme*, Ω/γ should be much greater than H_1 . This again raises the question: “what does much greater than” really mean?

3.2.2 What does “much greater than” really mean?

Ah, the age old question of physicists...If you ask a famous theoretical physicist like Willy Fischler [47], “much greater than” means roughly ten times greater. Given that our experiments rely on a condition that requires an adiabaticity factor to be “much greater than” unity, we set out to experimentally answer the question, “what does much greater than really mean?”

3.2.2.1 Experimental Concerns

This proton-NMR-FM experiment was performed in the 8.073 T NMR magnet in the sample-on-oscillator configuration depicted in Fig. 3.3. The sample was a crystal of ammonium chloride, NH_4Cl , which was mounted onto

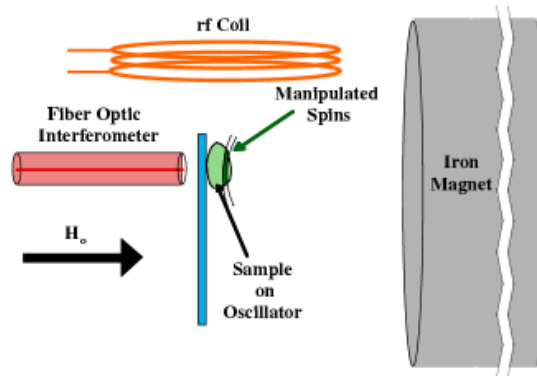


Figure 3.3: Experimental setup for the sample-on-oscillator configuration used in this study.

the head of a double torsional oscillator in the manner described in [27]. The sample was roughly a flat cylinder $10 \mu\text{m}$ thick and $25 \mu\text{m}$ in diameter. This salt was chosen for its abundance of protons ($6.9 \times 10^{22} \text{ }^1\text{H}/\text{cm}^3$), and for its long spin-lattice relaxation time at room temperature ($T_1 \sim 1 \text{ s}$).

The double torsional oscillator had an initial resonance frequency in a 15 mTorr vacuum of 6618 Hz, a quality factor of 900, and an estimated⁴ spring constant of 10^{-2} N/m . The minimum detectable force at room temperature was thus $2.1 \times 10^{-15} \text{ N}/\sqrt{\text{Hz}}$.

Figure 3.4 shows the oscillator resonance frequency as a function of time during the entire experiment. The resonance frequency of the oscillator increased noticeably during each run. The shift was found to be so dramatic

⁴The spring constant is estimated from modelling the normal modes of a double torsional oscillator. See [27] for more details.

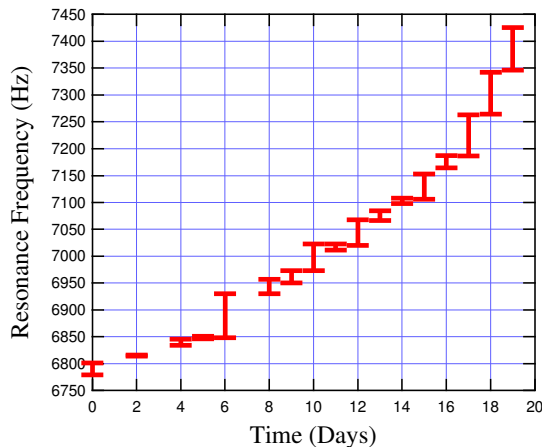


Figure 3.4: Range of resonance frequency of the oscillator each day as a function of time throughout the experiment. The frequency always increased (almost linearly) from the low end to the high end of the ranges indicated. The increase in frequency is attributed to the liberation of water from the sample.

that the DS345 frequency had to be adjusted to the new resonance each time the inversion cycle was performed. We attribute this effect to the liberation of water from the sample during prolonged exposure to vacuum.

The laser used for this experiment was a 660 nm Panasonic 50 mW (at 80 mA) laser diode. The current used during the experiment was held at 50 mA, resulting in a power of 3.7 mW delivered to the oscillator. The typical peak-peak fringe size that resulted was 2.3 V. To convert from fringe size to oscillator deflection, $2.3 V = \lambda/2\pi$ gave our conversion ratio as $1 V = 50.7 \text{ nm}$.

The permanent magnet that provided the field gradient was a 99.99% iron cylinder that was molded in an arc furnace. The cylinder was 44.0 mm long, and had a radius of 0.76 mm. Modelling of this cylinder (taking the

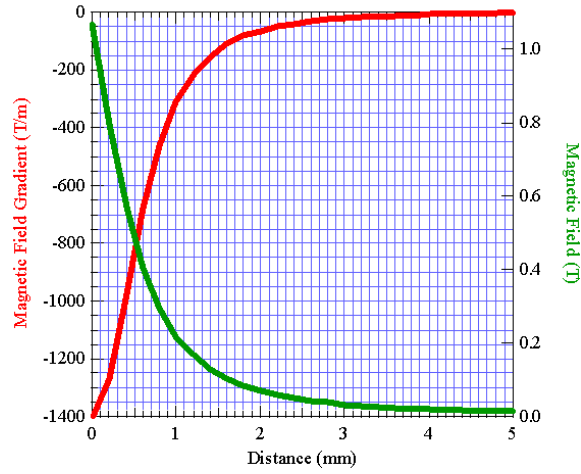


Figure 3.5: The modelled magnetic field (green) and magnetic field gradient (red) for the long bar magnet used in the experiment.

saturation magnetization of iron as 1700 emu/cc) yields the axial field, \mathbf{B}_z , and field gradient, $\nabla_z B_z$, as a function of distance depicted in Fig. 3.5.

The values of the field and its gradient from the permanent magnet at a given distance are important parameters that allow us to estimate our expected signal in two ways. First, the field in Curie's Law is the total field seen by the spins. Thus, to have an accurate estimate of the initial magnetization of a sample, the total field $H_o + H_{perm}$ needs to be used. Second, in order to estimate the expected force from the signal, the spatial extent of the resonance slice (i.e., how much of the sample is being manipulated) is needed. Additionally, knowing the total field is critical for determining the resonance frequency of the spins.

As mentioned previously, a reasonable estimate of the resonance slice

thickness, Δz , is

$$\Delta z = \frac{2\Omega}{\gamma \nabla_z B}. \quad (3.8)$$

For the purposes of this experiment, the resolution of the “image” of the sample was not a concern. As a result, the field gradient for operation was chosen to be that of the comfortable operating distance of 1 mm. The field gradient at 1 mm was -313 T/m, which yields a resonance slice thickness of $7.5 \mu\text{m}$ for $\Omega/\gamma = 50$ kHz. The field H_{perm} at 1 mm was 0.191 T, resulting in a total polarizing field of 8.264 T and a proton resonance frequency of 348.7 MHz.

Given the resonance slice thickness, the expected force was estimated via Curie’s Law for the magnetic moment M and the equation of force in the \hat{z} direction:

$$F_z = \left(\frac{1}{4} N (\gamma \hbar)^2 \frac{B}{k_B T} \right) \nabla_z B, \quad (3.9)$$

where N is the total number of spins contained within the resonance slice

$$\begin{aligned} N &= nV = nA\Delta z \\ &= 6.9 \times 10^{22} \text{ } ^1\text{H}/\text{cm}^3 \times \pi(25 \mu\text{m}/2)^2 \times 7.5 \mu\text{m} \\ &= 2.5 \times 10^8 \text{ } ^1\text{H}. \end{aligned} \quad (3.10)$$

Plugging our parameters into Eq. 3.9 yields an expected force of 7.1×10^{-14} N, and an expected signal-to-noise ratio (SNR) of 34.

As just demonstrated, an interesting way to rewrite Eq. 3.9 is to use Eq. 3.8 and $N = nA\Delta z$, where n is the proton density of the sample and $A\Delta z$

is the volume of the resonance slice inside of the sample:

$$\begin{aligned}
F_z &= \left(\frac{1}{4} \frac{(\gamma\hbar)^2}{k_B T} \right) nA(\Delta z) B \nabla_z B \\
&= \left(\frac{1}{4} \frac{(\gamma\hbar)^2}{k_B T} \right) nA \left(\frac{2\Omega}{\gamma \nabla_z B} \right) B \nabla_z B \\
&= \left(\frac{1}{4} \frac{(\gamma\hbar)^2}{k_B T} \right) nA \left(\frac{2\Omega}{\gamma} \right) B
\end{aligned} \tag{3.11}$$

From this final equation it is clear that if the resonance slice is smaller than the sample, then the force is independent of the field gradient. This is an optimistic point for NMR-FM because extremely large field gradients are necessary for high resolution images; Eq. 3.11 tells us there is no problem with this in terms of forces (line broadening and relaxation may be another story).

3.2.2.2 The Experiment

To record our data, the signal from the photodiode was fed directly into the lock-in, and its X and Y outputs were digitized with the Nicolet digital oscilloscope. The lock-in time constant for the entire experiment was 100 ms.

The permanent magnet was placed at an initial distance of 1.4 mm from the sample, and thus with roughly 300 μm between the oscillator and the resonance slice. Because we didn't know how much internal motion occurred during the violent act of inserting the probe into the NMR magnet, the initial search for the sample was done by moving the iron magnet away from the oscillator in steps of 15 μm . After no signal was seen over approximately 400 μm , the magnet was moved back toward the oscillator. A signal was detected at roughly 180 μm from the initial position. To check the validity

of this signal, the area in the range of 90 to 270 μm from the initial position was scanned again by retracting the magnet; the signal appeared again. The frequency of the RF was increased by 1 MHz to shift the resonance slice 100 μm closer to the magnet; the presence of the signal at this new position verified the NMR origin of our signal.

In order to map the $\Omega - H_1$ parameter space, we used $\Omega/\gamma \in [5, 40 \text{ kHz}]$ with $H_1 \sim 7 \text{ G}$. We actually also changed H_1 , but some jackass stole our computer and these data from the lab. For each value of the modulation amplitude, the iron magnet was scanned in 3 μm steps so that the resonance slice scanned through the sample, with considerable baseline measurements on each end of the scan. At each position, 5-8 scans were taken and averaged to represent the signal at that position. The baseline signals were all averaged together to represent the signal artifact, which is a spurious resonant excitation of the oscillator not associated with an NMR signal⁵. In order to determine the magnitude of the force on the oscillator, the signal artifact was subtracted from the averaged signal at each position. The resulting RMS amplitude at each position was taken as the NMR signal. The amplitude was converted to a force using the relation $F = k_{osc}A/Q$.

Instead of displaying a force versus Ω curve, we present our data in Fig. 3.6 as normalized SNR versus Ω . The normalized SNR is simply the experimentally measured SNR normalized to the theoretical SNR. We present

⁵A more detailed study of the signal artifact is presented in §2.5.

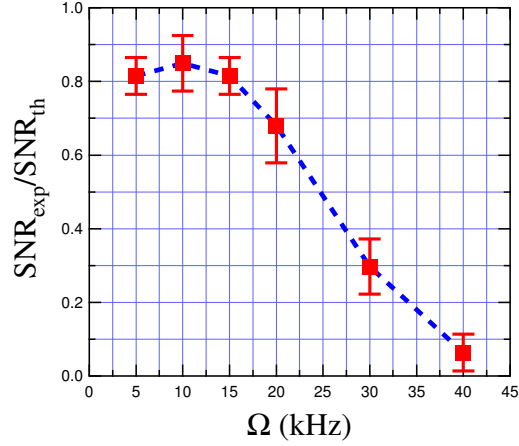


Figure 3.6: Data showing the normalized SNR as a function of the frequency modulation amplitude. The decrease in SNR is due to loss of spins because of violations of the adiabatic condition.

the data in this way because doing so implicitly accounts for the change in the resonance slice thickness ($\Delta z = 2\Omega/\gamma\nabla_z B_z$) for each Ω ; force data need more intricate massaging to do the same. That our normalized SNR does not reach unity implies that something was not optimal in either our theoretical SNR or in our measurement of the SNR. Because the level is constant within our error for the region where the adiabatic condition is well-met, we believe this to be an insignificant issue because it is most likely due to the approximated theoretical SNR.

Our data clearly show a decrease in the expected signal for large values of Ω . This is in contradiction to both the functionality of $(M_z/M_o)_{max}$, and the expected SNR, which is Ω -independent. The decrease in the signal with increasing Ω must then be due to violations of the adiabatic condition, which

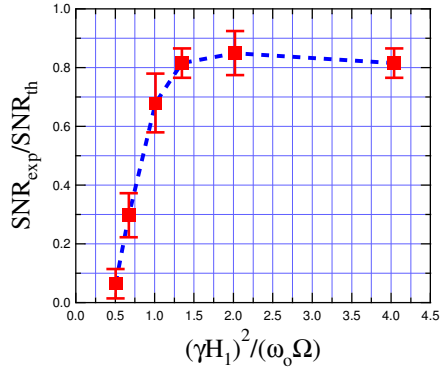


Figure 3.7: Data showing the normalized SNR as a function of the adiabaticity factor. The decrease in SNR is due to loss of spins because of violations of the adiabatic condition when the adiabaticity factor is small.

states $(\gamma H_1)^2 / \omega_{osc} \Omega \gg 1$. Figure 3.7 shows the normalized SNR as a function of the adiabaticity factor $(\gamma H_1)^2 / \omega_{osc} \Omega$. In this light, the transition between the two regimes is much more dramatic. The knee in the data occurs at $(\gamma H_1)^2 / \omega_{osc} \Omega \approx 1.5$. A previous study by Rugar’s group determined similar results for ^{19}F in CaF_2 [46].

Based on the conclusions of this study, “ \gg ” really means something more like “ $> 1.5\times$ ” for cyclic inversion of nuclear spins.

3.3 Adiabatic Following

The two-level system is one that is general and extends throughout physics. This is advantageous because such general research has been performed on the basic problem that their results can be applied to any one individual field without loss of generality. To end this chapter on the adia-

batic condition, we translate an interesting work by Sawicki and Eberly from its original application⁶ of laser induced population transfers in atoms to our nuclear spin interests. Future NMR-FM experiments with precise control of modulation parameters and RF field strength could be used to tune the adiabatic factor to experimentally verify the following theory.

3.3.1 Theoretical Formalism

To begin, imagine the magnetization in the rotating frame at equilibrium: $\mathbf{M} = (0, 0, M)$. If we apply an appropriate RF field, we can make the magnetization rotate uniformly in the rotating frame. If the angular velocity of this field is small compared to the Larmor frequency of the spins (both in the rotating frame), then adiabatic following (commonly called spin-locking) will be achieved. If, however, the angular velocity of the field is much greater than the Larmor frequency, then the spins will not be locked and will not follow the effective field vector.

The time evolution of the Bloch-vector \mathbf{M} is given by

$$\frac{d\mathbf{M}}{dt} = \gamma \mathbf{H}_{eff} \times \mathbf{M}, \quad (3.12)$$

where \mathbf{H}_{eff} is the “torque” vector about which \mathbf{M} rotates (the effective magnetic field), and γ is the gyromagnetic ratio of the spins. When the Rotating

⁶An interesting twist to the general idea of adiabatic following is also addressed in their work: diabatic following. According to their theory, if the effective field spins around extremely fast, it will give the Bloch vector a kick each time it passes it. Since this is in the extreme diabatic limit, the spins do not have time to relax, and inversion due to the kicks eventually occurs.

Wave Approximation (RWA) is used to transfer into the rotating frame, then one finds $\gamma\mathbf{H}_{eff} = (\gamma H_1, 0, \omega_o - \omega)$, or, equivalently, $\gamma\mathbf{H}_{eff} = (\gamma H_1, 0, \gamma H_z)$, where the third component is called the detuning (i.e., how far off resonance you are).

Now in order to make $\gamma\mathbf{H}_{eff}$ rotate uniformly we apply another “torque” vector, \mathbf{A} with constant magnitude in, say, the \hat{y}' direction. In this case, $\gamma\mathbf{H}_{eff}$ will have the same time evolution as \mathbf{M} , namely

$$\frac{d\gamma\mathbf{H}_{eff}}{dt} = \mathbf{A} \times \gamma\mathbf{H}_{eff}. \quad (3.13)$$

The effective field then becomes

$$\gamma\mathbf{H}_{eff} = (\pm\gamma H_{eff} \sin At, 0, \pm\gamma H_{eff} \cos At), \quad (3.14)$$

where $\gamma H_{eff} = \sqrt{(\gamma H_1)^2 + (\gamma H_z)^2}$. The solution that satisfies both Eq. 3.12 and Eq. 3.13 is called the spin-locking solution [48]:

$$\mathbf{M} = \pm (\gamma\mathbf{H}_{eff}(t) - \mathbf{A}) T, \quad (3.15)$$

The constant T has units of time and is under the constraint $\mathbf{M} \cdot \mathbf{M} = \mathbf{1}$, which is to say $(\gamma H_{eff}^2 + A^2)T^2 = 1$, where A is the angular velocity⁷ of $\gamma\mathbf{H}_{eff}$ about \mathbf{A} .

⁷At this point, observe the following regarding A and γH_{eff} : when $A \ll \gamma H_{eff}$, we are in the spin locking regime because the angular velocity of the effective field, \mathbf{A} , is small compared to the angular velocity of the spins, γH_{eff} . When $A \sim \gamma H_{eff}$, the adiabatic condition is being tested, and when $A \gg \gamma H_{eff}$ it is completely broken.

The exact solution of Eq. 3.13 can be written as

$$\begin{aligned}\gamma\mathbf{H}_{eff}(t) &= \hat{\mathbf{A}}(\hat{\mathbf{A}} \cdot \gamma\mathbf{H}_{effo}) + (\hat{\mathbf{A}} \times \gamma\mathbf{H}_{effo}) \sin At \\ &\quad + \hat{\mathbf{A}} \times (\hat{\mathbf{A}} \times \gamma\mathbf{H}_{effo}) \cos At,\end{aligned}\quad (3.16)$$

where $\hat{\mathbf{A}}$ is a unit vector along \mathbf{A} and $\gamma\mathbf{H}_{effo}$ is the initial effective field vector. If we assume $\gamma\mathbf{H}_{effo} = (0, 0, -\gamma H_{eff})$, then the time dependence can be written as

$$\gamma\mathbf{H}_{eff}(t) = -\gamma H_{eff}(\sin At, 0, \cos At). \quad (3.17)$$

At this point, it is useful to adopt a new coordinate system that is rotating with $\gamma\mathbf{H}_{eff}(t)$ about \mathbf{A} . The obvious orthogonal unit vectors of the new time dependent axes are

$$\begin{aligned}\hat{\mathbf{A}}(t) &= (0, 1, 0) \\ \gamma\hat{\mathbf{H}}_{eff}(t) &= -(\sin At, 0, \cos At) \\ \hat{\mathbf{A}}(t) \times \gamma\hat{\mathbf{H}}_{eff}(t) &= (-\cos At, 0, \sin(At)).\end{aligned}\quad (3.18)$$

Next, we need to write an equation for the Bloch vector in this new frame, namely

$$\mathbf{M}(t) = \alpha(t)\hat{\mathbf{A}} + \beta(t)\gamma\hat{\mathbf{H}}_{eff}(t) + \xi(t) \left(\hat{\mathbf{A}}(t) \times \gamma\hat{\mathbf{H}}_{eff}(t) \right), \quad (3.19)$$

where, from the Bloch Equation in coordinate form, the time dependent coef-

ficients α, β , and ξ obey the equations

$$\begin{aligned}\frac{d\alpha(t)}{dt} &= \gamma H_{eff} \xi(t), \\ \frac{d\beta(t)}{dt} &= A \xi(t), \\ \frac{d\xi(t)}{dt} &= -\gamma H_{eff} \alpha(t) - A \beta(t).\end{aligned}\tag{3.20}$$

With the rotated initial conditions $\mathbf{M} = (0, 1, 0)$, the solutions of these equations are given by

$$\begin{aligned}\alpha(t) &= \gamma H_{eff} A T^2 (\cos(t/T) - 1), \\ \beta(t) &= 1 + A^2 T^2 (\cos(t/T) - 1), \\ \xi(t) &= -AT \sin(t/T).\end{aligned}\tag{3.21}$$

The exact solution for the Bloch vector in our doubly-rotating coordinate system is found by substituting Eq. 3.21 directly into Eq. 3.19. This solution can then be rewritten in the coordinates of the original rotating frame as

$$\begin{aligned}& (AT \sin t/T \cos At - (1 + A^2 T^2 (\cos t/T - 1) \sin At)) \hat{x}' \\ & \quad + (\gamma H_{eff} A T^2 (\cos t/T - 1)) \hat{y}' \\ & + (-AT \sin t/T \sin At - (1 + A^2 T^2 (\cos t/T - 1)) \cos At) \hat{z}'\end{aligned}\tag{3.22}$$

3.3.2 The Inversion Probability P_π

The object of interest for adiabatic inversion is the probability of spins following $\gamma \mathbf{H}_{eff}$ through a rotation of π radians, P_π . In so doing, we tacitly

assume any spins that are lost will relax back to equilibrium with the static field. We determine P_π through the relation $P_{esc} + P_\pi = 1$, where P_{esc} , the probability to escape following, is defined [45] as

$$P_{esc} = \frac{1}{2}(1 - M_z(t)). \quad (3.23)$$

Thus, evaluating P_{esc} for the inversion time $t = \pi/A$ leads to the result

$$P_\pi = \frac{1}{2} \frac{A^2}{1 + (A/\gamma H_{eff})^2} \left(1 - \cos \left(\pi \frac{\sqrt{1 + (A^2/\gamma H_{eff}^2)}}{A/\gamma H_{eff}} \right) \right). \quad (3.24)$$

Using the trigonometric identity $1 - \cos \theta = 2 \sin^2(\theta/2)$ Eq. 3.24 reduces to the quite simple formula

$$P_\pi = 1 - \frac{A^2}{1 + (A/\gamma H_{eff})^2} \sin^2 \left(\frac{\pi}{2} \frac{\sqrt{1 + (A^2/\gamma H_{eff}^2)}}{(A/\gamma H_{eff})^2} \right). \quad (3.25)$$

To further illuminate this formula in the light of adiabatic inversion, we introduce a diabaticity parameter $\Lambda \equiv A/\gamma H_{eff}$. This parameter compares the angular velocity of the now rotating effective field to the angular velocity of the spins about the effective field. Thus, $\Lambda \rightarrow 0$ in the adiabatic limit of $\gamma H_{eff} \gg A$, and $\Lambda \rightarrow \infty$ in the diabatic limit of $A \gg \gamma H_{eff}$. Making this substitution in Eq. 3.25 leads to the equation

$$P_\pi = 1 - \frac{\Lambda^2}{1 + \Lambda^2} \sin^2 \left(\frac{\pi}{2} \frac{\sqrt{1 + \Lambda^2}}{\Lambda^2} \right). \quad (3.26)$$

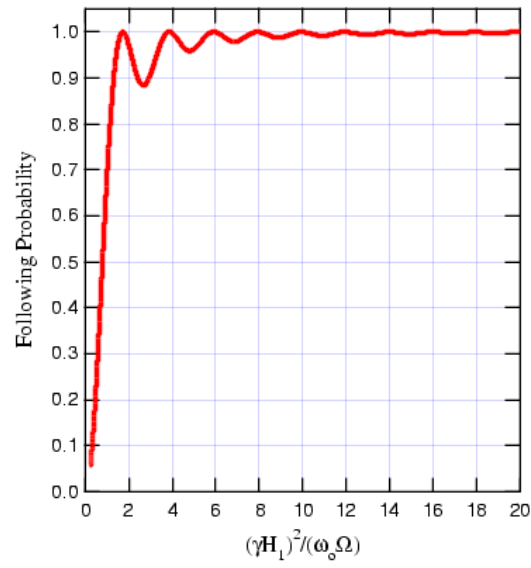


Figure 3.8: Adiabatic following probability vs adiabatic factor.

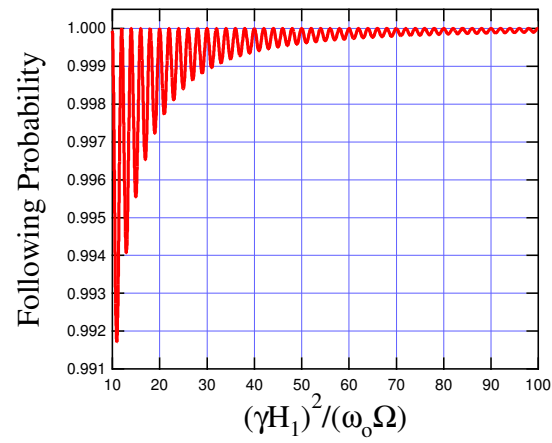


Figure 3.9: Adiabatic following with well-met adiabatic condition.

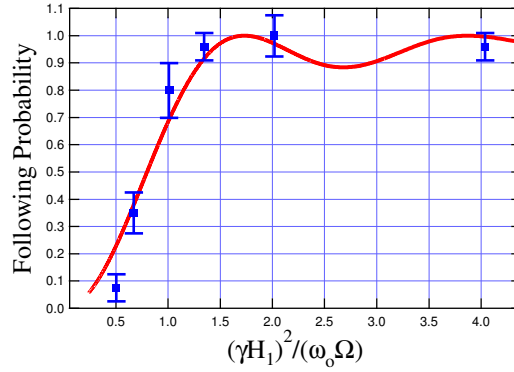


Figure 3.10: Experimental data using cyclic adiabatic inversion plotted with the theoretical curve for adiabatic following.

Figures 3.8 and 3.9 show Eq. 3.26 plotted as a function of the adiabaticity parameter applicable to our experiment, namely

$$\frac{1}{\Lambda} = \frac{(\gamma H_1)^2}{\omega_{osc} \Omega}. \quad (3.27)$$

The following probability P_π is unexpectedly intricate.

3.3.2.1 Application to Cyclic Adiabatic Inversion

Our cyclic adiabatic inversion data from Fig. 3.7 are presented again in Fig. 3.10 where they are shown with the theoretical curve of Fig. 3.8. The data points have been normalized to their maximum value for ease of comparison to the theory. We stress that no fit has been performed here, but the similarity between the data and theory seems to imply that this theory could apply to cyclic adiabatic inversion even though it inverts spins in a more simplistic way (i.e., where \mathbf{H}_{eff} has a constant magnitude throughout inversion). In

order to accurately fit this model to CAdI data, one might need to consider the following probability after n π rotations, which would result in a following probability of P_π^n . This seems like it might be wrong, however, since it would make the deviations of P_π from unity drop significantly in just a few cycles: for a nominal $P_\pi = 0.99$, we would find $P_\pi^9 = 0.0058$ after only nine π inversions; a CAdI cycle typically exists for thousands of oscillator cycles.

3.4 Future Adiabaticity Studies

An interesting future study would be to map out P_π for a given sample using NMR-FM. In order to meet the assumptions of the above theory, several experimental factors must be considered. First and foremost, how does one apply a field that is uniformly rotating in the traditional rotating frame? Other questions would be sample specific, revolving around relaxing agents in the form of impurities and dipole-dipole interactions.

The answer to the question of establishing a circular field in the rotating frame could be addressed via phase modulation, wherein both the amplitude and frequency of the RF field are time dependent. Establishing such a field may not be straightforward; although both modulation frequencies would be the same, the relative amplitudes may not be easy to precisely determine. With this in mind, the effective field would trace out an ellipse as depicted in Fig. 3.11, which has the representation $\mathbf{H}_{eff}(t) = (H_1 + \Delta H_1 \cos At, 0, H_o - \frac{1}{\gamma}(\omega_o + \Omega \sin At))$, where ΔH_1 is the amplitude of the AM, Ω is the amplitude of the FM, and A is the angular velocity of the above discussion. As the

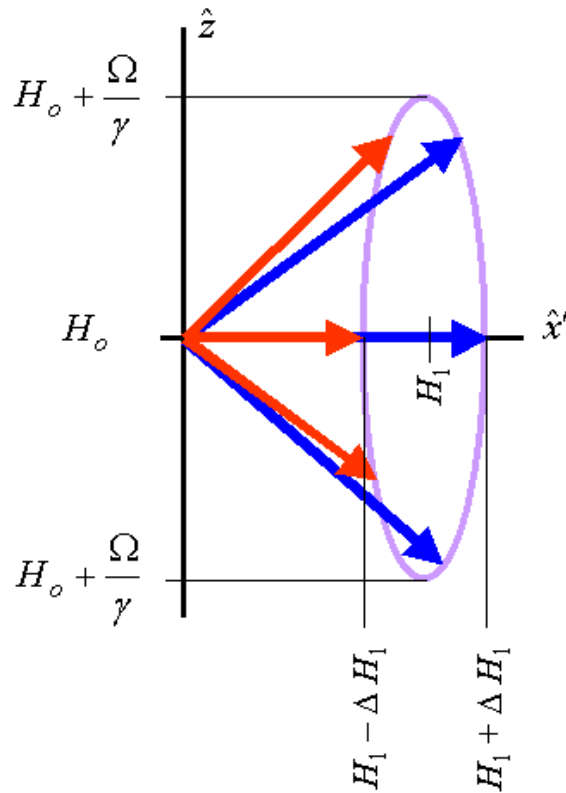


Figure 3.11: H_{eff} traces out an ellipse centered about H_1 with phase modulation if both the FM and AM have different modulation amplitudes.

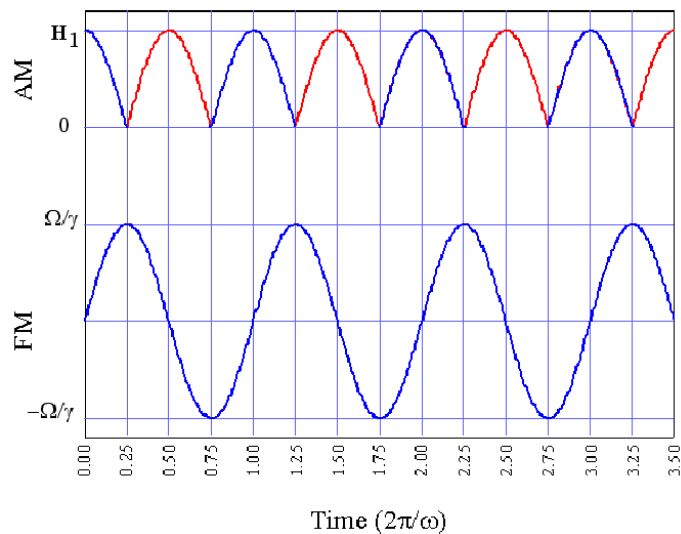


Figure 3.12: Schematic representation of the components required for the effective field to trace out a circle centered at the origin. The colors are used to imply relative phase; blue is $\phi = 0$, and red is $\phi = \pi$.

figure indicates, there is another problem with this method because the path of the effective field is not centered in the rotating frame. In order to produce such a field we need to introduce a π phase shift each half cycle when the RF amplitude is at its minimum. This could introduce some experimental difficulties for two reasons. First, the phase shift should occur sometime before the RF amplitude is below the local fields (2-3 G), as its presence will be meaningless otherwise and the spins will begin to relax. As a result, the second problem is the discontinuity in the \hat{x}' component; this may induce spins to become unlocked from \mathbf{H}_{eff} . A schematic representation of the effective field components required for a circularly rotating field is presented in Fig. 3.12, and the resulting curve it traces is given in Fig. 3.13.

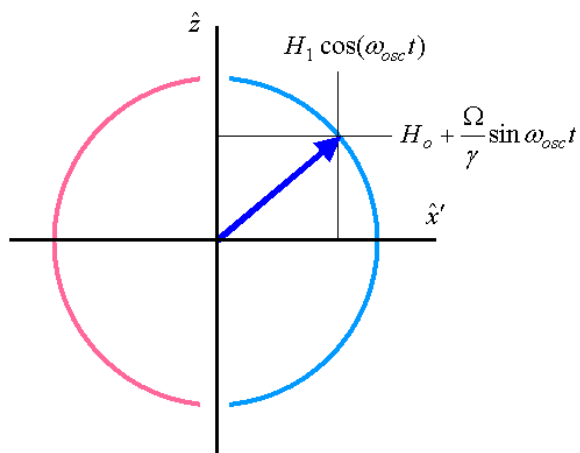


Figure 3.13: Effective field traces out a circle centered at the origin if appropriate measures are taken. The discontinuity in the curves near $x' = 0$ is the region where $H_{eff} \sim H_{local}$. The colors indicate different phase, as in Fig. 3.12.

Chapter 4

Field Effects on Oscillators Capped with Magnets

“I should have been a cowboy.”

- Toby Keith

In this chapter we discuss the characteristics of CoPt-capped single-crystal-silicon micro-oscillators when a magnetic field is applied perpendicular to the magnetic film. After discussing the motivations for this study, the experiment is described. Finally, experimental results and models that describe the observed behavior are presented.

4.1 Motivation and Introduction

Magnetic resonance force microscopy (MRFM) has advanced quite rapidly since its proposal by Sidles in 1991, with most work performed in the sample-on-oscillator configuration [49–53]. The eventual practical use of MRFM for biological and solid state imaging, however, is heavily dependent upon the successful conversion to the magnet-on-oscillator configuration. This configuration is often implemented with the external polarizing magnetic field, \mathbf{H}_o ,

parallel to the cantilever axis. Such a setup is used in order to minimize the interaction of the field with the magnetic particle [54, 55]. To our knowledge, this is the first study where \mathbf{H}_0 is normal to the face of the oscillator; this arrangement is necessary for operation in small bore (1.5 inch diameter) superconducting magnets, as the axis of the interferometer optical fiber must be, for the most part, parallel to the axis of the bore. Additionally, this configuration will ultimately be beneficial because it offers a more convenient field gradient geometry for MRFM image deconvolution as the highly symmetric field gradient pattern can be readily calculated, whereas other, irregular magnet geometries can provide force maps that are less straightforward to interpret.

The general experimental setup for a magnet-on-oscillator NMR-FM experiment is shown in Figure 4.1. The magnet on the oscillator generates a field gradient ∇B in the otherwise homogenous field \mathbf{H}_0 . In the presence of this field gradient, the magnetization \mathbf{M} of the sample imposes a force on the mechanical oscillator equal to $(\mathbf{M} \cdot \nabla)\mathbf{B}$. A frequency-modulated magnetic field is introduced using a radio-frequency coil to manipulate the spins of the sample in such a way that a thin slice of the magnetization, and thus the force on the oscillator, becomes a function of time. By cyclically inverting this magnetization at a frequency equal to the resonant frequency of the oscillator, a vibration amplitude measurable using a fiber optic interferometer is attained. The force sensitivity is limited by the thermal noise of the

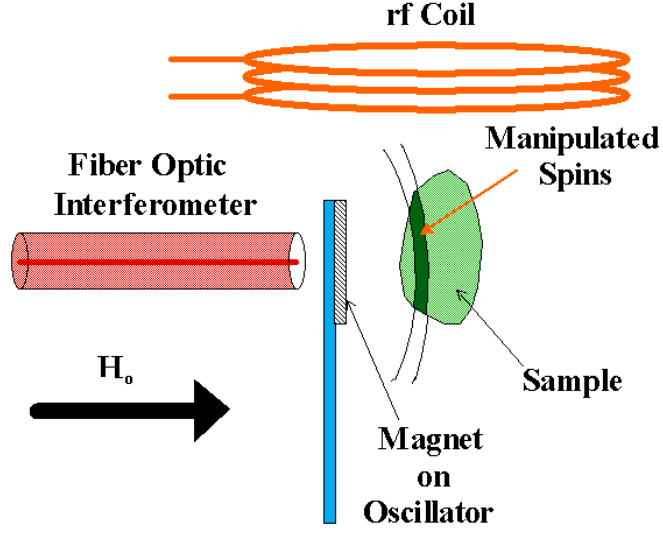


Figure 4.1: Schematic overview of magnet-on-oscillator experimental setup.

mechanical oscillator,

$$F_{min} = \sqrt{4k_B T k_{osc} \Delta\nu / Q \omega_{osc}}, \quad (4.1)$$

where k_{osc} , ω_{osc} , and Q are the spring constant, resonant frequency, and quality factor of the oscillator, and $\Delta\nu$ is the equivalent noise bandwidth¹ of the measurement. Typical oscillators fabricated in our lab are ~ 200 nm thick, have spring constants ~ 0.01 N/m, resonant frequencies ~ 10 kHz, and quality factors $\sim 10^3$, resulting in a nominal room temperature force sensitivity on the order of 10^{-15} N/ $\sqrt{\text{Hz}}$.

¹ $\Delta\nu = 1/4\tau$, where τ is the time constant of the lock-in amplifier with a 6 dB/oct filter. This changes depending on the slope of the filter chosen on the lock-in.

4.2 Experimental Details

The micro-magnets discussed in this work were CoPt² films deposited in our lab by Troy Messina. The dimensions of these magnets and their host oscillators are presented in Table 4.2, and schematics of the two types of oscillators

Table 4.1: Oscillator characteristics and magnet dimensions used in this study.

Oscillator	f_{osc} (kHz)	Q	l (μm)	w (μm)	t (nm)	magnet size
A (paddle)	6.545	200	10	120	80	1/8 head
B (double)	10.50	270	20	150	80	1/2 head
C (paddle)	5.840	190	75	120	80	whole head

used, paddles and double torsionals, are given in Figure 4.2. The oscillators used were processed in their entirety by Michelle Chabot as described in her dissertation [27].

The CoPt source was produced by arc melting stoichiometric mixtures of Co (99.9975% pure) and Pt (99.9999% pure) in a water-cooled copper hearth in a zirconium-guttered inert atmosphere. The single crystal silicon oscillators were then shadow masked with a razor blade under a microscope and placed in the vacuum chamber with a base pressure of 10^{-8} Torr. The CoPt films were deposited using electron-beam evaporation [56]; a film thickness of 80 ± 1 nm was measured by a quartz resonant growth monitor.

²For the sake of clarity, CoPt here means $\text{Co}_{0.50}\text{Pt}_{0.50}$, that is, a 1:1 molar ratio of cobalt to platinum. It is somewhat common in the literature to define the alloy initially as $\text{Co}_x\text{Pt}_{1-x}$, and to refer to it thereafter as simply CoPt or Co-Pt.

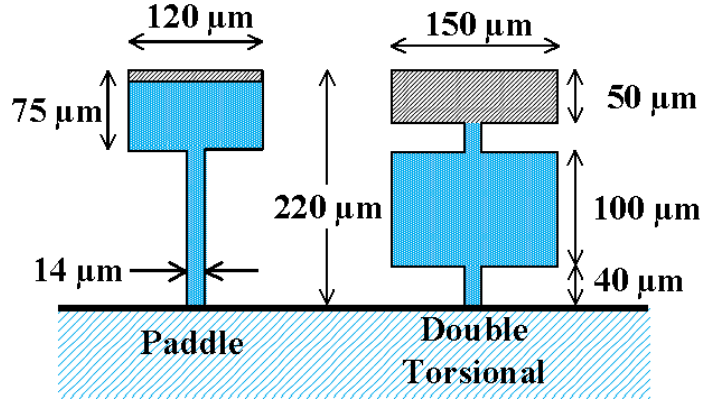


Figure 4.2: Oscillators used in these experiments.

To determine the effect of \mathbf{H}_o on the magnet-capped oscillators, room temperature frequency scans were performed in an exchange gas pressure of 100 mTorr using the probe built by Tobias Graf [57] in a High Field Magnet (HFM) for magnetic fields between -5 T and $+5$ T. Note that ideally the pressure would have been 1 mTorr or lower so as to optimize the quality factor of the oscillators [35]. Unfortunately, 100 mTorr was the lowest pressure attainable for this experiment. This high pressure is attributed to the combination of outgassing and low throughput to the pump due to the long, small diameter hose. The probe was leak checked with a helium leak detector by the Cryo Shop; no leaks were found. In retrospect, the pressure may have been limited by outgassing from the rubber vacuum hoses; metallic hoses have been used since this experiment to achieve pressures³ around 10^{-5} Torr.

³This pressure is read at the top of the probe; the pressure at the oscillators themselves (5 feet away from the gauge) is probably an order of magnitude higher.

The oscillators with magnets were glued to a piezo plate that applied a sinusoidal driving force. The vibration amplitude of the oscillators was detected using a fiber optic interferometer operating at 660 nm. For each of the oscillators discussed here, the first cantilever mode was utilized, as verified by phase-sensitive detection on opposite sides of the oscillator heads [18]. The resonant frequencies ω_{osc} , and quality factors Q , were determined by fitting the vibration amplitude to a Lorentzian using the least squares curve fitting algorithm in Igor Pro. The initial field application from 0 T to +5 T was irreversible for each of the magnets, and did not necessarily overlap with the reversible behavior observed thereafter. \mathbf{H}_o was changed from +5 T to -5 T and back to +5 T for each oscillator in anticipation of hysteretic behavior, though none was detected with the large field steps used here (several thousand Gauss, which is much greater than the coercive field perpendicular to any magnetic film). All changes of the field were done at the maximum allowed rate for the current in the HFM of 0.0075 A/s, which is roughly 12 G/s. No steps greater than 0.5 T were taken because the equilibrium position of the oscillators appeared to change with field strength, as deduced from shifting fringes in the interferometer signal.

The frequency shifts normalized to the zero field frequency of the magnet-capped oscillators and one bare paddle are shown in Figure 4.3. The initial frequency shift of the bare oscillator may be due to the paramagnetism of the heavily boron-doped single-crystal silicon. Note that the resonant frequency of the silicon paddles exhibit negligible field dependence in the high-

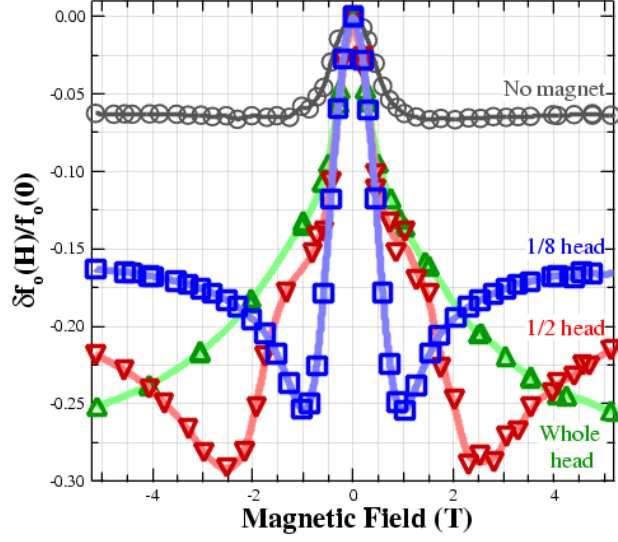


Figure 4.3: Normalized shift in resonant frequency for a bare paddle \circ and magnetically capped oscillators A, \square , B, ∇ , and C, \triangle .

field region of interest for NMR-FM. The magnet-capped oscillators exhibit two regimes of \mathbf{H}_0 dependence. The low-field behavior occurs while the strong shape anisotropy of the films confines the moment to the plane of the oscillator, and thus nearly perpendicular to \mathbf{H}_0 . The high-field behavior occurs when the field is strong enough to rotate the moment out of the plane, nearly aligned with \mathbf{H}_0 . Although the frequency increases at high fields, it never fully recovers to the zero-field frequency. This can be beneficial to NMR-FM experiments because lower oscillator frequencies help to meet the adiabatic condition for cyclic adiabatic inversion [58] of sample spins.

The quality factor dependence on external magnetic field is given in Figure 4.4. The Q of the magnet-capped oscillators decreased sharply in the

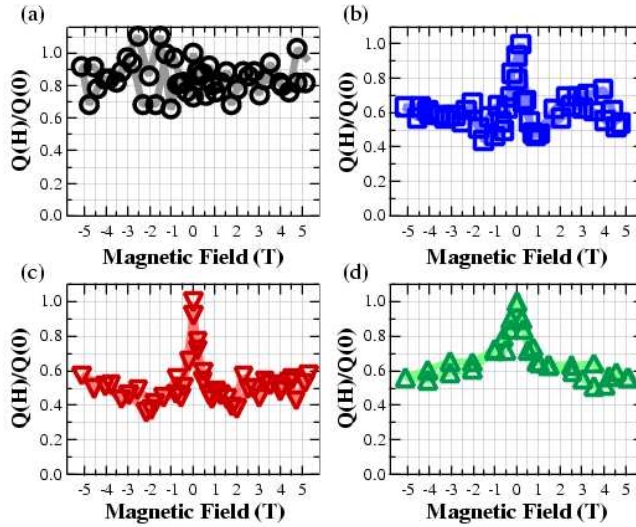


Figure 4.4: Quality factor dependence on field for a bare paddle \circ and magnetically capped oscillators A, \square , B, ∇ , and C, \triangle .

low field regime. The changes were extreme for each magnetically capped oscillator, with deviations as high as 70%. No appreciable shift was detected for the bare oscillator. In the high field regime the Q of the oscillators have less dramatic field dependence, and in the case of the 1/8 and 1/2 head magnets, the quality factor actually increases with higher fields though it never recovers its zero-field value. Though less obvious, these data show a transition point at the same field value (H_s) as that of the frequency data. The overall decrease in quality factor at high fields has a very small affect on our ultimate force sensitivity, which is proportional to $Q^{-1/2}$. No attempt to describe this behavior mathematically is presented at this time. Similar behavior was reported by Marohn's group at the MRFM workshop held at UT in March, 2003.

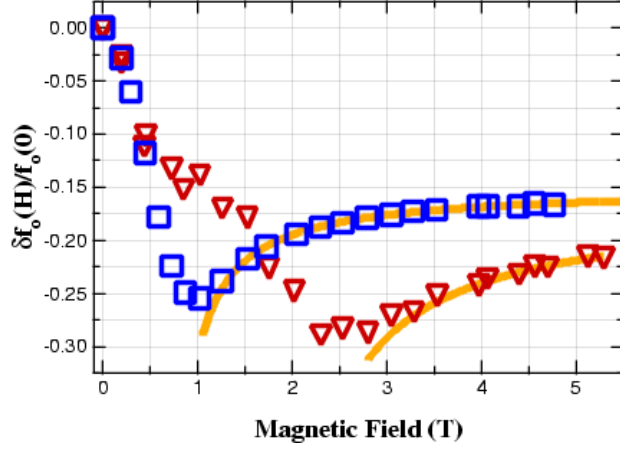


Figure 4.5: Normalized shift in resonant frequency oscillator A (1/8th capped head, \square), and oscillator B (1/2 head capped, ∇). The solid line is a fit of the high field data to the model used previously by Rugar's group.

4.3 Modelling of Data

4.3.1 High-Field Regime Model

The field dependence seen in the high-field regime is similar to that previously reported by Rugar for the geometry where \mathbf{H}_o is in the plane of the oscillator. The increase in resonant frequency with \mathbf{H}_o is due to an increase in the effective spring constant that is caused by the small restoring torque that is present. When the moment and \mathbf{H}_o are aligned, such magnetic stiffening causes a shift in the resonant frequency equal to

$$\frac{\Delta\omega_{osc}}{\omega_{osc}} = \frac{\mu H_o}{2k_{osc}L_{eff}^2} \left(\frac{H_k}{H_o + H_k} \right), \quad (4.2)$$

where μ is the moment of the magnet, H_k is the anisotropy field, and L_{eff} is the effective length of the cantilever [54]. Figure 4.5 shows the data for oscillators A and B fit to Eq. (4.2) with the substitution $H_o \rightarrow H_o + H_s$, where H_s is

an offset field above which the moment and \mathbf{H}_0 are nearly aligned. This offset field is necessary because for smaller fields the angle between the moment and the field is too large to reasonably utilize the small angle approximation, which is the backbone of this model. A least squares fit of the data to Eq. (4.2) allows us to determine μ , H_k , and H_s of oscillator A to be

$$\begin{aligned}\mu^A &= 7.1 \times 10^{-11} \text{ J/T}, \\ H_K^A &= 0.61 \text{ T}, \\ \text{and } H_s^A &= 1.21 \text{ T},\end{aligned}$$

while those of oscillator B were

$$\begin{aligned}\mu^B &= 1.6 \times 10^{-10} \text{ J/T}, \\ H_K^B &= 0.69 \text{ T}, \\ \text{and } H_s^B &= 2.27 \text{ T}.\end{aligned}$$

The measured moment values are in good agreement with those estimated from the magnet volumes and saturation magnetization of CoPt (750 kA/m) [59]: $\mu^A \approx 7.2 \times 10^{-11} \text{ J/T}$, $\mu^B \approx 1.6 \times 10^{-10} \text{ J/T}$.

This simple model, however, cannot explain the effects observed in the low-field regime. The model we propose for the low-field behavior considers the dependence of the magnetic energy on the direction of the magnetic moment with respect to the three primary directions of the film. We model the magnetization of the film as a single domain that initially lies in the \hat{x} direction, and that is confined to the \hat{x} - \hat{z} plane. Further, we assume the oscillations of the

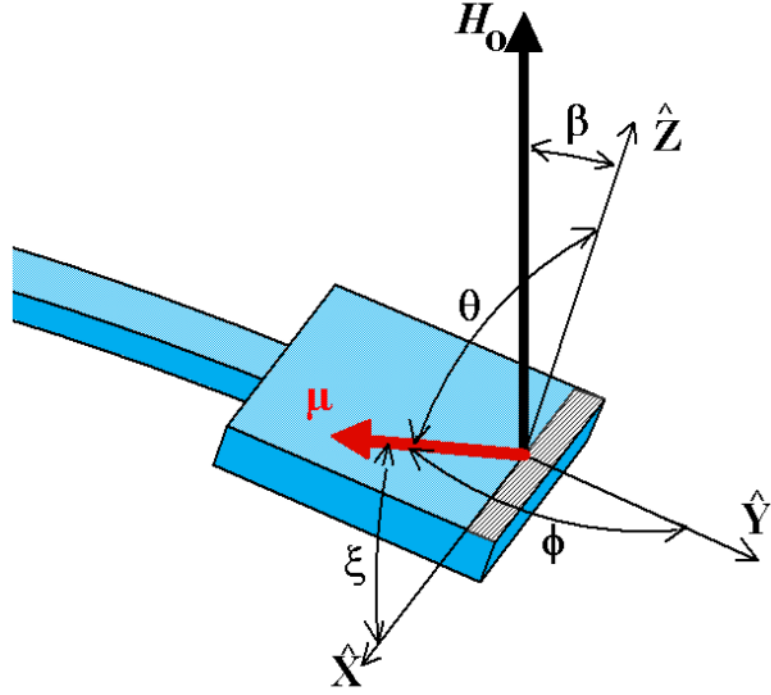


Figure 4.6: Schematic illustrating the coordinate system used in our low field model.

cantilever occur in the \hat{y} - \hat{z} plane. Additional assumptions will be mentioned within the derivation of this low-field model.

4.3.2 Low-Field Regime Model

We start by writing a general energy density equation that contains only anisotropy and Zeeman energy terms:

$$\frac{E}{V} = K_{\hat{x}} \sin^2 \xi + K_{\hat{y}} \sin^2 \phi + K_{\hat{z}} \sin^2 \theta - M_s H \cos \angle(\vec{\mu}, \mathbf{H}), \quad (4.3)$$

where ξ , ϕ , and θ are the angles from the primary axes of the micro-magnet \hat{x} , \hat{y} and \hat{z} , respectively, as shown in Figure 4.6. We take $\vec{\mu} = \mu(\cos \xi, \cos \phi, \cos \theta)$,

and our assumption that the oscillations of the cantilever occur solely in the \hat{y} - \hat{z} plane leads to $\mathbf{H} = H(0, -\sin\beta, \cos\beta)$, where β is the tilt angle of the cantilever relative to the field. Using the definition of the dot product, we find

$$\cos\angle(\vec{\mu}, \mathbf{H}) = -\sin\beta\cos\phi + \cos\beta\cos\theta. \quad (4.4)$$

We make a small angle approximation based on the small cantilever amplitude, namely $\sin\beta = \beta$. Next, we assume for simplicity that the angle the moment makes with the \hat{y} axis is $\pi/2$. With this last assumption, Eq. 4.4 becomes

$$\cos\angle(\vec{\mu}, \mathbf{H}) = \cos\beta\cos\theta. \quad (4.5)$$

This assumption also allows us to use $\xi + \theta = \pi/2$ to write $\sin^2\xi = 1 - \sin^2\theta$. The energy density of Eq. 4.3 then reduces to

$$\frac{E}{V} = K_{\hat{x}}(1 - \sin^2\theta) + K_{\hat{y}} + K_{\hat{z}}\sin^2\theta - M_s H \cos\beta\cos\theta. \quad (4.6)$$

We then minimize this energy density with respect to θ :

$$\frac{\partial E}{\partial\theta} = 0 = 2(K_{\hat{z}} - K_{\hat{x}})\sin\theta\cos\theta + M_s H \cos\beta\sin\theta. \quad (4.7)$$

Accordingly,

$$\cos\theta = -\frac{\mu H \cos\beta}{2(K_{\hat{z}} - K_{\hat{x}})} = -\frac{H \cos\beta}{H_{K_{(\hat{z}, \hat{x})}}}, \quad (4.8)$$

where we define⁴ $H_{K_{(\hat{z}, \hat{x})}} \equiv 2(K_{\hat{z}} - K_{\hat{x}})/M_s$. Then by our small deflection angle approximation we have

$$\cos\theta = -\frac{H}{H_{K_{(\hat{z}, \hat{x})}}}. \quad (4.9)$$

⁴Note that this parameter is inherently positive.

The next simple assumption we make is that only the \hat{x} component of the torque affects the lower cantilever mode of our oscillators. We have $\tau_x = \mu_y H_z - \mu_z H_y$. Invoking our small angle approximation and assumption that $\tilde{\mu} \perp \hat{y}$ leads us to

$$\tau_x = -\mu_z H_y = -\mu H_o \frac{H_o \beta}{H_{K(\hat{z}, \hat{x})}}. \quad (4.10)$$

Next, we assume that the change in the spring constant of the oscillator can be directly related to the restoring torque, namely

$$\Delta k = \frac{\tau_x}{\beta L_{eff}^2}, \quad (4.11)$$

where L_{eff} is the effective length of the oscillator⁵. Taylor expansion then leads to the approximation that $\Delta\omega_{osc}/\omega_{osc} = \Delta k_{osc}/2k_{osc}$, from which our result for the normalized resonance frequency shift due to an applied field $|\mathbf{H}_o|$ follows directly:

$$\frac{\Delta\omega_{osc}}{\omega_{osc}} = \frac{\mu H_o^2}{2k_{osc} L_{eff}^2} \left(\frac{1}{H_{K(\hat{z}, \hat{x})}} \right). \quad (4.12)$$

Figure 4.7 shows the normalized frequency shift for oscillator A with a least squares fit to Eq. (4.12). The fit yields $H_{K(\hat{z}, \hat{x})}^{-1} = -3.7 \text{ T}^{-1}$, where we have taken the value of μ to be the magnetic moment obtained from the high-field fit ($7.1 \times 10^{-11} \text{ J/T}$). The sign and magnitude of the composite anisotropy field factor shows the preference of the moment to lie in the plane of the film.

⁵For the lower cantilever mode, $L_{eff} = 1.378L$, where L is the actual length of the cantilever [54].

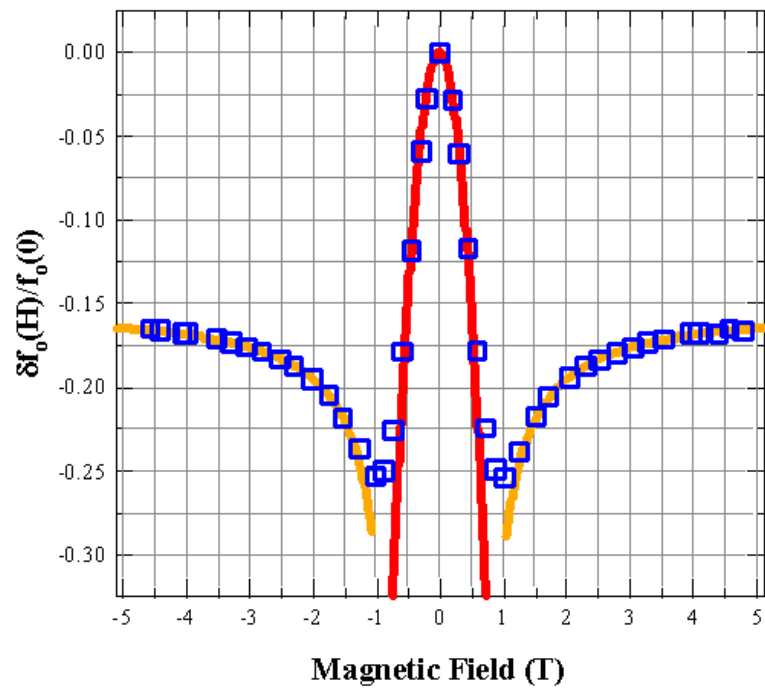


Figure 4.7: Fits to 1/8th head magnet using the low field model is shown in red. The fit to the high field model is shown for completeness in gold.

The transition between regimes is marked by a sharp minimum that reflects the energy necessary to overcome the shape anisotropy of the thin films. For our films, with similar thickness and length, this energy scales with the volume of the micro-magnets; the minima correspondingly shift with volume. The volume ratios $V_A : V_B : V_C$ are 1 : 2.3 : 7.5. This is in good agreement with the observed minima; the transition point for oscillator A is approximately 1.0 T, and that for oscillator B is around 2.3 T, while no transition is detected for oscillator C for field strengths below 5.0 T. These transition points correspond well with the H_s values from the fit of the high-field data to Eq. (4.2). One of the comments from the referee of the paper that resulted from this work [60] suggested that the effect could be flux dependent, meaning that it could be the area of the magnets that is important rather than the volume. Either way, the prospects are very good for the future of magnet-on-oscillator NMR-FM because the effects described, though not malignant, will diminish as progress is made toward smaller and smaller magnets.

4.4 Notes

One thing we observed but are unable to explain at this time is the qualitative difference in the shapes of the normalized frequency versus external field curves. For low fields, oscillators A and B both have a concave down shape, while the field dependence of oscillator C is concave up. The most obvious difference, which may or may not be responsible for this discrepancy, is that, due to the length:width ratio of the magnet, A and B both have a strong

in-plane shape anisotropy while that of C is weaker. This shape anisotropy confines the moments of oscillators A and B to being roughly perpendicular to both \mathbf{H}_0 and the oscillator axis, while for C, the moment is only restricted to being in the plane of the oscillator. Thus the in-plane direction of the moment of oscillator C can no longer be determined strictly from shape considerations.

After concluding this experiment, it was determined that the oscillators were located just outside of the homogeneous field of the HFM. The field gradient that was thus present at the oscillator's position is the most likely culprit behind the dynamic equilibrium position. The probe has been altered so that subsequent experiments find the oscillators safely in the homogenous field. One such experiment that has been performed (this same experiment with different oscillator/magnet configurations) showed the fringes to be stable during field increments, but, thankfully, also showed the oscillator characteristics shifted in a manner similar to that presented in this work.

4.5 Conclusions with Application to NMR-FM

The shift in resonance frequency of single-crystal-silicon oscillators with magnetic films of various sizes has been observed to exhibit two regimes of response to a perpendicular external field at room temperature. The low-field regime is characterized by a sharp decrease in resonant frequency with applied field, in agreement with our simple anisotropy model. The increase in resonant frequency for high fields is consistent with previous results. The transition point between regimes scales with the volume (or area) of the magnets. Similar

behavior is observed for the quality factor of the oscillators.

This work suggests magnet-on-oscillator NMR-FM experiments can be performed in the perpendicular configuration without significant sensitivity degradation. Recall the minimum detectable force equation

$$F_{min} = \sqrt{\frac{4k_B k_{osc} T \Delta\nu}{Q\omega_{osc}}}. \quad (4.13)$$

Assuming the spring constant of the oscillator is constant, then the sensitivity is proportional to $(Q\omega_{osc})^{-1/2}$. If we take the worst case scenario from our data, $f_{osc} \rightarrow 0.7f_{osc}$ and $Q \rightarrow 0.4Q$, then $F_{min} \rightarrow F_{min}/\sqrt{0.28} = 1.9F_{min}$. A factor of two is insignificant with single-shot signal-to-noise ratios greater than 10. It is also comforting that the magnets to be used in future experiments are smaller by several orders of magnitude from those studied here.

Chapter 5

Demonstration of Magnet-on-Oscillator NMR-FM

“I am not discouraged because every wrong attempt discarded in another step forward.”

- Thomas Alva Edison

In this chapter we describe the first magnet-on-oscillator NMR-FM study performed in our lab. The sample was a “semi-infinite” slab of ammonium sulfate. The sample is “semi-infinite” because its dimensions are several orders of magnitude larger than those of the gradient-producing magnet with which it interacts. A SNR ~ 4 was detected, and is in good agreement with what was expected. Other work, mostly theoretical, has been published on the semi-infinite slab [61, 62].

5.1 Experiment Overview

These experiments were performed in the magnet-on-oscillator setup, illustrated in Fig. 5.1. In this configuration, the sample approaches the gradient-producing magnet so that the gradient has the opposite sign from all of our

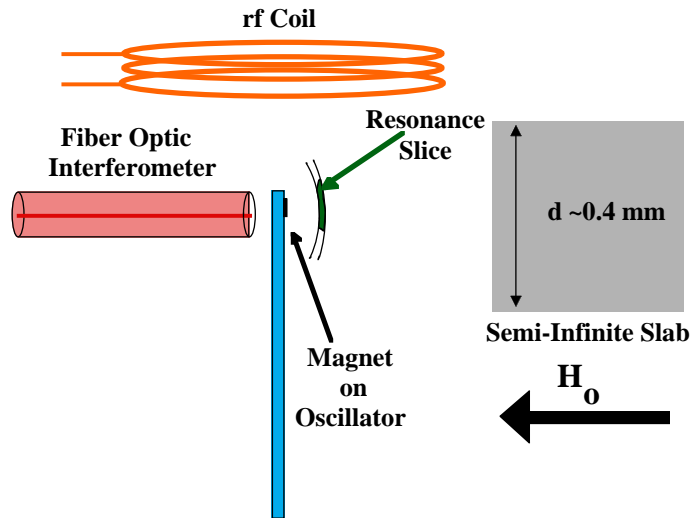


Figure 5.1: Schematic overview of magnet-on-oscillator experimental setup to study the semi-infinite slab. Note that the external field is pointing in the opposite direction from our other NMR-FM studies.

sample-on-oscillator experiments. The result of the relative sign change manifests itself as a decrease of the oscillator’s amplitude during CAI cycles because the signal artifact is out of phase with the NMR force. This is more of an annoyance than a problem.

During the experiment, the sample was held by a tube piezo that was mounted onto the \hat{z} positioner stage (known as the “magnet stage” for the previous sample-on-oscillator experiments). This gave us fine positioning controlled by the voltage on the tube piezo, and coarse position controlled via external positioning rods. The oscillators used were produced by Michelle Chabot at NIST with a process that integrates the magnet deposition with lithography and fabrication [63]. The magnets were 4 μm diameter Permalloy

($M_s = 650$ kA/m) cylinders that were 180 nm thick. The resonance frequency of the oscillators were measured to be ~ 4000 Hz, the pressure-limited quality factors were ~ 1600 , and the spring constant was measured¹ to be $\sim 4 \times 10^{-4}$ N/m. The resulting room-temperature force sensitivity using a lock-in bandwidth of $\Delta\nu = 1/(4 \times 30 \text{ ms}) \approx 8$ Hz was determined using

$$F_{min} = \sqrt{\frac{4k_{osc} k_B T \Delta\nu}{\omega_{osc} Q}}, \quad (5.1)$$

to be 5.8×10^{-16} N. The force expected from a resonance slice completely immersed in the sample was determined via Curie's Law and the discussion of §1.3.2 to be 7.6×10^{-16} N using

$$F_{expected} = n \frac{(\gamma \hbar)^2}{4 k_B T} H_{total} \frac{2\Omega A}{\gamma}, \quad (5.2)$$

where the area of the slice was estimated from the diameter of the magnet to be $A = \pi (4 \mu\text{m})^2/4$, and the FM amplitude Ω was $2\pi \times 50$ kHz. The expected signal-to-noise ratio of 1.3 was thus smaller than we would have liked, so the data were averaged N times² to increase the SNR by \sqrt{N} .

5.2 Magnets on Oscillators

The gradient-producing magnets on the mechanical oscillators were Permalloy cylinders. The diameters of the magnets produced varied from

¹From its geometry, the expected spring constant was $\sim 2 \times 10^{-4}$ N/m, where we used $k_{osc} = Et^3w/4l$, taking $E = 10^{11}$ N/m², $t = 250$ nm, $w = 3 \mu\text{m}$, and $l = 180 \mu\text{m}$.

²N was usually 4... run-specific details below.

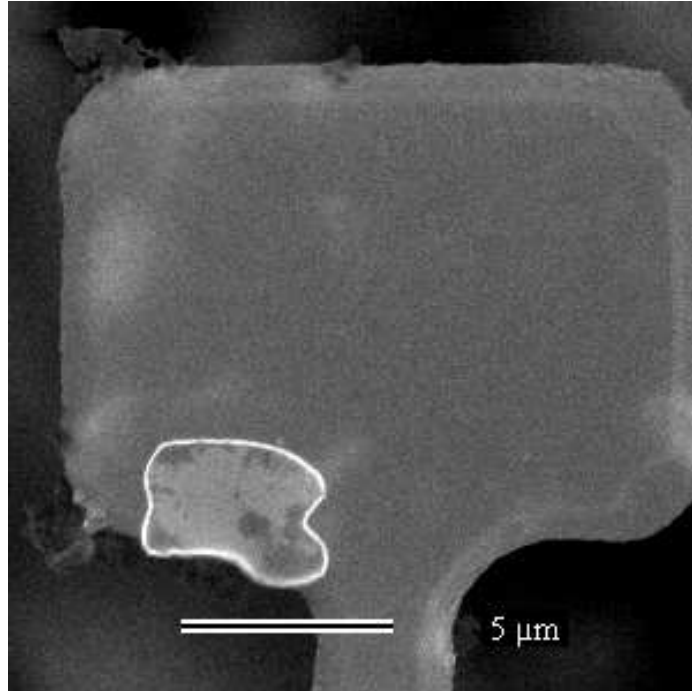


Figure 5.2: SEM showing the irregular geometry of 370 nm thick cylinders on the head of an oscillator. These thick magnets are deformed during the lift-off stage of the fabrication; thinner magnets are more uniform.

3 μm to 5 μm , and the thicknesses were 170 nm, 180 nm, and 370 nm. Ideally, the 370 nm magnets would have been used to push a given field gradient farther from the magnet. These magnets, as depicted in Fig. 5.2, did not have well-defined geometries due to tearing during lift-off, which would have made modelling them difficult. Instead, we chose to use an oscillator whose magnet was actually cylindrical (4 μm in diameter and 180 nm thick) so that we could confidently model its field and gradient.

The \hat{z} component of the magnetic field B from a magnetic cylinder with

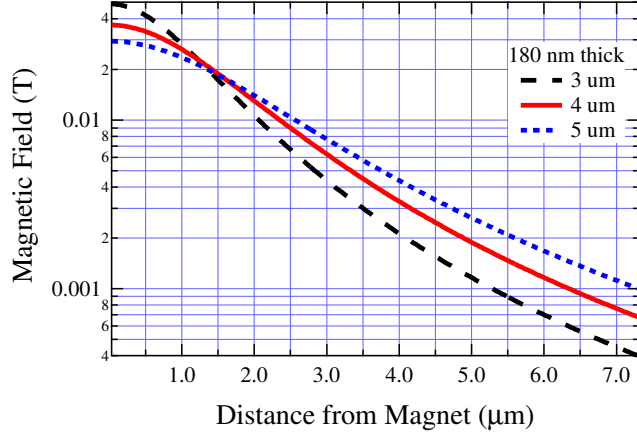


Figure 5.3: Magnetic fields as functions of distance from the magnet along the axis of 180 nm thick cylindrical Permalloy magnets modelled using Eq. 5.3.

saturation magnetization M_s , length L , radius r , at a distance z along its axis is given by

$$B_z(z) = 4\pi M_s \left(\frac{z}{2\sqrt{z^2 + r^2}} - \frac{z - L}{2\sqrt{(d - L)^2 + r^2}} \right). \quad (5.3)$$

This is a general formula that does not make assumptions of the aspect ratio L/r of the magnet. Its derivative with respect to z shows that the field gradient along the axis is given by

$$\nabla_z B_z(z) = \frac{-4\pi M_s \left(\frac{r}{L}\right)^2 / 2L}{\left[\left(\frac{r}{L}\right)^2 + \left(\frac{r}{L} - \frac{1}{2}\right)^2\right]^{3/2} - \left[\left(\frac{r}{L}\right)^2 + \left(\frac{r}{L} + \frac{1}{2}\right)^2\right]^{3/2}}. \quad (5.4)$$

Figures 5.3 and 5.4 show the results of these models for the 180 nm thick cylindrical Permalloy magnets that have been deposited on mechanical oscillators. The oscillator type used in these experiments is shown in Fig. 5.5, and a zoom in showing the magnet and the oscillator thickness is shown in Fig. 5.6.

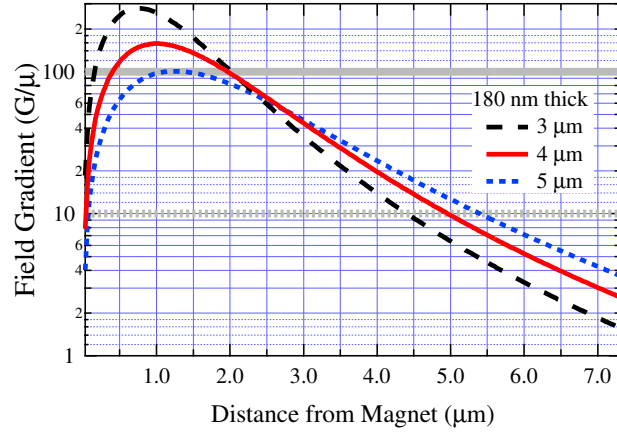


Figure 5.4: Magnetic field gradients as functions of distance from the magnet along the axis of 180 nm thick cylindrical Permalloy magnets modelled using Eq. 5.3. The solid and dotted straight lines indicate resonance slice thicknesses of 100 nm and 1000 nm taking the FM amplitude $\Omega/2\pi = 50$ kHz.

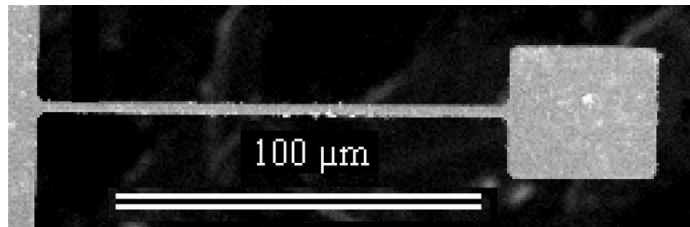


Figure 5.5: SEM of the oscillator type used to study the semi-infinite slab. The gradient-producing magnet is the small white spot in the middle of the head. The neck width and length are $3.00 \mu\text{m}$ and $130.0 \mu\text{m}$, the head is $30.0 \mu\text{m} \times 40.0 \mu\text{m}$, and the thickness is about 250 nm.

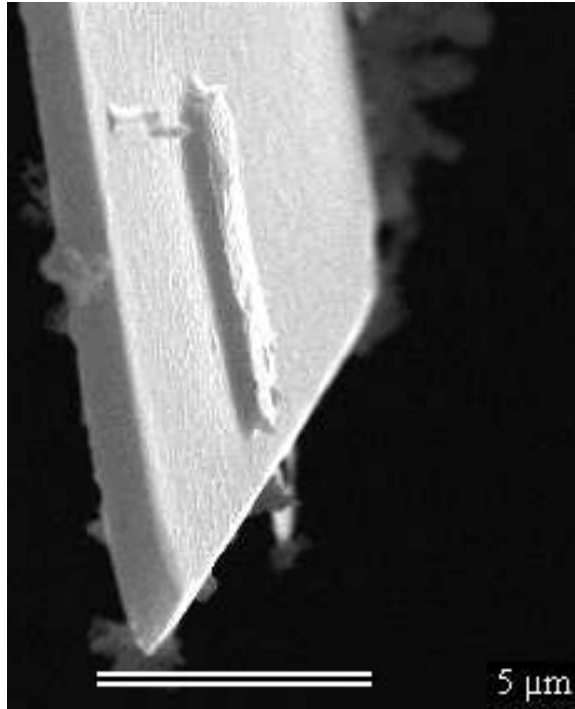


Figure 5.6: Angled SEM of the oscillator type used to study the semi-infinite slab showing the thickness of the oscillator and the magnet. The cylindrical gradient-producing magnet shown is 180 nm thick and $\sim 5 \mu\text{m}$ in diameter. Working backward from the known tilt angle of the SEM and the bevel of the oscillator reveals a thickness of about 250 nm.

5.3 Sample Preparation

The semi-infinite slab sample was prepared from granular ammonium sulfate, $(\text{NH}_4)_2\text{SO}_4$. We chose ammonium sulfate as our sample for this demonstration experiment because its spin-lattice relaxation time is long (~ 5 s), its proton density is large (6.4×10^{22} $^1\text{H}/\text{cm}^3$), and it is easily cleaved to yield a flat vacuum-sample interface. Once a satisfactory crystal is cleaved, the sample is glued to a graphite rod and aligned with the fiber and sample.

5.3.1 Crystal Selection

To select a sample, the following procedure was followed. A small number of grains were placed in a weighing boat. Separate from this, dirty double-sided tape was placed in the bottom of another weighing boat. The grains were inspected using the telescoping microscope to choose grains with good initial characteristics. Attractive grains are relatively small, right parallelepipeds with length-to-width-to-height ratios of roughly 4:3:1, have a rough yet finished sheen, and have few internal voids. Voids and other defects are most easily observed by blocking the light from the lamp with the tip of a scalpel (the direct light washes out the light reflected from the defects). Once a grain was chosen, it was placed very near the edge of the double-sided tape so that it could be easily removed if the cleave went well. Samples were initially placed in the middle of the tape, but it was soon found that even the dirtiest tape was still so sticky that the sample was nearly impossible to remove without either crushing it or having the cleave end up face down and thus covered

with dirt.

Cleaving the $(\text{NH}_4)_2\text{SO}_4$ grains was straightforward. A clean straight-edged scalpel was used to cleave the samples along their length. If the sample was too long, it was cut down to size along the width before being cleaved. The tip of the scalpel was secured in the base of the weighing boat, and a chopping motion was used to touch blade to the crystals. This was done in order to get several cleaves per crystal, which is necessary because although the $(\text{NH}_4)_2\text{SO}_4$ grains cleave fairly easily, they do not always form large planar regions. The most useful crystals cleaved easily if the scalpel was pressed lightly against their edges.

After each cleave it was necessary to inspect the region of the cleave to make sure it was planar and free of defects and particles. The stickiness of the tape was useful at this point because the sample could be tilted while being held in place. Samples that were chosen for mounting looked uniform in the center of the crystal, while unacceptable samples had obsidian-like ring shaped fractures. Because these samples were supposed to represent semi-infinite slabs, the crystals chosen were roughly cubic with 300 – 500 μm sides.

5.3.2 Sample Mounting

A 0.5 mm graphite rod (pencil lead) served as our sample holder. This sample holder was chosen for its availability, rigidity, and conductivity. The setup for mounting the crystal onto the rod is depicted in Fig. 5.7. The crystal was picked up with one tine of a pair of tweezers, presumably attached

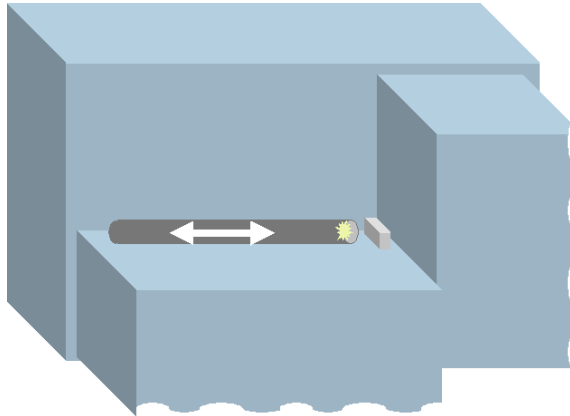


Figure 5.7: Setup for sample mounting using a graphite rod and three microscope slides. The slides only allow the rod to move in one direction and hold the crystal steady during mounting.

by an electrostatic interaction, and placed in the corner made by three glass microscope slides. The graphite rod was then placed along two of the slide-walls so that it could only move in the direction perpendicular to the third wall (and thus the plane of the crystal). The crystals were mounted on the graphite rod using Torr-Seal epoxy. The epoxy was mixed for one minute, then using a single strand of wire from a braided cable, a small drop of epoxy was transferred to the tip of the graphite rod and smeared around. The graphite rod was then pushed up against the back of the crystal, and the excess epoxy was smeared around the crystal-graphite interface. This alignment procedure was done in its entirety under the stereoscope. The epoxy was cured by placing a 60 W lamp about 1 inch above the setup for at least two hours.

A fitted aluminum insert was pressure-fit into the grounded inner electrode of a tube piezo by placing a $2\text{ mm} \times 1\text{ mm}$ strip of aluminum foil between

it and the piezo. The graphite rod was inserted into a fitted through-hole in the aluminum insert until the crystal was 5 mm from the insert. The end of the hole was slightly deformed so that it scratched the graphite rod as it passed this point; this serves to hold the rod in place and to establish an electrical contact that grounds the rod. The sample was then approached within about 50 μm of the oscillator. The height and three angle-controlling screws of the scanner stage were adjusted so that the normals to the oscillator and the vacuum-sample interface were as parallel as possible. The alignment is critical because the relative angle between the oscillator and the sample must be less than $\sim 5^\circ$ in order for the resonance slice to enter the sample³. §5.4.1 below demonstrates that the alignment was good enough that at distances of $\sim 50 \mu\text{m}$ or more the laser light could reflect off the sample back into the 5 μm diameter fiber core; the alignment error thus less than 5/100.

5.4 Experimental Difficulties

We ran into several unexpected difficulties while trying to perform our first magnet-on-oscillator experiment. Our trials and tribulations are noted here.

³The magnet was $\sim 20 \mu\text{m}$ from the top of the oscillator, and the useful gradients are found at $\sim 2 \mu\text{m}$; $\theta_{\text{misalign}} \sim 2/20$.

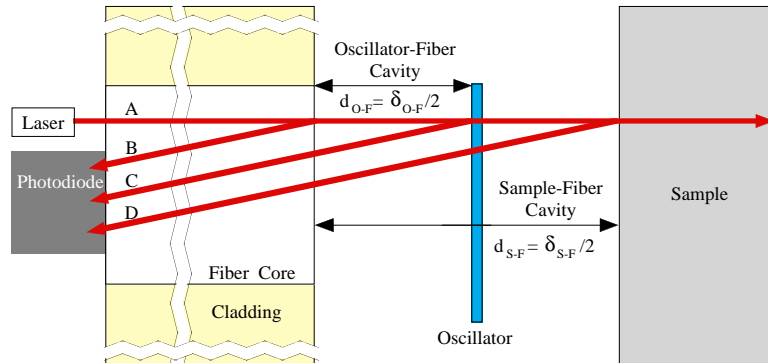


Figure 5.8: Artist’s rendition of the double interferometer. In the normal interferometer, reflected waves B and C interfere. The double interference is observed when the light reflected from the sample-vacuum interface (wave D) enters the fiber and interferes with the normal interference pattern.

5.4.1 Sample-Mediated Double Interference

Our initial experimental setup was naively exactly that depicted in Fig. 5.1, where the fiber is pointed at the head of the oscillator, which is close to the sample. Some of the incident laser light transmits through the ~ 250 nm thick oscillator and eventually strikes the sample. Because the sample has been aligned with the oscillator so that their normals are nearly parallel, the light that hits the sample reflects back through the oscillator into the fiber where it establishes a second interferometer with the light that is internally reflected from the fiber-air interface. This results in two coupled interferometers as the intensity of the light at the photodiode can be independently modulated by both the fiber-oscillator distance and the fiber-sample distance. Figure 5.8 schematically illustrates the “double interferometer”.

As an aside, the reader should note that there are actually three in-

terferometers; they can be identified by their path length differences, namely oscillator-fiber, sample-fiber, and sample-oscillator. Practically speaking, however, there are only two interferometers because, for instance, the path length differences of the sample-fiber cavity and the oscillator-fiber cavity are always changed in synchrony when the oscillator-fiber distance is changed. A similar argument applies if the sample-oscillator cavity is changed. If we could move all three elements independently, the third interferometer would reveal itself.

The quality of the interference pattern was strongly dependent on whether the fiber-oscillator distance or the fiber-sample distance was changed. The former gave normal high quality patterns, while the latter produced abnormal interference patterns. Three examples of each interference pattern are depicted in Fig. 5.9. The initial conditions (at 0 V) were prepared by changing the constant distance to maximize the DC level, maximize the slope, and to minimize the DC level for the top, middle, and bottom curves in the figure. For instance, for the top curve of the left graph, the sample-fiber distance was changed to maximize the interference pattern for the initial oscillator-fiber distance, then it was held constant as the oscillator-fiber distance was changed. The double interferometer was shown via modelling using only first order reflections to yield normal patterns by changing either distance. We conclude that the erratic behavior of the sample-mediated interference pattern of Fig. 5.9 is due to multiple reflections within the fiber-oscillator cavity.

While the discovery of the double interferometer is interesting, it is detrimental to our experiment because it makes the validity of the traditional

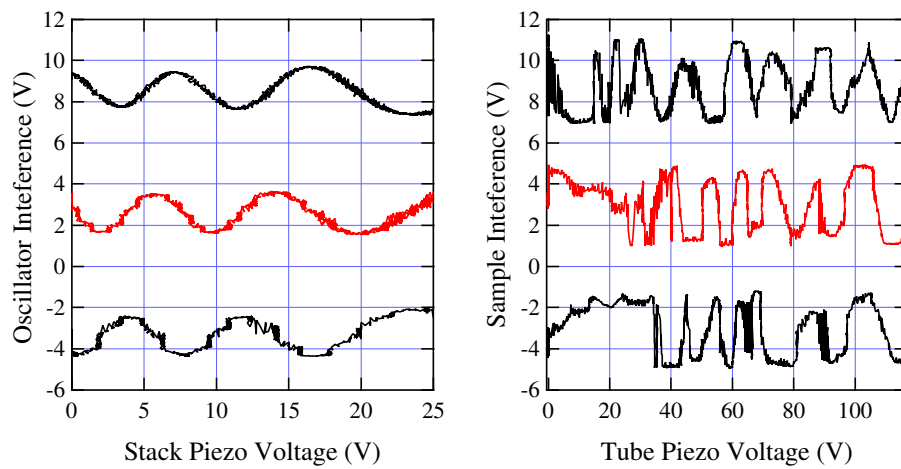


Figure 5.9: Interference patterns formed by changing the oscillator-fiber distance (left), and the sample-fiber distance. The left axis scale applies directly for only the red middle curve on each plot; the others were offset for clarity. The top curves have their initial DC level at the maximum of the pattern, the middle curves begin at the middle of the fringe (where we would normally lock with feedback), and the lower curves begin at the minimum DC level.

conversion interferometer light intensity to oscillator displacement questionable. If the sample is far from the fiber ($\sim 50 \mu\text{m}$), the sample-mediated interference pattern is small, if noticeable at all. As the sample is brought closer to the oscillator, its effect increases to the point that the sample-mediated pattern has an amplitude equal to that of the oscillator-mediated pattern. In a normal interferometer, the conversion from intensity to deflection amplitude is straightforward (see §2.1.4). The dependence of the intensity on the sample-mediated interferometer undesirably changes the conversion ratio. We have chosen to postpone further analysis of this phenomenon at this time. In order to avoid the double interference, we raised the sample about $100 \mu\text{m}$ so that only the head of the oscillator can contact it, and lowered the fiber so that the laser is incident half way down the oscillator on its $3 \mu\text{m}$ neck. The resulting setup is depicted in Fig. 5.10.

5.4.2 Position Dependence of the Artifact

With the double interference problem alleviated, the experiment went forward. The sample was initially placed as close to the oscillator as it could be as viewed using the adjustable microscope on the lab bench, then retracted by approximately $100 \mu\text{m}$. The oscillators were then moved laterally so that the last oscillator on the chip was $\sim 100 \mu\text{m}$ away from the laser light from the fiber; this is a preventative measure against fiber-oscillator collisions during can mounting and probe insertion. The can was placed on the probe, it was pumped down to about 10^{-4} Torr, then placed into the 8.073 T NMR magnet.

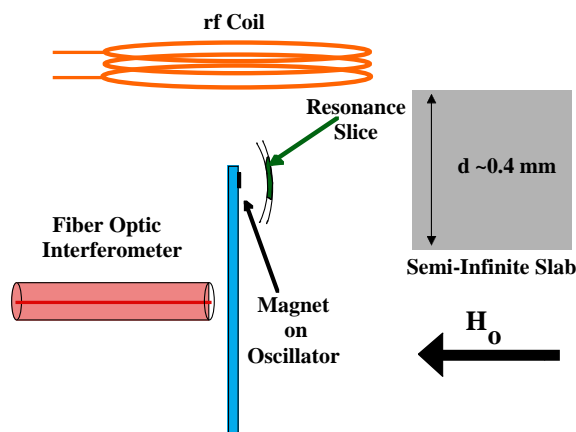


Figure 5.10: Experimental setup used to study the semi-infinite plane. The fiber was lowered and the sample was raised to avoid the double interference effect, though the latter is not evident in this picture.

The sample was then brought forward in $\sim 6 \mu\text{m}$ coarse steps with $+117 \text{ V}$ initially on all four quadrants of the tube piezo so that it was fully retracted. After each coarse step, the tube-piezo voltage was decreased to zero to make a fine approach of up to $3 \mu\text{m}$. Before advancing coarsely again, the electrodes of the piezo were grounded so that the hysteresis was repeatable (see §2.3), and the applied voltage was increased to $+117 \text{ V}$ to retract the piezo.

At each coarse and fine position, a cyclic adiabatic inversion (CAI) cycle was performed to search for an NMR signal for five different carrier frequencies. The resulting data is shown in Figs. 5.11 and 5.12. These data appear to be what we are looking for at first glance, but further scrutiny proves otherwise. Because the expected signal is out of phase with the artifact we expect the force from NMR to decrease the oscillator's amplitude during a

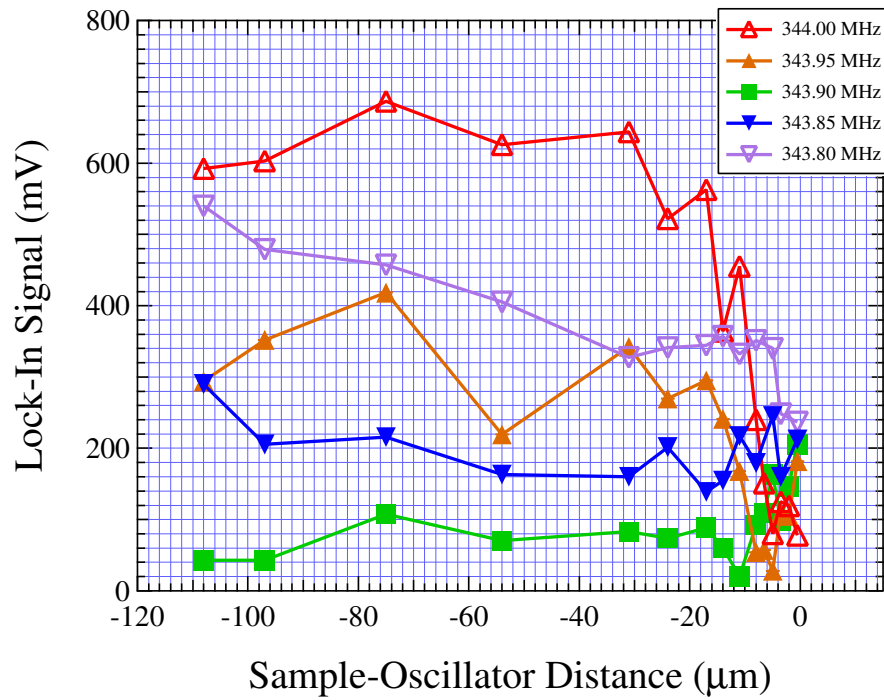


Figure 5.11: Oscillator deflection amplitude during CAI cycle for five different frequencies for different sample positions. The initial position was chosen to be the reference position. Error bars are withheld for the sake of clarity, but are on the order of 80 mV.

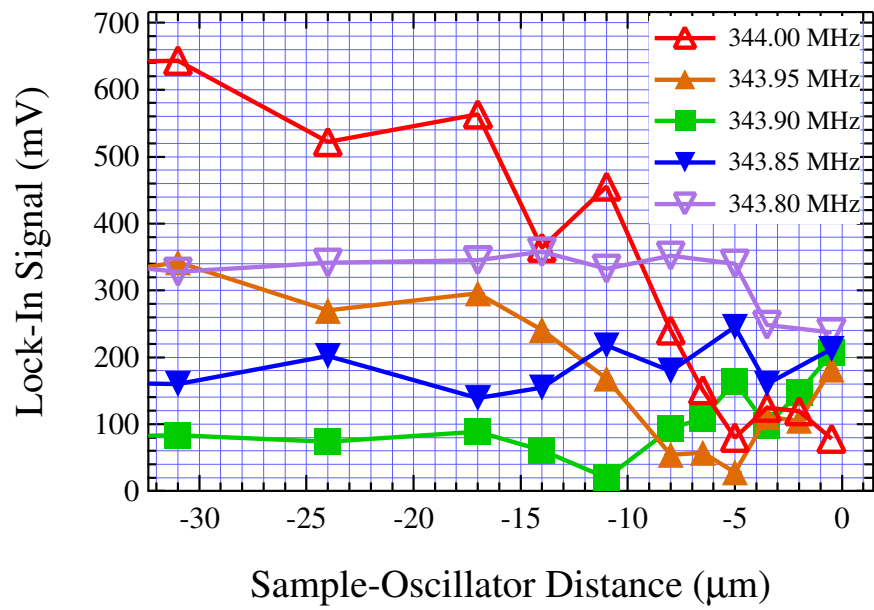


Figure 5.12: Zoom of the interesting region of Fig. 5.11. Oscillator deflection amplitude during CAdI cycle for five different frequencies for different sample positions. Error bars are withheld for the sake of clarity, but are on the order of 80 mV. The reference distance (0) was taken to be the point at which the sample touched the oscillator.

CAdI cycle. This clearly appears to happen in our data. However, the length scales on which the transition happens are roughly an order of magnitude too large. The resonance slice thicknesses for these frequencies are all in the range $0.5 \mu\text{m}$ to $1.4 \mu\text{m}$. The transition shown in the data occurs over about $20 \mu\text{m}$. The obvious conclusion is that something other than (or more likely, in addition to) NMR is changing the oscillator's spurious amplitude. We thus believe the data of Figs. 5.11 and 5.12 are dominated by a position-dependent artifact unrelated to NMR.

In addition to the CAdI cycles, we also performed frequency scans at each position to monitor the resonance frequency of the cantilever over time. The resonance frequency of 4004.7 Hz and quality factor of ~ 1600 of the oscillator remained constant throughout the experiment. However, as shown in Fig. 5.13, the response of the cantilever to an assumedly constant driving voltage of 10 mV was not constant. The response amplitude increases as the sample-oscillator distance is decreased. One might expect the opposite of this if there were some sort of long-range interaction (e.g., electrostatic), but in that case the response would decrease because of an interaction magnitude-dependent decrease in the quality factor. The source of this position-dependent response has not been determined, and its presence may require an additional calibration correction for each position.

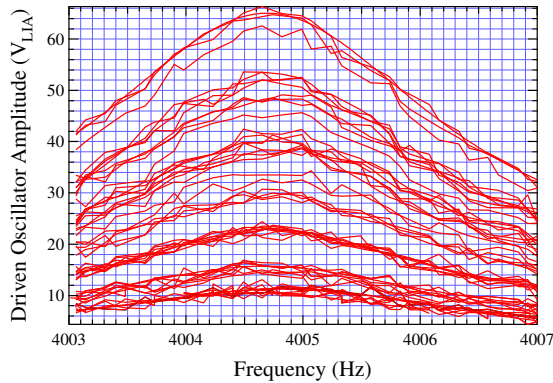


Figure 5.13: Oscillator response to a constant driving force for different sample-oscillator distances. The lowest amplitude group of curves correspond to the distances below the transition ($< \sim -20 \mu\text{m}$), and the largest amplitude group corresponds to the closest approach ($\sim 0 \mu\text{m}$). The origin of this amplified response is unknown.

5.4.3 Tuning Dependence of the Artifact

As the astute reader noted, the artifact strength in the preceding section was a strong function of the detuning of the carrier frequency from the tank circuit's resonance frequency. This was noted previously for the ideal artifact in §2.5.4, but that study implied that there was a region of roughly 3 MHz centered at the tuned frequency where the artifact was minimized. The artifact for the +0.1 MHz detuned carrier was an order of magnitude larger than that of the tuned carrier (see Fig. 5.11). This led us to investigate this phenomenon further.

Figure 5.14 shows the observed oscillator amplitudes during CAdI cycles for two different tunings of the tank circuit as functions of the carrier frequency for an RF power of +26.1 dBm. The carrier frequencies used were

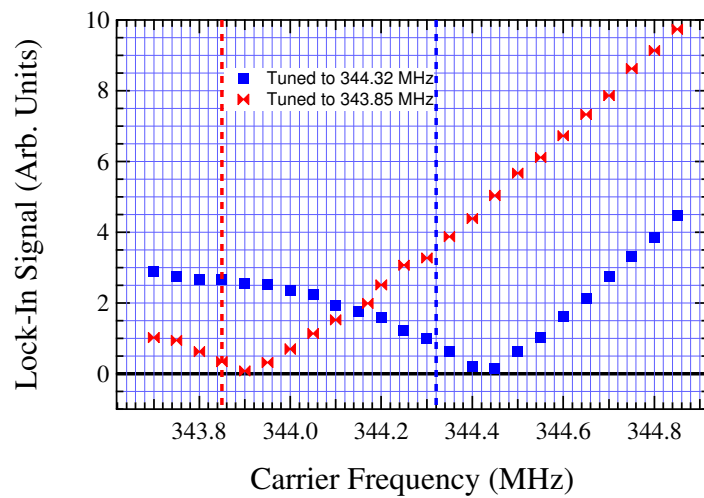


Figure 5.14: Magnitude of signal artifact as a function of carrier frequency for two different tunings of the tank circuit. The two vertical dashed lines indicate the frequencies that were tuned using the Smith Chart function of a network analyzer. The difference between the tuned frequency and the frequency of minimum artifact may illustrate the systematic error in tuning (~ 3 parts in 10,000).

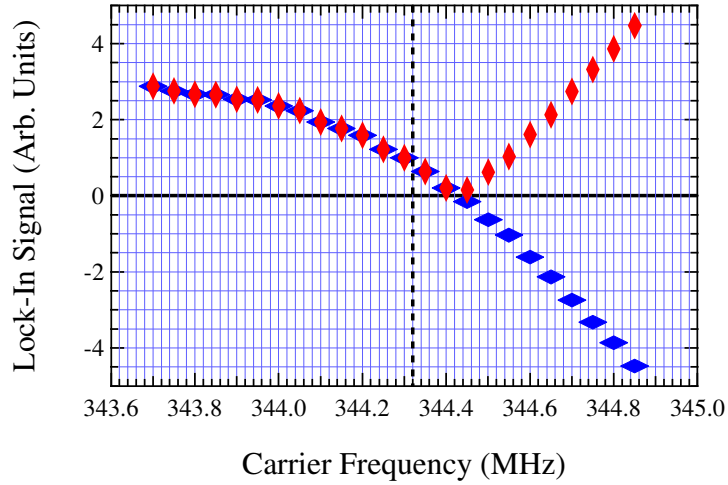


Figure 5.15: Magnitude of signal artifact as a function of carrier frequency taking phase into consideration. The vertical diamonds are the same data as shown in Fig. 5.14. The minimum magnitude of the artifact corresponds to a sign change in the phase of the signal, which we believe corresponds to the resonance frequency of the tank circuit.

in the range from 343.70 MHz to 344.85 MHz, separated by 0.05 MHz. The sample was retracted $\sim 100 \mu\text{m}$ from the oscillator to the region where the artifact was observed to be position-independent prior to taking the data.

We believe that the minimum artifact level occurs at the resonance frequency of the tank circuit, but the observed minima appear to occur above the tuned frequency. This discrepancy is most likely the realization of systematic errors associated with tuning the tank circuit. If we take the phase of the artifact signal into consideration, as in Fig. 5.15, then we realize that the minimum artifact level corresponds to a sign change of the phase of the signal. This supports our belief that the minimum occurs at the resonance frequency

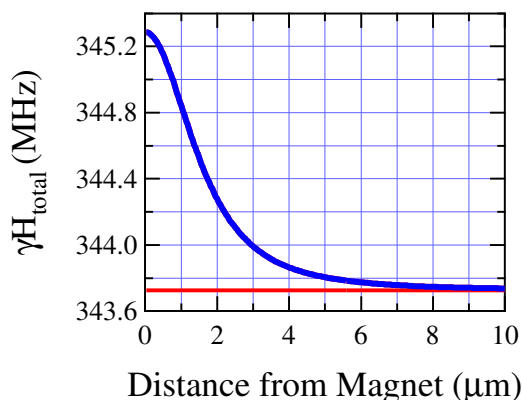


Figure 5.16: Proton resonance frequency as a function of distance from the 4 μm diameter, 180 nm thick Permalloy magnet. The red horizontal line at 343.72 MHz is γH_o .

of the tank circuit.

5.5 Carrier Frequency Scan

After encountering the long-range position dependence of the artifact, we decided to search for an NMR signal by changing the carrier frequency of the RF. This method of scanning has always seemed to be the favorite method of the other MRFM groups that have performed magnet-on-oscillator MRFM...we suppose we now know why. Because the sample-oscillator position is fixed in this sort of experiment, changes to the artifact level are due to either the relative tuning of the tank circuit or NMR; no other effects have been discovered (yet) that alter the artifact level.

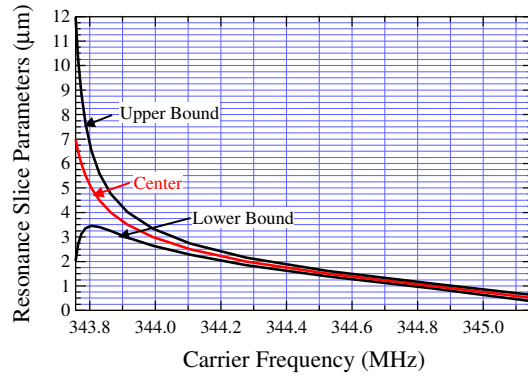


Figure 5.17: Resonance slice center and bounds as a function of the carrier frequency. The slice thickness is determined by the distance between the upper and lower bound curves. The bound curves were calculated using an FM amplitude of 50 kHz.

5.5.1 Sub-Micron Resonance Slices

Figure 5.16 shows the resonance frequencies of protons as a function of distance from the magnet to the center of the resonance slice. The center position of the resonance slice can be swept by changing the carrier frequency to match the resonance frequency at the desired position; doing so for several frequencies constitutes a scanning experiment. Additionally, because the field gradient is a strong function of distance (see Fig. 5.4, the thickness of the resonance slice becomes a function of the carrier frequency. Figure 5.17 shows the effect of the carrier frequency on the resonance slice. Figure 5.18 explicitly shows the thickness of the resonance slice for an FM amplitude of 50 kHz for relevant frequencies. Note that the slice thickness is less than 500 nm for most of the frequency range, with a minimum thickness of 150 nm at 344.85 MHz.

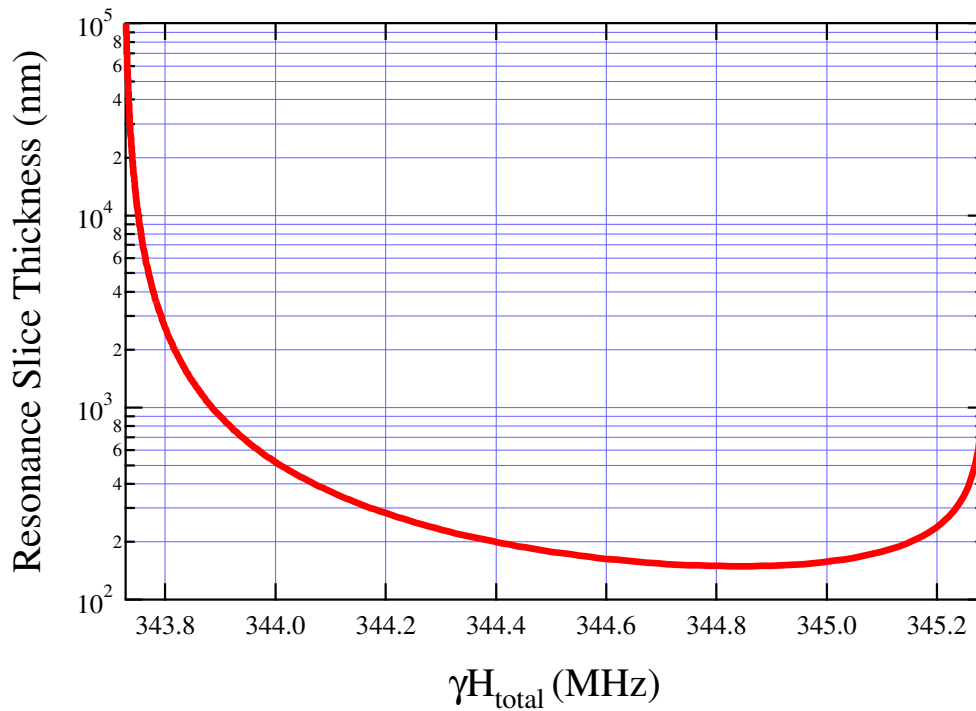


Figure 5.18: Resonance slice thickness for different frequencies. The curve was calculated using an FM amplitude of 50 kHz and the normal equation for the slice thickness Δz . These experiments are our first experiences with sub-micron resonance slices. The thinnest resonance slice is 150 nm and occurs at 344.85 MHz.

5.5.2 The Experiment

The sample was initially positioned about $50\ \mu\text{m}$ from the oscillator, and was approached in $\sim 6\ \mu\text{m}$ steps. Making lemonade from lemons, we observed the response of the mechanical oscillator to the constant driving force as the approach was made. When the oscillator's driven amplitude nearly reached the highest level previously observed (just before the sample touched it in the position scan of above), the approach was stopped. This approach method brought the sample to about $2\ \mu\text{m}$ from the oscillator.

With the sample in position, we began to search for an NMR signal by performing CAdI cycles that were 1.8 s long, embedded in a ~ 2.2 s RF exposure. Using a Rhode and Schwarz signal generator, the initial frequency offset was set to 400 kHz above resonance, and the decay from this level down to resonance had a time constant of 10 ms. The CAdI cycle was initiated 10 ms after the decay to resonance⁴. The FM amplitude $\Omega/2\pi$ was ~ 50 kHz. The pulse programmer was used in its "auto cycle" mode to repeat the decay and CAdI cycle once every 40 s. This long repetition period was chosen because it was about eight times the spin-lattice relaxation rate for ammonium sulfate. The RF power was held constant at 26.1 dBm throughout the experiment, which we estimate yielded an RF field strength of about 5 G. The lock-in had a time constant of 30 ms. The oscillator resonance frequency was 4006.1 Hz and its Q of ~ 1600 was measured from the ring-down when the CAdI cycle

⁴This was a limitation of the pulse programmer time base that was used

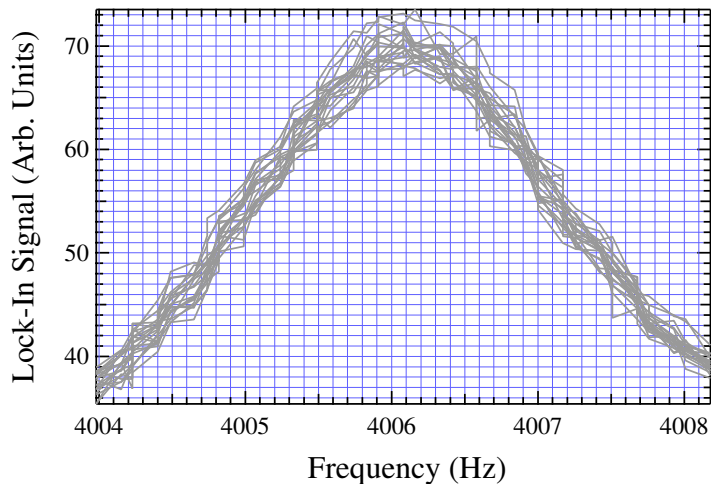


Figure 5.19: Frequency scans of the mechanical oscillator. The scans were taken twice per carrier frequency throughout the experiment.

was terminated. In contrast to the position scan, the oscillator’s response to a constant driving amplitude was quite constant (see Fig. 5.19).

The fringe size was constant throughout the experiment at $0.8 V_{pp}$. In order to convert to oscillator displacement, however, we could not use the normal conversion factor. Instead, we needed to take into consideration that the laser was aimed half way down the oscillator to avoid the double interference, and that we were locking on the side of the fringe that damped the oscillator. To first order, we estimate that the oscillator’s amplitude at the magnet was twice the measured amplitude. In order to correct for the damping, we generated a conversion factor using the Equipartition Theorem to tell us what the room-temperature mean-square displacement of the oscillator due to thermal noise should have been for $k_{osc} = 4 \times 10^{-4}$ N/m.

To perform the scans, the tank circuit was tuned to frequencies f_{tuned} that gave 500 nm separation between each position of the resonance slice. Five carrier frequencies f_c were used for each tuned frequency. Specifically, four carrier frequencies⁵ in addition to the tuned frequency were used while the tank circuit was tuned to f_{tuned} , namely $f_c = f_{tuned} \pm 0.05$ MHz and $f_c = f_{tuned} \pm 0.10$ MHz. For each tuning and carrier frequency, four CAI cycles that were averaged constituted a measurement. Figure 5.20 shows the raw data for all five frequencies. The arbitrary units of the signal are directly proportional to the oscillator’s deflection; Figure 5.21 shows the ring-ups for all $f_c = f_{tuned}$ converted to oscillator amplitude. The transition to lower amplitude ring-ups for each frequency group is due to the NMR force signal.

We present processed data for tuned carrier frequencies $f_c = f_{tuned}$ in Fig. 5.22. In order to generate these data, the RMS value of the signal artifact was subtracted from the total signal, leaving only noise and the negative signal due to NMR. The calculated RMS value of the resultant oscillator displacement was 3.9 nm, and the calculated RMS noise level was 1.0 nm. The observed SNR is thus 3.9. We expected an SNR of 2.6 for $N = 4$ averages and a single-shot SNR of about 1.3 (see §5.1). This discrepancy is most likely due to the conservative estimate of expected force using only the area of the gradient-producing magnet; the field actually intercepts an area larger than the magnet

⁵This was done with the intention of making sure that the artifact was minimized due to tuning—only later did we realize the discrepancy between the “tuned” frequency and the actual minimum of the artifact (see Fig. 5.14).

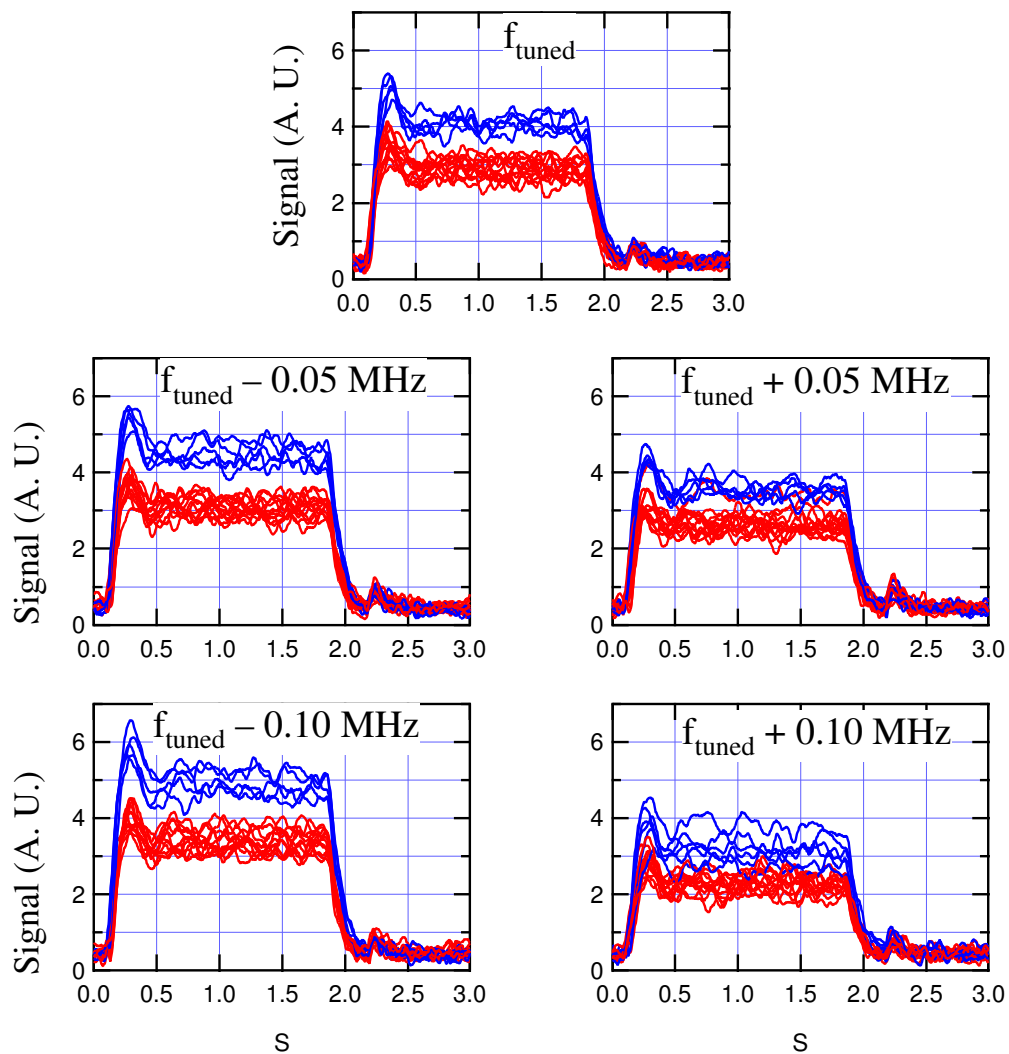


Figure 5.20: Raw data for all five frequency regimes investigated. The larger amplitude blue curves are artifact signals, and the lower amplitude red curves contain both the artifact and the NMR signals; the signal level decreases because the artifact and NMR forces are out of phase. The RF is turned on at $t = 0$ s, and goes off at 2.2 s; the embedded CAdI cycles begin at 70 ms, and end at 1.85 s.

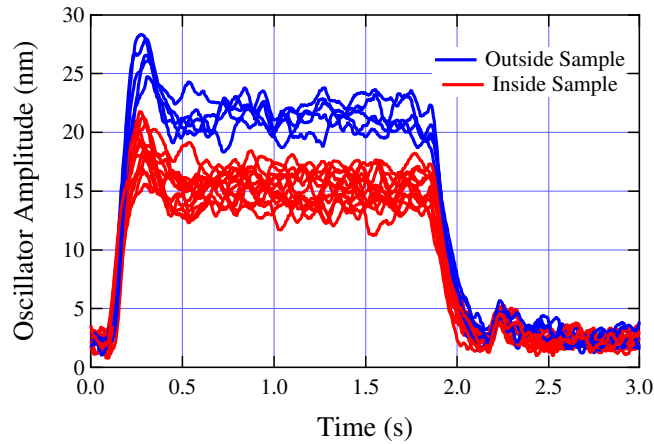


Figure 5.21: Ring-up data during CAdI cycles for $f_c = f_{tuned}$. The larger amplitude blue curves are artifact signals, and the lower amplitude red curves contain both the artifact and the NMR signals; the signal level decreases because the artifact and NMR forces are out of phase.

itself.

The data for the carrier frequencies that were above and below the resonance frequency of the tank circuit show an unexpected, but small, shift in the location of the sample. These data are presented in Fig. 5.23. The origin of this shift is currently unknown. The mechanism may be related to some sort of H_1 effect that is mediated by the apparently extreme sensitivity of the experiment to the tank circuit tuning. This, however, seems unlikely because the quality factor of the resonant circuit is probably no greater than 100, which implies that H_1 should be quite constant over the 200 kHz range we observe. The cause is not obvious.

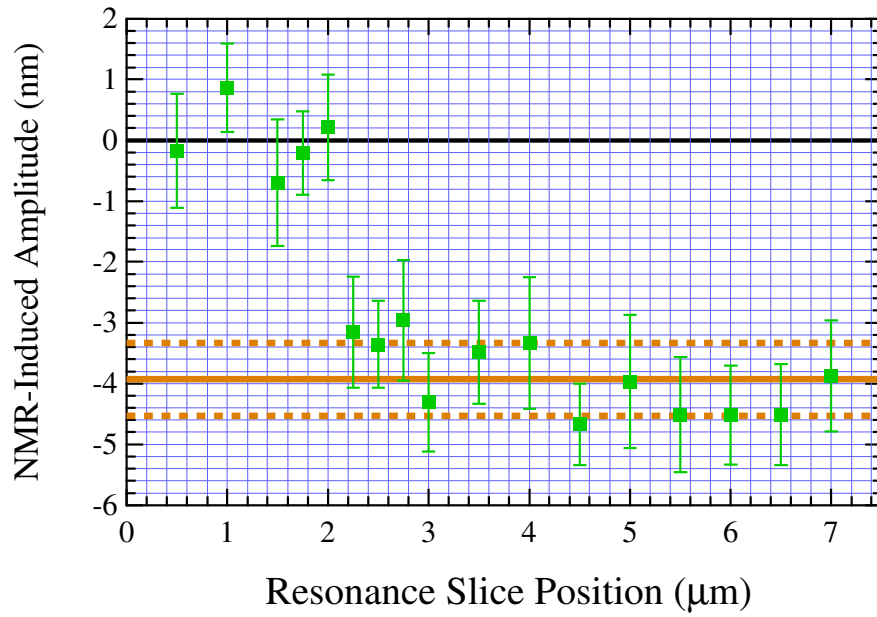


Figure 5.22: NMR signal detected by scanning the carrier frequency to move the resonance slice position. The SNR is about 3.9, which is in accord with the expected improvement with $N = 4$ averages. The solid lines are the means for the artifact level (top) and the NMR signal (bottom) and the dashed lines are one standard deviation from the means. The error bars indicate the standard deviations of the steady-state levels of the ring-ups.

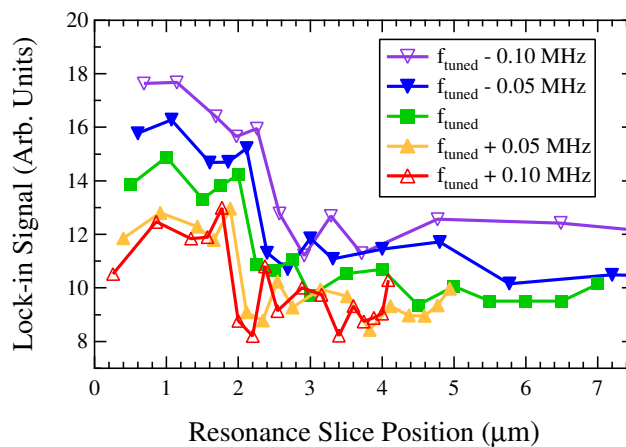


Figure 5.23: Raw data for each of the frequency groups used. The transition at the sample interface is seen for each of the frequencies, but the location of the shift is dependent on the detuning of the carrier frequency from the resonant frequency of the tank circuit. The shift is of unknown origin.

5.5.3 Nutation

Once the NMR signal was detected, we tried to perform spin nutation experiments to calibrate the RF field H_1 so that we could apply accurate $\pi/2$ pulses to the sample. A single pulse of length τ_p was applied 5 ms before the magnetization was sampled with a CAdI cycle. The values of τ_p ranged from $0.5 \mu\text{s}$ to $16.5 \mu\text{s}$. The smallest pulse increment was 500 ns for $\tau_p \in [0.5 \mu\text{s}, 6.5 \mu\text{s}]$; H_1 field strengths of up to 80 G could have been detected (assuming three points per π rotation). The data presented in Fig. 5.24 indicate that no nutation signal was detected. The absence of a nutation signal most likely indicates that there was a non-zero concentration of paramagnetic impurities in the sample that caused the relaxation rates to be rapid enough

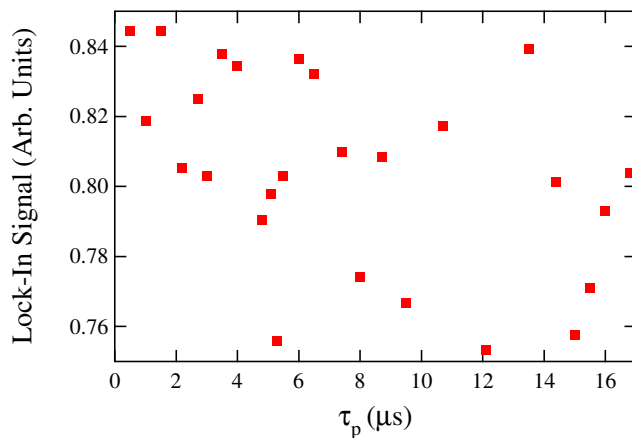


Figure 5.24: Typical results of nutation experiments with the resonance slice just inside the sample. Each data point is the peak value of an $N = 8$ averaged signal.

that, in conjunction with spin-diffusion, the coherence was degraded in a time shorter than the 5 ms interval between the pulse and the onset of the CAdI cycle. It is possible, even likely, that the crystal was significantly contaminated with water, which would certainly cause shorter relaxation times—recall the discussion of § 3.2.1 and Fig. 3.4 where in the sample-on-oscillator setup the resonance frequency of the oscillator increased even after several weeks in vacuum due to the liberation of water from the sample.

Chapter 6

Future Work: NMR-FM Measurements of Magnesium Diboride

“The Force will be with you...always.”

- Star Wars

6.1 Future Work: MgB₂

It was discovered in 2000 that magnesium diboride (MgB₂) becomes superconducting at $T_c = 39$ K [64]. This superconducting transition temperature is not extraordinarily high, but is nearly twice the highest T_c known for all other intermetallic superconductors (Nb₃Ge held the record at 23 K). It owes its high T_c to the small masses of its composite two atoms; the electron-phonon interaction of the theory of Bardeen, Cooper, and Schrieffer is manifested in this material. Within about one and a half years of its superconductivity being discovered, most of the physical properties of MgB₂ were reported; a review of this research can be found in a special issue of *Physica C* [65], and a fairly transparent overview of the history and importance of MgB₂ can be found in the March 2003 issue of *Physics Today* [66].

NMR measurements are among the many experiments performed on

any superconductor. In particular, relaxation times as functions of temperature can tell us the mechanism mediating superconductivity. For instance, s-wave superconductors (i.e., those where the electron-phonon interaction is at work like MgB₂) exhibit the well-known Hebel-Slichter coherence peak in the relaxation rate $1/T_1$ at T_c , while d-wave superconductors (like the high T_c copper oxides) do not. Furthermore, the temperature dependence of $1/T_1$ can shed light on the symmetry and anisotropy of the superconducting gap.

The temperature dependence of $1/T_1$ has been measured for MgB₂ powder samples [67, 68]. However, the Hebel-Slichter coherence peak has been broadened so much by the angle-averaging due to the powder that it is hard to claim that it has been observed. This is the heart of the issue: one of the unfortunate qualities of MgB₂ is that large single crystals cannot be made. The size limit to date is a hexagonal cylinder $\sim 100 \mu\text{m}$ between opposite vertices and $10 \mu\text{m}$ thick. Because of the limits on size, all NMR data to date have been powder measurements. These measurements average over all angles of the crystal because of the random orientation of the crystal axes of the powder. This results in data that is broadened because the electronic properties of MgB₂ are highly anisotropic. For example, in a magnetic field of 8 T, grains of the layered structure of MgB₂ shown in Fig. 6.1 with layers parallel to the field are superconducting, while those with layers perpendicular to the field are not. To understand superconducting properties, single crystal data is infinitely more important than powder data. Enter NMR-FM: *the only present technique that can measure NMR data on single crystals*

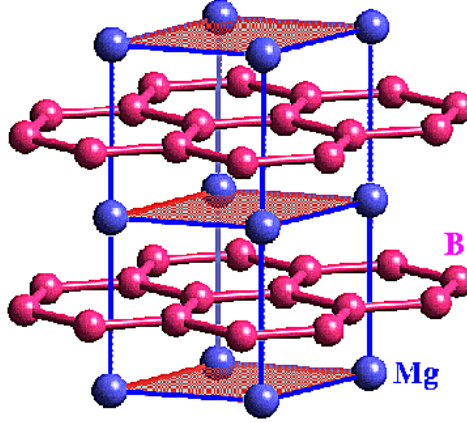


Figure 6.1: Unit cell of MgB_2 . The in-plane lattice parameter for the boron planes is $a = 0.3086$ nm, and the out-of-plane lattice parameter is $c = 0.3524$ nm.

of MgB_2 is NMR-FM. This alone demonstrates the potential of NMR-FM, but the future experiments outlined below will prove its power.

6.1.1 Feasibility Calculations

Here, we present conservative calculations of the feasibility of using NMR-FM to measure ^{11}B NMR in MgB_2 single crystals. The unit cell is shown in Fig. 6.1. We will begin by calculating the magnetization from Curie's Law

$$M_o = N \frac{\gamma^2 \hbar^2 (I(I+1))}{3k_B T} H_o, \quad (6.1)$$

where $\gamma = 2\pi \times 13.66$ MHz/T and $I = 3/2$.

We determine N from the atomic density n of ^{11}B and the volume of the crystal to be measured V , taking into consideration that the natural

abundance¹ of ¹¹B is 81.2%

$$n = \frac{6 \text{ B}/u.c. \times 0.812 \text{ }^{11}\text{B}/\text{B}}{6 \left(\frac{1}{2} (0.309 \text{ nm})^2 \times 0.352 \text{ nm}\right) /u.c.} = 4.83 \times 10^{28} \text{ }^{11}\text{B}/\text{m}^3, \quad (6.2)$$

where the denominator is the volume of the unit cell. We will assume a sample volume of $(20.0 \mu\text{m})^2 \times 1.00 \mu\text{m} = 4.00 \times 10^{-16} \text{ m}^3$; the area is typical of smaller crystals, and the thickness is that of the resonance slice (we have tacitly assumed the slice is entirely within the sample). Thus, in such a volume we find $N = 1.93 \times 10^{13}$ ¹¹B. Equation 6.1 then tells us that in an 8.2 T field the magnetization at temperature T is

$$M_o = \frac{1.2 \times 10^{-15} \text{ J/T}}{T}. \quad (6.3)$$

If we now assume that the field gradient at the sample is 10 G/ μm , we can calculate the expected ideal² force at each temperature using

$$F = \frac{1.2 \times 10^{-15} \text{ J/T}}{T} \times 10^3 \text{ T/m}. \quad (6.4)$$

To calculate the minimum detectable force, we assume previously observed values of $k_{osc} = 4 \times 10^{-4} \text{ N/m}$, $\omega_{osc}/2\pi = 2 \text{ kHz}$, and $Q = 10^3$. The sensitivity in a bandwidth $\Delta\nu$ is thus

$$F_{min} = 4.2 \times 10^{-17} \frac{\text{N}}{\sqrt{\text{K} \cdot \text{Hz}}} \times \sqrt{T \Delta\nu}. \quad (6.5)$$

Table 6.1 delineates the temperature dependent parameters for the experiment

¹It is possible to make crystals using only ¹¹B, but since this is supposed to be a conservative calculation, we simply assume the natural abundance.

²Ideal in the sense that we can manipulate all possible spins.

$T(\text{K})$	$M_o(\text{J/T})$	$F_{\text{expected}}(\text{N})$	$F_{\text{min}}(\text{N})$	SNR
300	3.8×10^{-18}	3.8×10^{-15}	1.1×10^{-15}	3.3
77	1.5×10^{-17}	1.5×10^{-14}	5.8×10^{-16}	26
39	2.9×10^{-17}	2.9×10^{-14}	4.1×10^{-16}	71
10	1.2×10^{-16}	1.2×10^{-13}	2.1×10^{-16}	550
4	2.7×10^{-16}	2.7×10^{-13}	1.4×10^{-16}	2000

Table 6.1: Important values for the magnetization, expected force, force sensitivity, and signal-to-noise ratios at interesting temperatures.

for interesting temperatures. The prospects for the experiment in this light are outstanding as the temperature is decreased.

Aside from the expected ideal signal, the other major concerns are based around the experimental parameters, namely that the spins meet the adiabatic condition, and that the fraction of spins available is large. The adiabaticity factor for sinusoidal frequency modulation is given in terms of the modulation amplitude Ω , the RF field strength H_1 , and the oscillator resonance frequency as

$$\frac{1}{\Lambda} = \frac{(\gamma H_1)^2}{\omega_{osc} \Omega}, \quad (6.6)$$

and the maximum \hat{z} component of the magnetization is

$$\left(\frac{M_z}{M_o}\right)_{max} = \frac{1}{\sqrt{1 + (\frac{\gamma H_1}{\Omega})^2}}. \quad (6.7)$$

A typical FM amplitude is $2\pi \times 50$ kHz (or below), and $H_1 \sim 5$ G is safe to assume. Some values of the adiabaticity parameter and maximum manipulable magnetization for specific FM amplitudes are given in Table 6.2. While

$\Omega/2\pi$ (kHz)	$(M_z/M_o)_{max}$	$1/\Lambda$
10	0.83	2.3
20	0.95	1.2
30	0.98	0.78
40	0.99	0.58
50	0.99	0.47

Table 6.2: Values of the adiabaticity parameter and maximum manipulable magnetization for specific FM amplitudes assuming $H_1 = 5$ G.

the maximum magnetization is comforting, the adiabaticity factor is not. Increasing H_1 to 10 G increases $1/\Lambda$ by a factor of four, but this is still relatively low for large Ω . An alternative method of FM modulation using the tangent function that will increase this factor further is presented below.

6.1.2 Experimental Plan and Considerations

The first experiments to be performed are to measure the relaxation times T_1 and T_2 as functions of temperature using the sample-on-oscillator setup. While magnet-on-oscillator may be feasible for this sample, it is not recommended. In fact, the refining of magnet-on-oscillator MRFM experiments is a difficult, long-term goal, whereas many readily accessible sample-on-oscillator MRFM experiments can be conceived. What we need right now is to show that NMR-FM can be used to actually do NMR, and the best way for this to happen is to use the sample-on-oscillator experiment.

The other major reasons for using the sample-on-oscillator setup are due to the gradient-producing magnet. This magnet should be a long cylinder

whose field and gradient profiles are easily and accurately calculated. The magnet should be made from iron ($M_s = 1700$ kA/m), if not gadolinium ($M_s = 1980$ kA/m); this will maximize its field gradient at a given sample-magnet distance for a fixed length-to-diameter aspect ratio. The magnet should be mounted in the center of the tube piezo, or a new holder should be made. One important thing is that the magnet must be held securely otherwise the field from the NMR magnet will move it; two 0-80 set screws have been successfully used for this purpose in the past. The length of the magnet will be limited by the spacing between the tube piezo stage and the oscillators; this is currently 1.25". The purpose of this experiment is not to show an image of the sample, so any resonance slice that maximizes the SNR will suffice. The largest such slice is the one that is exactly as thick as the MgB₂ crystal itself, but note that all other smaller slices have an equal SNR.

We state with confidence that the probe is ready to use on a daily basis. The major issue then that will be faced in making the first measurements on MgB₂ will be maintaining the alignment of the fiber to the oscillator during cool-down. This, however, may prove to be less difficult than expected; the large range (roughly 1 cm) of the external positioners³ of the three main stages and the use of the piezo bimorph should be able to counter act any temperature-driven misalignment. Using a large diameter magnet like that described above will be useful because its motion relative to the oscillator will

³It will be extremely advantageous to install some kind of turn-meter, something similar to those used for 10 or 15-turn potentiometers.

likely be less than the magnet's radius, leaving only the fiber and the oscillator to align.

If necessary, the piezo bimorph can be adjusted to give a larger range of motion because it is currently configured with one of the outer electrodes grounded, while the voltage is applied to the other outer electrode. In order to maximize its range, the inner electrode should be grounded, and opposite voltages should be applied to the two outer electrodes. This option also implies the design and construction of a new bimorph holder that will keep its electrodes isolated from the probe; delrin and phenolic are low-temperature compatible and should do the trick, but macor is always an option⁴.

6.1.3 Tangent-Wave Cyclic Adiabatic Inversion

After all of the cool-down issues have been dealt with, another major issue to be handled is that of spin inversion. As demonstrated above, the adiabatic condition may be an issue for MgB_2 using cyclic adiabatic inversion. More precisely, sinusoidal adiabatic inversion may be a problem. In this section, we outline different ways one might try to optimize the adiabaticity factor $1/\Lambda$.

Increasing the adiabaticity factor can be achieved most readily by changing the two main parameters of CAdI, namely the frequency modulation amplitude Ω and the RF field strength H_1 . Spin-lattice relaxation times

⁴The shop always has plenty of free scrap macor chunks.

for ^{11}B from powder NMR at 7.2 T have been measured as short as ~ 500 ms at 300 K, and as long as ~ 3000 ms at 5 K [69], so if we can boost the adiabatic factor, we may be able to use cyclic adiabatic inversion. Using the sample-on-oscillator configuration will help us do just this because the unloaded oscillators to be used in this study have resonance frequencies of about 4 kHz; placing one crystal (tens of nanograms) of MgB_2 will reduce the frequency (recall the adiabaticity factor $1/\Lambda \propto 1/\omega_{osc}$). However, the most efficient way to boost Λ is by reducing the diameter of the RF coil and thus increasing the RF field strength H_1 ($1/\Lambda \propto H_1^2$). This will mean that the coil's motion during cool-down will then become an issue if it is less than ~ 1 mm in diameter. If this route is chosen, then the coil should be secured to either the permanent magnet (or its stage) or the fiber chuck. Making a new coil may further prove useful because less power will be needed to establish acceptable values of H_1 and the oscillator and sample will then absorb less power and have stable temperatures⁵. In the end, if cyclic adiabatic inversion of any kind does not appear feasible, it is not the end of the world because other inversion methods exist (see Section 1.3.1.3: *Spin Manipulation Regimes*).

The less direct method, but perhaps the only way to go, is to use an inversion function other than our typical sinusoidal modulation of $\mathbf{H}_{eff} \cdot \hat{z}$. If the adiabatic condition is to be pressed at all, it should be pressed far off resonance because although spins that are lost will begin to relax along H_o ,

⁵The issue of sample and oscillator temperature may be enough to warrant using interrupted cyclic adiabatic inversion regardless of $1/\Lambda$.

they may be subsequently relocked as the field sweeps past them again in a short amount of time; relocking of spins is less probable if they were lost near resonance because the effective field will only pass by them again after π/ω_{osc} . Thus, if we consider H_1 fixed for all time, then the function we choose should move more slowly through resonance than at its extrema. One of the most obvious analytical functions that would satisfy this criterion is the tangent function. We cannot simply use the tangent function in all its glory because it is unbounded, and because it only has a positive slope. The true function that should be used would be piecewise-composed of part of $-\text{tangent}$ and part $+\text{tangent}$. The “part” of tangent used would be where it is finite, say, in the range from $-\pi/4$ to $+\pi/4$ ($\tan(\pm\pi/4) = \pm 1$). The proposed function is shown in Fig. 6.2.

We need to now derive an adiabatic condition in terms of our modulation parameters and the oscillator resonance frequency. For the sake of generality, we will first derive a statement for a function $f(t)$, then apply it to the tangent wave.

The basic adiabatic condition states that the Larmor frequency of the spins about the effective field (ω_L) must be much greater than the angular frequency of the effective field about the origin (ω_{eff}). To apply this statement to our system, we take

$$\mathbf{H}_{eff}(t) = H_1 \hat{x}' + \frac{\Omega}{\gamma} f(t) \hat{z}, \quad (6.8)$$

$$\omega_L(t) = \gamma | \mathbf{H}_{eff}(t) |, \quad (6.9)$$

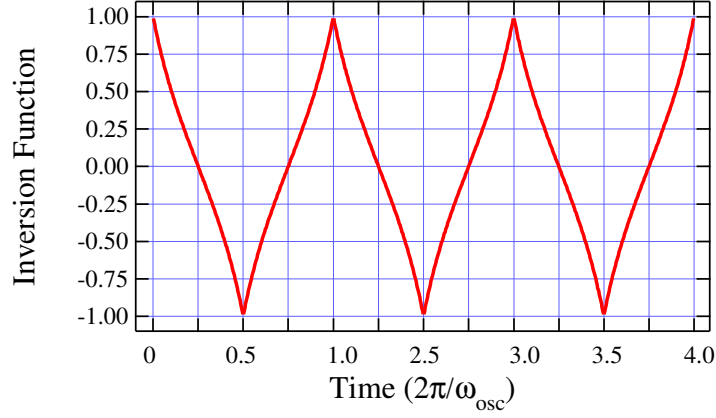


Figure 6.2: Proposed piecewise inversion function for cyclic adiabatic inversion. Odd half-oscillator periods are composed of $-\tan(\omega_{osc}t)$, and even half-oscillator periods are $+\tan(\omega_{osc}t)$. The tangent functions are truncated and merged at $\omega_{osc}t = \pm\pi/4$.

$$\omega_{eff}(t) = \frac{d\theta}{dt}, \quad (6.10)$$

where $\omega_L(t)$ and $\omega_{eff}(t)$ are functions of time, and where we take θ to be the angle from \hat{x}' to \mathbf{H}_{eff} as in §3.2. In this notation, the time-dependent adiabatic statement is

$$\omega_L(t) \gg \omega_{eff}(t). \quad (6.11)$$

Next, we write

$$\omega_{eff}(t) = \frac{d}{dt} \tan^{-1} \left(\frac{\Omega}{\gamma H_1} f(t) \right), \quad (6.12)$$

which reduces to

$$\omega_{eff}(t) = \frac{\Omega/\gamma H_1}{1 + \left[\frac{\Omega}{\gamma H_1} f(t) \right]^2} \frac{d}{dt} f(t). \quad (6.13)$$

At this point we have two choices. We can make the normal adiabatic condition proclamation that $\omega_L \gg \omega_{eff}$, or we can adopt the time dependence of Eq. 6.11. The latter will result in a function that would be most efficient, which is to say that one could declare that $\omega_L(t) = n\omega_{eff}(2)$ for all time, then derive a function for each value of n . We will not undertake this exercise at this time, but emphasize that this method is the best route for optimizing the adiabaticity factor for a given set of parameters. This will also likely lead to the maximum force signal because, as noted in § 3.2, the maximum \hat{z} component of the magnetization (and thus force) decreases as the adiabatic condition is more well-met. At this time, we opt for the former, and apply the very general result of Eq. 6.13 to the specific case of tangent-like modulation.

Let $f(t) = n \tan(\omega_{osc}t)$, where $n \in \mathbb{R}$ and ω_{osc} is the oscillator resonance frequency. The angle the effective field makes with the \hat{x} axis is

$$\theta = \tan^{-1} \left(\frac{\Omega}{\gamma H_1} n \tan(\omega_{osc}t) \right). \quad (6.14)$$

Notice that if $n\Omega/\gamma = H_1$ then $\omega_L = \omega_{eff}$. In this case, the angular velocity ω_{eff} is constant and equal to the oscillator resonance frequency. For usable present-day oscillators whose $\omega_{osc} \sim 2\pi \times 5$ kHz, the adiabatic condition is well met because $\gamma H_1 \sim 2\pi \times 50$ kHz. This represents a case that we may not want because the adiabatic condition is too well met, which may result in degradation of the force signal.

Moving along then, Equations 6.10 and 6.13 then tell us

$$\omega_{eff}(t) = \frac{\Omega/\gamma H_1}{1 + \left(\frac{n\Omega}{\gamma H_1}\right)^2 \tan^2(\omega_{osc}t)} \frac{n \omega_{osc}}{\cos^2(\omega_{osc}t)}, \quad (6.15)$$

which we can rewrite as

$$\omega_{eff}(t) = \frac{n\omega_{osc}\Omega/\gamma H_1}{\cos^2(\omega_{osc}t) + \left(\frac{n\Omega}{\gamma H_1}\right)^2 \sin^2(\omega_{osc}t)}. \quad (6.16)$$

The traditional adiabatic statement compares the maximum value of Eq. 6.16 to $\omega_L = \gamma H_1$. The maxima of Eq. 6.16 are found by determining the points at which the angular acceleration of the effective field, $\alpha_{eff}(t)$, goes to zero. Straightforward differentiation of $\omega_{eff}(t)$ reveals

$$\alpha_{eff}(t) = \frac{2n\omega_{osc}^2\Omega}{\gamma H_1} \frac{1 - \left(\frac{n\Omega}{\gamma H_1}\right)^2}{\csc^2(\omega_{osc}t) + \left(\frac{n\Omega}{\gamma H_1}\right)^2 \sec^2(\omega_{osc}t)}. \quad (6.17)$$

The possibilities for the extrema of ω_{eff} are when

$$\gamma H_1 = n\Omega, \quad (6.18)$$

$$\omega_{osc}t = m\frac{\pi}{2}, m \in \mathbb{R}. \quad (6.19)$$

The condition of Eq. 6.18 was noted above (when $\omega_{eff}(t)$ was constant). The second condition, Eq. 6.19, occurs when the tangent function diverges—we will avoid this region by truncating our piecewise waveform so that its domain is $[-\pi/4, \pi/4]$. The maximum angular velocity of the effective field will then be at the extrema of this domain. This domain is also nice because the resulting range is $[-1, 1]$, which allows Ω/γ to retain its usual meaning as the modulation amplitude... though this does change if $n \neq 1$.

To finally arrive at an adiabatic condition, we evaluate the angular velocity of the effective field $\omega_{eff}(\omega_{osc}t = \pi/4)$ to obtain

$$\frac{2n\omega_{osc}\Omega/\gamma H_1}{1 + \left(\frac{n\Omega}{\gamma H_1}\right)^2} \ll \gamma H_1, \quad (6.20)$$

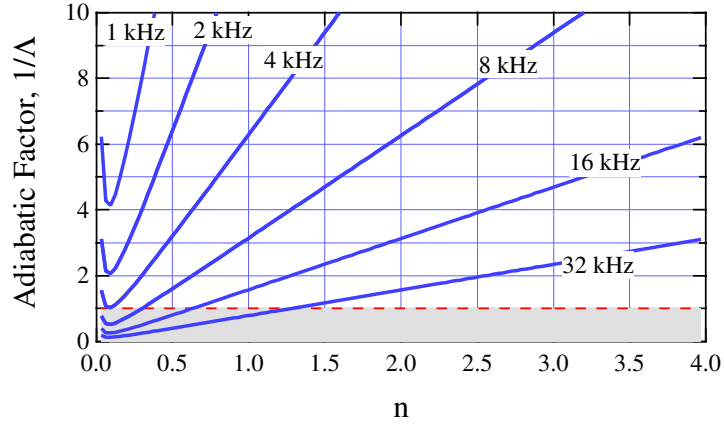


Figure 6.3: Adiabaticity factor of Eq. 6.21 as a function of the parameter n . The realistic parameters used were $\Omega = 2\pi \times 50$ kHz, $\gamma = 2\pi \times 13.66$ MHz/T, $H_1 = 3$ G, and $\omega_{osc}/2\pi$ are indicated. Because $1/\Lambda$ is significantly larger than one for $n = 1$, n should be taken as 1 for convenience. The shaded area indicates $1/\Lambda < 1$.

which we rewrite in the usual way as

$$\frac{1}{\Lambda} = \frac{(\gamma H_1)^2}{2n \omega_{osc} \Omega} + \frac{n \Omega}{2\omega_{osc}} \gg 1. \quad (6.21)$$

Figure 6.3 shows the effect the parameter n has on $1/\Lambda$. The parameters chosen for the figure had realistic experimental values $\Omega = 2\pi \times 50$ kHz, $\gamma = 2\pi \times 13.66$ MHz/T, $H_1 = 3$ G, while the oscillator resonance frequencies $\omega_{osc}/2\pi$ were chosen between 1 kHz and 32 kHz. The adiabatic condition is well-met for all values of n for low frequency oscillators, but is quite close for each of the resonance frequencies chosen. This allows us to fix n at unity, and thereby keep the traditional meaning of Ω as the modulation amplitude.

6.2 Conclusion

In conclusion, the prospects for performing NMR-FM measurements on the superconductor MgB_2 are good. The calculations presented imply that the signal strength should not be an issue if the spins can be locked to the effective field. If the traditional sinusoidal FM does not appear to work, the tangent-wave FM may increase the adiabaticity factor enough to readily lock the spins. It appears that the only thing left to do is the experiment (which of course will reveal a seemingly endless number of sub-experiments).

Appendices

Appendix A

Launching into the Fiber

Launching the light from the laser diode into the fiber optic cable of the directional coupler is, by any measure, the most tedious task of the current experimental setup. It is in principle a very simple procedure that in its most basic form is simply the collimation of light between two lenses. The arduous nature of the event (and it is an event) rears its ugly head when you realize that the margin for error in positioning of the two lenses is exceptionally small, a consequence of the size of the light emitting area of the laser and the diameter of the single mode fiber. The fiber port and laser port of the laser bench from Optics For Research (OFR) are quite well manufactured, and can allow up to 25% coupling into the fiber. The key element to assuring a decent coupling ($> 18\%$) is patience. In addition to this, I have found the step-by-step instructions from OFR, and a basic understanding of the two-lens system, invaluable.

The first time you perform an alignment, it is extremely instructive to take the ports apart. This will give you some idea of the guts of the system, and will acquaint you with what happens when you turn each of the screws. The main components of the fiber and laser ports are the same; the only real

differences are that one has an FC connector for a fiber cable, and the other has a holder for a laser diode. The direction of light flow is the $+\hat{z}$ direction, as in Fig. 2.4.

When looking at the FC connector (or diode leads), you are looking at the rear face of the port. The rear face has one through hole for the connector or diode and three sets of three screws located 120° apart. The through hole is smaller than the actual component and serves to hold the component in place by squeezing it against the bulkhead. In each set of screws, the left socket cap screw is used for \hat{z} adjustments, the middle flat-headed socket screws hold the component in place, and the right steel plunge screws that are recessed are spring-loaded and apply the counter force for the \hat{z} adjustments.

The front face of the port is plain, and should face the front face of the other port during adjustments. The lens is attached to the inside of the front face of the port with a ring magnet. Additionally, the spring-loaded feet of the steel plunge screws touch the inside of the front face. Adjusting the socket cap screws on the rear will move the front face and thus the plane in which the lens resides. The ring magnet is held in the \hat{x} - \hat{y} plane by two positioning screws on the outer perimeter of the port¹ at 12 and 4 o'clock, and by the spring-loaded counter force at 9 o'clock, when viewed from the rear. The screw at 9 o'clock on the perimeter is for locking the \hat{x} - \hat{y} position of the lens, which is unnecessary for our application so it should not be touched².

¹These screws move in the \hat{x} - \hat{y} plane.

²Locking the port can lose all of your diligently sought after coupling-don't risk it!

The first thing to do when launching into the fiber is to remove the fiber bench from the probe. I have tried launching into the fiber with the bench attached to the probe in two situations, once on the table, and once while the probe was in the NMR magnet-both failed miserably. You need the stability the lab table provides, not for the optics, but for your hand. Every adjustment you make to the ports should be done with your wrists planted on the table. This posture will allow only your fingers to move as they make the adjustments. These restrictions sound quite silly and it may seem that I'm over dramatizing things, but I'm not; a rotation of any one screw by 15° is enough to lose over half of your coupling. Having the fiber bench on the lab table also saves your back a lot of pain during this procedure, which takes even the experts at OFR at least two hours.

In order to collimate the light into or from the ports, you must first secure the bench to a small piece of optical breadboard, and fix the assembly to the table with some duct tape. You will need to borrow the connectorized laser from the other probe to align the fiber port, the short (20 cm) lime-green multi-mode fiber from the black OFR box, the photodiode from the Yttrium-Hydride transmission breadboard (or where ever), a voltmeter, and a hex-driver (not an Allen key!) that fits the \hat{z} socket caps.

The fiber port should be collimated first. Attach the FC connector from the laser to the fiber port. Check the beam by moving a flat screen³

³I make the screen out of scotch tape so that the beam spot is not too intense to view with the naked eye

back and forth from the fiber port to the laser port. Though the \hat{x} - \hat{y} position shouldn't need to be altered much at all, adjust the \hat{x} - \hat{y} screws to obtain a circular beam. If the beam is well collimated, then the laser spot will appear to have a constant diameter over this entire range. If the beam is diverging, the lens is too close, and the \hat{z} screws need to be loosened; if it is converging, it is too far from the fiber and \hat{z} screws should be tightened. Make the necessary adjustments to collimate the beam with great care-you should use 1/8 turns or less.

Next, set up the laser port. Make sure to protect the laser during this entire process by making certain that the leads of the laser diode are all electrically connected, and that you and the entire fiber bench are grounded. Once everything is in place and adjustments are ready to be made, connect the laser to the current supply and turn it on so the beam is easy to see, but not too bright. Now you should collimate the beam from the laser port in the same manner as for the fiber port (when in doubt, a slightly converging beam is preferred to a slightly diverging beam). The major difference here will be the magnitude of adjustments needed to obtain a circular beam. Additionally, you will notice the laser spot will have a bright stripe across its middle. This is due to the actual shape of the light emitting portion of the device being rectangular-there is no way to get rid of this without replacing the lens.

Now that both ports are collimated, replace the connectorized laser in the fiber port with the lime-green multi-mode fiber. Set the free end of the fiber up so that it is pointed at the photodiode. Adjust and fix this assembly

using black cloth and foil to reduce stray light from hitting the photodiode. The final setup should not be touched after finding a good light level-brushing your hand against the cloth is enough agitation to cause a light leak during alignment.

The next step is the actual coupling of the light from the laser diode into the fiber, and requires, as previously mentioned, extreme patience. Increase the laser current until a visible amount of light is launched from the laser port toward the fiber port. Adjust the transverse plane screws to minimize the clipping of the beam entering the fiber port aperture. Adjust the gain of the photodiode circuit so that this light level is near the low end of its response. Next, iteratively adjust the \hat{x} - \hat{y} screws to maximize the voltage on the voltmeter. You will have to periodically adjust the gain because the voltage will increase dramatically as the focal point of the lens gets closer to the light-emitting part of the diode. Once you have reached the first maximum in the \hat{x} - \hat{y} plane, you will have to make extremely small (less than $1/20^{th}$ of a turn) back and forth adjustments while monitoring the voltage. When you are confident the maximum has been achieved, switch to the \hat{z} screws. Tighten each \hat{z} screw slightly going clockwise while monitoring the voltage. It is common (and perhaps necessary) to see the voltage dip as you tighten one or two of the screws; the third one should then increase the voltage beyond the previous maximum; you will develop a feel for when it won't hurt to tighten while the voltage is decreasing. As the voltage gets higher and higher, the system gets touchier and touchier. You will need to make extremely small adjustments to

squeak out 20% coupling. The technique I have used to successfully make these small adjustments is to balance the Allen driver on my finger so that its center of mass is slightly off my finger; the torque resulting from the gravitational pull will then turn the screw the ridiculously small amount needed. When you have again maximized the coupling, repeat the process starting with the \hat{x} - \hat{y} screw adjustments until the coupling is about 20%.

The fiber bench with the fiber and laser ports is the most economical long-term option, but is also the most tedious to maintain. The above instructions should lead you to good coupling, but remember that 25% is as good as it gets. Other laser options that come with 25% nominal coupling include pigtailed laser diode modules and fully connectorized and optically isolated laser-supply stations; both are suitable for room temperature purposes, though the full potential (and price justification) of the latter will likely only be realized at low temperatures where noise from the laser is a serious issue.

The pigtailed design used on the other probes in the lab is easy to use, but has no optical isolation, which has been the cause of observable power fluctuations during experiments⁴. One advantage of the fiber bench is that an optical isolator can be inserted between the two ports in order to stabilize the laser power output (connectorized isolators exist for the pigtailed modules). The isolator uses Faraday Rotation of polarized light: light from the

⁴The laser settles down after a few hours, but having to wait is annoying.

laser passes through a polarizer (P_1), is rotated 45° clockwise by a permanent magnet in the isolator, passes through a second polarizer (P_2) at 45° degrees to the first, goes out to the fiber, reflects somewhere causing it to head back toward the laser, passes through P_2 , is rotated another 45° by the isolator's magnet, and finally hits P_1 at 90° to its axis, which allows no light back to the laser. One disadvantage of using the optical isolator with the current setup is that the fiber bench would have to be kept out of the field of the magnet because the extra field will cause additional rotation of the light, which would decrease the isolation. Our current optical isolator from OFR has been on the probe while it was in the magnet so its isolation may not meet specs. This may also have caused an observed decrease in fringe size when the probe was in the magnet [27]. Because the laser stability does not seem to be a current issue with this probe, and because the isolator halves (or more than halves) the coupling into the fiber, it has been removed for the time being.

Appendix B

BNC Feedthrough Vacuum Compatibility

Leaks in the vacuum system are a great headache. After many attempts to make vacuum compatible BNC feedthroughs, the following procedure has proven successful. Begin with a 1 inch thick KF blank flange. Drill a clearance hole through the axis of the flange. Next, mount the flange on the mill so that it can be cut at 45° to its axis. Remove just enough material that the flat is slightly larger than the diameter of the collar of the BNC. Drill a clearance hole perpendicular to this flat, but only so deep that it breaks into the through hole along the axis. At this point, make sure you can see material around the outside of the collar of the BNC when it is placed in the hole; remove more material if necessary. Rotate the part 90° and repeat these first steps. Do not chamfer the holes or else the collar will not evenly touch the flats. When the milling and drilling is finished, you will notice rough edges inside the axis hole where the other holes have broken through: clean off any large burrs, but don't waste your time trying to make the edges smooth. Remove the cutting fluid from the part by boiling it in acetone for several minutes at least twice. After the final hot acetone bath and before the part dries, rinse the flange with methanol to remove the acetone polymer. Wrap the clean flange in aluminum foil to keep it lint free.

The next thing to do is prepare the chassis-isolated BNC feedthroughs for the epoxy. First, solder all leads to the BNCs¹. I recommend using solid wire instead of braided wire. Fill the core cups up with solder before inserting the wire. Make sure there are a few millimeters of bare wire between the solder and the insulation so the epoxy can bind directly to metal. When they have dried, clean the flux off all surfaces with clean acetone-soaked cotton swab; repeat this until the swabs no longer pick up any visible residue². After the BNCs have been cleaned, apply a generous layer of superglue to the metal-insulator interfaces and over the solder joint on the core electrode. Next, repeat this with 5-minute epoxy, one BNC at a time. Apply the epoxy using the wood end of a cotton swab. Be sure to use only enough epoxy to cover the soldered leads and the metal-insulator interfaces since if there is too much epoxy it will run over the sides and drip onto the threads, making the piece too large to fit into the clearance holes in the flange. When the epoxy has dried, inspect the lab side of the feedthrough to make sure no glue or epoxy has leaked through and filled up the center female electrode.

At this point, the BNCs should appear as depicted in Fig. B. Once the BNCs are sealed, they should be secured into the flange³. Do this, as before, using the 5-minute epoxy, one feedthrough at a time. Apply just enough epoxy to form a continuous ring to the vacuum side of the BNC collar (where the

¹Make sure to do a good job because soldering after the BNCs are set in epoxy is dangerous because the heat can crack the epoxy.

²Do not soak the BNCs in acetone to remove the flux because the insulating material is readily dissolved by acetone.

³Test the conductivity through both electrodes of each BNC before proceeding.

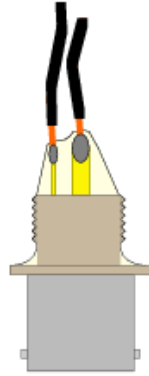


Figure B.1: BNC with the proper amount of epoxy. Any more epoxy will spill over the edge onto the threads.

BNC will touch flange). Insert the BNC into its hole in the flange and twist it around twice while pressing gently; this will make certain the epoxy is evenly applied around the BNC. Inspect the piece from the vacuum side to make sure that the leads are not touching other leads or the walls of the holes in its final position. Allow the epoxy to fully cure with the BNC in place before repeating these steps for the other feedthroughs. After all the feedthroughs have cured in place, apply a coating of superglue over the flange-epoxy-BNC interface as a bit of insurance. Finally, prepare the flange for the vacuum compatible Stycast epoxy. Make a small protective barrier around the axis hole of the flange out of modelling clay incase the epoxy overflows. Prepare the Stycast epoxy according to its directions, making sure to pump on it until the bubbling has subsided for several minutes. Slowly pour the epoxy into the hole while maintaining a constant flow. Pour in the epoxy until the level reaches the surface of the flange. Let the epoxy cure overnight at room temperature; do

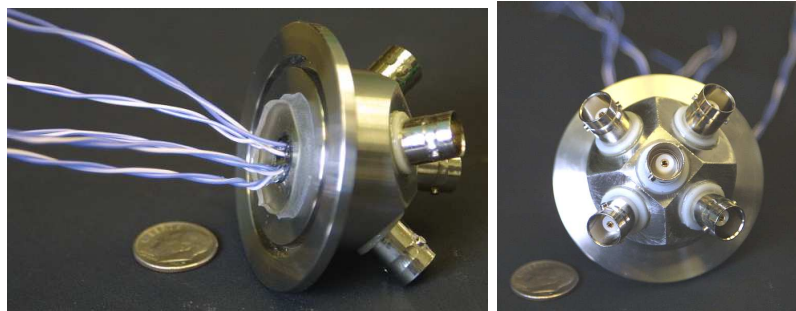


Figure B.2: Photographs of completed BNC feedthrough.

not cure the flange with heat cycle. Have the part leak checked after removing the modelling clay with an alcohol-soaked cotton swab. The final part should look something like Fig. B.

Bibliography

- [1] J. J. Sakurai, *Modern Quantum Mechanics*, revised ed. (Addison-Wesley, Reading, 1994).
- [2] D. J. Griffiths, *Introduction to Quantum Mechanics* (Prentice-Hall, Englewood Cliffs, 1995).
- [3] R. A. Serway, C. J. Moses, and C. A. Moyer, *Modern Physics*, 2nd ed. (Saunders College Publishing, Fort Worth, 1989).
- [4] A. Abragam, *Principles of Nuclear Magnetism* (Oxford University Press, New York, 1986).
- [5] C. P. Slichter, *Principles of Magnetic Resonance*, 2nd ed. (Springer-Verlag, New York, 1978).
- [6] F. Bloch, *Phys. Rev.* **70**, 460 (1946).
- [7] G. E. Pake, *Amer. J. Phys.* **18**, 438 (1950).
- [8] G. E. Pake, *Amer. J. Phys.* **18**, 473 (1950).
- [9] J. A. Sidles, *Appl. Phys. Lett.* **58**, 2854 (1991).
- [10] K. R. Thurber, L. E. Harrell, and D. D. Smith, *J. Magn. Res.* **16**, 336 (2003).

- [11] J. A. Marohn, R. Fainchtein, and D. D. Smith, *J. Appl. Phys.* **86**, 4619 (1999).
- [12] O. Klein, V. V. Naletov, and H. Alloul, *Eur. Phys. J. B* **17**, 57 (2000).
- [13] B. C. Stipe *et al.*, *Phys. Rev. Lett.* **87**, 277602 (2001).
- [14] J. D. Hannay, R. W. Chantrell, and D. Rugar, *J. Appl. Phys.* **87**, 6827 (2000).
- [15] K. Wago, D. Botkin, C. S. Yannoni, and D. Rugar, *J. Vac. Sci. Technol. B* **14**, 1197 (1996).
- [16] D. Rugar, C. S. Yannoni, and J. A. Sidles, *Nature* **360**, 563 (1992).
- [17] Z. Zhang, M. L. Roukes, and P. C. Hammel, *J. Appl. Phys.* **80**, 6931 (1996).
- [18] M. D. Chabot *et al.*, *Proc. SPIE* **4559**, 24 (2001).
- [19] B. C. Stipe *et al.*, *Phys. Rev. Lett.* **87**, 096801 (2001).
- [20] K. Wago *et al.*, *J. Vac. Sci. Technol. B* **14**, 1197 (1996).
- [21] T. D. Stowe *et al.*, *Appl. Phys. Lett.* **71**, 288 (1997).
- [22] A. N. Cleland and M. L. Roukes, *Appl. Phys. Lett.* **69**, 2653 (1996).
- [23] M. D. Chabot and J. T. Markert, *Proc. SPIE* **3875**, 104 (1999).

- [24] P. C. Hammel, Z. Zhang, G. J. Moore, and M. L. Roukes, *Book?* **101**, 59 (1995).
- [25] T. G. Ruskell, M. Loehndorf, and J. Moreland, *J. Appl. Phys.* **86**, 664 (1999).
- [26] A. Schaff and W. S. Veeman, *J. Appl. Phys.* **80**, 6931 (1996).
- [27] M. D. Chabot, Ph.D. thesis, University of Texas at Austin, 2001.
- [28] J. L. Garbini, K. J. Bruland, W. M. Dougherty, and J. A. Sidles, *J. Appl. Phys.* **80**, 1951 (1996).
- [29] K. J. Bruland, J. L. Garbini, W. M. Dougherty, and J. A. Sidles, *J. Appl. Phys.* **80**, 1959 (1996).
- [30] O. Zueger and D. Rugar, *Appl. Phys. Lett.* **63**, 2496 (1993).
- [31] O. Zueger, S. T. Holen, C. S. Yannoni, and D. Rugar, *J. Appl. Phys.* **79**, 1881 (1996).
- [32] H. J. Mamin and D. Rugar, *J. Vac. Sci. Technol. B* **14**, 1197 (1996).
- [33] K. J. Bruland *et al.*, *Rev. Sci. Instrum.* **70**, 3542 (1999).
- [34] D. Rugar *et al.*, *Science* **264**, 1560 (1994).
- [35] K. Y. Yasumura *et al.*, *J. Vac. Sci. Technol. B* **14**, 1197 (1996).
- [36] A. Torii, M. Sasaki, K. Hane, and S. Okuma, *Meas. Sci. Technol.* **7**, 179 (1996).

- [37] J. A. Sidles *et al.*, Rev. Mod. Phys. **67**, 249 (1995).
- [38] H. A. Sommer, Master's thesis, University of Texas at Austin, 1995.
- [39] K. Tatebe, Senior Honors Thesis, University of Texas at Austin, 2001.
- [40] J. L. Cobb, Ph.D. thesis, University of Texas at Austin, 1995.
- [41] K. Kim and S. Lee, J. Appl. Phys. **91**, 4715 (2002).
- [42] M. Zalalutdinov *et al.*, Appl. Phys. Lett. **79**, 695 (2001).
- [43] G. C. Ratcliff, D. A. Erie, and R. Supefine, Appl. Phys. Lett. **72**, 1911 (1998).
- [44] Y. J. Rao and B. Culsaw, Sens. and Actuat. A **30**, 203 (1992).
- [45] D. Sawicki and J. H. Eberly, Opt. Expr. **4**, 217 (1999).
- [46] K. Wago *et al.*, J. Vac. Sci. Technol. B **14**, 1197 (1996).
- [47] W. C. Fischler, Class Notes, Quantum Mechanics II, 2001.
- [48] P. Guttinger, Zeits. f. Phys. **73**, 169 (1931).
- [49] J. A. Sidles, Appl. Phys. Lett. **58**, 2854 (1991).
- [50] B. C. Stipe *et al.*, Phys. Rev. Lett. **87**, 277602 (2001).
- [51] Z. Zhang and P. C. Hammel, IEEE Trans. Magn. **33**, 4047 (1997).

- [52] J. A. Mahron, R. Fainchtein, and D. D. Smith, *J. Appl. Phys.* **86**, 4619 (1999).
- [53] O. Klein, V. V. Naletov, and H. Alloul, *Eur. Phys. J. B* **17**, 57 (2000).
- [54] B. C. Stipe *et al.*, *Phys. Rev. Lett.* **86**, 2874 (2001).
- [55] J. A. Mahron, R. Fainchtein, and D. D. Smith, *Appl. Phys. Lett.* **73**, 3778 (1998).
- [56] T. C. Messina, Ph.D. thesis, University of Texas at Austin, 2002.
- [57] T. Graf, Master's thesis, University of Texas at Austin, 1996.
- [58] K. Wago, D. Botkin, C. S. Yannoni, and D. Rugar, *Phys. Rev. B* **57**, 1108 (1998).
- [59] Y. Yamada, T. Suzuki, and E. N. Abarra, *IEEE Trans. Magn.* **33**, 3622 (1997).
- [60] C. W. Miller *et al.*, *J. Appl. Phys.* **93**, 6572 (2003).
- [61] A. Suter, D. V. Pelekhov, M. L. Roukes, and P. C. Hammel, *J. Magn. Res.* **154**, 210 (2002).
- [62] P. C. Hammel *et al.*, *Proc. IEEE* **91**, 789 (2003).
- [63] M. D. Chabot and J. Moreland (unpublished).
- [64] J. Nagamatsu *et al.*, *Nature* **410**, 63 (2001).

- [65] *Physica C* **385**, 1 (2003).
- [66] P. C. Canfield and G. W. Crabtree, *Physics Today* **March**, 34 (2003).
- [67] Kotegawa *et al.*, *Phys. Rev. B* **66**, 064516 (2002).
- [68] Kotegawa *et al.*, *Phys. Rev. Lett.* **87**, 127001 (2001).
- [69] S. H. Baek *et al.*, *Phys. Rev. B* **66**, 104510 (2002).
- [70] K. Wago *et al.*, *Rev. Sci. Instrum.* **68**, 1823 (1997).
- [71] M. D. Chabot and J. T. Markert, *Proc. SPIE* **3875**, 104 (1999).
- [72] M. D. Chabot *et al.*, *Proc. SPIE* **4559**, 24 (2001).

Vita

Casey William Miller was born April 30, 1977 in Rochester, New York to William and Sharon Miller. He entered Wittenberg University in Springfield, Ohio in August of 1996. During his sophomore and junior years, he worked with Professor Albert J. Frasca studying radiation damage effects on prototype silicon carbide thyristors. For his Honors Thesis, *The Effects of Fast Neutron Bombardment on the Radar Cross Section of Metal and Dielectric Spheres*, he worked with Professor Daniel Fleisch. He was made a member of Phi Beta Kappa by the action of the Omicron of Ohio at Wittenberg University on April 12, 1999 in recognition of high attainments in liberal scholarship. He graduated *Summa Cum Laude* in May of 1999 with his Bachelor of Arts Degree in Physics with University and Departmental Honors.

He entered the Physics Department of The University of Texas at Austin in June, 1999. In January of 2001, he was fortunate enough that Professor John T. Markert was willing to risk allowing him into his lab. He first studied the switchable mirror effect in films of yttrium hydride, then finally found his niche working on nuclear magnetic resonance force microscopy. He was lucky enough to receive the University Co-Op Society's 2002 **Outstanding Graduate Research Award** for work on NMR-FM.

After receiving his Ph. D., he will move to San Diego, California to

work with Professor Ivan K. Schuller on "nanomagnetism and sensors, broadly defined".

Permanent address: 4013 Burnet Road
Suite A
Austin, Texas 78756

This dissertation was typeset with \LaTeX^\dagger by the author.

[†] \LaTeX is a document preparation system developed by Leslie Lamport as a special version of Donald Knuth's \TeX Program.